Surgenor

Mass Transfer and Shear Stress at the Wall for Cocurrent Gas-Liquid Flows in a Vertical Tube

M.Eng.

MASS TRANSFER AND SHEAR STRESS AT THE WALL FOR COCURRENT GAS-LIQUID FLOWS IN A VERTICAL TUBE

by

BRIAN W. SURGENOR, B.Eng.

A Report Submitted to the School of Graduate Studies
in Partial Fulfillment of the Requirements
for the Degree
Master of Engineering

Department of Engineering Physics
McMaster University
Hamilton, Ontario, L8S 4M1, Canada

January 1979

MASTER OF ENGINEERING (1979)
Department of Engineering Physics

TITLE: Mass Transfer and Shear Stress at the Wall for Cocurrent Gas-Liquid Flows in a Vertical Tube

AUTHOR: Brian W. Surgenor, B.Eng. (Queen's)

SUPERVISOR: Dr. S. Banerjee

NUMBER OF PAGES: xiii, 170

ABSTRACT

An investigation of the technique of obtaining the wall shear stress in a two-phase flow, by measuring the mass transfer coefficient at the wall with the electrochemical method, has been completed.

The experiments involved the measurement of flow rates, pressure drops, void fractions and mass transfer coefficients, for a cocurrent upwards gas-liquid flow in a vertical tube, 13 mm in diameter. The liquid phase was an electrolyte consisting of 1.0 to 3.0 molar sodium hydroxide, and 0.005 to 0.010 equimolar potassium ferricyanide and potassium ferrocyanide. The gas phase was nitrogen. The flow regimes studied were slug, churn and annular.

Emphasis is placed on the measurements obtained with the electrochemical method. Its application, advantages and disadvantages are detailed. A series of single-phase experiments were performed to explore the characteristics of the method and to serve as benchmarks for the two-phase experiments.

The space-time-averaged values of the mass transfer coefficient were found to give the wall shear stresses to an accuracy of ±20%. Frequency analysis of the local fluctuating values indicate that measurements of the local mass transfer coefficient can be used for flow regime identification.

The theoretical flow regime map of Dukler and Taitel successfully predicted the flow regimes. The correlations of Griffith and Wallis, and Lockhart and Martinelli as modified by Davis, predicted the pressure drops and void fractions to an accuracy ±15% when applied to the appropriate flow regimes. As a further exercise, the force interactions between the phases, referred to as the interfacial shear terms, were calculated from both the measured and predicted void fractions and pressure drops.

ACKNOWLEDGEMENTS

The author gratefully acknowledges the supervision of Dr. S Banerjee.

Thanks must be extended to M. Vandenbroek who aided in the construction, maintenance and operation of the experimental apparatus.

The financial support provided by the National Research Council of Canada in the form of a scholarship is also greatly appreciated.

TABLE OF CONTENTS

LIST OF TABLES

LIST OF FIGURES

CHAPTER 1

INTRODUCTION

Safety analyses of nuclear reactor core cooling systems require accurate analytical models of two-phase flows under transient conditions. The nuclear industry is certainly not the only area where two-phase flow modelling finds application, but it is where research is being most actively pursued. Current safety analysis codes use the homogeneous equilibrium model in which the two-phase flow is treated as a pseudo single-phase flow with properties representing the average of the two phases involved. An improved description of two-phase flow can be obtained by writing the conservation equations of mass, momentum and energy separately for each phase. In this separated flow model the phases can have unequal velocities, pressures and temperatures, and additional information in the form of interphase constitutive relations is required. This investigation arose out of the need to develop accurate constitutive relations for interfacial momentum transfer. If this is to be accomplished one has to make available a means to accurately measure wall shear stress in a two-phase flow. The reasons for this requirement are discussed in Section 2.1.

Three classes of methods exist to measure wall shear stress (1):

1. Balancing methods. By allowing a section of the wall to float, balancing and then measuring the force exerted on the wall will provide the wall shear stress.

2. Heat and mass transfer methods. By transferring heat or mass to the fluid near the wall, over a short distance within the developing boundary layer the transfer is controlled by the velocity gradient. Thus the wall shear stress can be obtained from the rate of heat or mass transfer.

3. Wall impact probes. By measuring the impact pressure on a Preston or Stanton tube, the fluid momentum flux adjacent to the wall is obtained. The wall shear stress can be calculated from an empirical relationship.

The electrochemical method belongs to the second class. It was chosen for investigation in this study due to its versatility and accuracy. The method has been applied to two-phase flow in the past. Sutey (2) studied climbing film flow in an annulus. Kutateladze et al (3) made brief report of success in applying the method to vertical flow in the bubble, slug and annular regimes. It was felt that a more detailed study and report was warranted in order that a laboratory could apply the electrochemical method in confidence to a two-phase flow.

The investigation involved the construction of a loop that would circulate a two-phase mixture of gaseous nitrogen

and liquid electrolyte through a vertical tube. The flow regimes available for study were slug, churn and annular. The conditions of operation were such that the wall shear stresses in the test section could be calculated from the measured flow rates, pressure drops and void fractions. These values could than be compared with the wall shear stresses calculated from the wall mass transfer coefficients as measured with the electrochemical method. In this manner the accuracy of the method could be determined. Experiments in both single- and two-phase flow were performed to define the method's characteristics, proper application, advantages and disadvantages. The technique of using the fluctuating value of the mass transfer coefficient for flow regime identification was investigated.

The observed flow regimes were compared with applicable flow regime maps. The measured void fractions and pressure drops were compared with the predictions of available correlations. The interfacial shear terms were calculated from the measured void fractions and pressure drops and compared with the interfacial shear terms predicted by these same correlations.

CHAPTER 2

PREVIOUS WORK AND THEORY ON COCURRENT GAS-LIQUID FLOW

The analysis of two-phase flow is extremely difficult, not only because of the additional variables compared to single-phase flow, but because of the variety of flow regimes that can exist. These flow regimes can be classified according to the relative amounts of the two phases, their distribution and individual motions. The clearly identifiable regimes for vertical flow are illustrated in Figure 2-1, adapted from Collier (4, p. 9). Descriptions in order of their appearance with increasing gas flow rate are:

1. Bubble flow. The liquid forms the continuous phase, with the gas dispersed as small individual bubbles.
2. Slug flow. The gas flows as large bullet shaped bubbles, referred to as Taylor bubbles. These are separated by slugs of liquid, which frequently contain small gas bubbles. Each Taylor bubble is surrounded by a thin film which may or may not be falling relative to the wall (5, p. 393).
3. Churn flow. For slug flow there is a point at which the role of the liquid slug as a bridge between successive Taylor bubbles is disrupted, possibly due to an excessive amount of entrained gas in the slug.

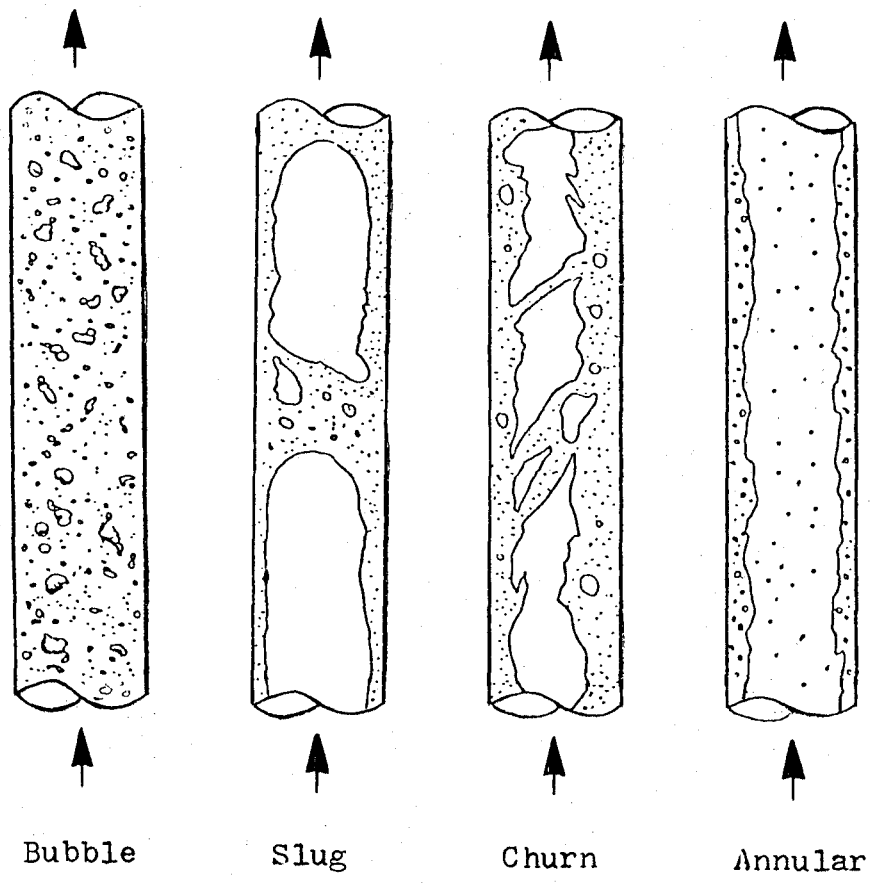

Fig. 2-1. Flow regimes in vertical cocurrent flow.

When this occurs, the liquid falls, accumulates, reforms as a slug and then is swept up once again by the gas. The oscillatory motion of the liquid is characteristic of the churn flow regime. Churn flow is considered to be a transitional regime occuring only below certain liquid flow rates, between the more permanent slug and annular regimes.

4. Annular flow. This regime is characterized by a continuous gas core, with some of the liquid entrained as droplets and the remainder travelling as an annular film on the tube wall. The liquid film is not uniform in thickness and is in fact quite wavy.

Which of these flow regimes will be present is a function of the flow rates, fluid properties, and channel size, shape and orientation. Most realistic models of two-phase flow are based upon the geometry of one specific regime. A model developed for one regime will not necessarily be valid for other regimes, where the distribution and characteristic motion of the phases, and thus the boundary conditions, could be very different. The practice of presenting a correlation without identifying the flow regime is no longer considered acceptable.

In light of this, correlations for the void fraction and pressure drop, specific to the slug and annular flow regimes, together with the means of quantitatively predicting the existence of a regime, are given in this chapter. No correlation specific to the churn flow regime is available.

As the concepts and correlations contained in this

chapter are widely known, only their underlying assumptions and final forms will be given. Wallis' book (6) is available if one desires a detailed analytical discussion of two-phase flow. The text by Govier and Aziz (5) provides further empirical coverage of two-component two-phase flows. For the subject of convective boiling, one should refer to the book by Collier (4). Hewitt and Hall-Taylor's work (7) provides comprehensive coverage of annular two-phase flow.

2.1 Governing Equations

In order that the structure of the separated flow model can be appreciated, the simple momentum equations used for calculations in this report, will be derived from the complete one dimensional, cross-sectionally averaged, mass and momentum conservation equations as used by the separated flow model. The form presented by Banerjee and Hancox (8) will be used. One should refer to this paper for a discussion of two-phase flow models and their application to reactor safety.

All quantities are volume-averaged in order to make the problem tractable. The averaging brackets are defined by

$$\langle h_j \rangle = \frac{1}{V_j} \int_{V_j} h_j \, dV$$

where V_j is the volume occupied by phase j.

$$\langle h_j \rangle_i = \frac{1}{V} \int_{a_i} h_j \, dA$$

where the volume V is formed by the cross-sectional area A and the length z.

Mass conservation:

$$\frac{\partial}{\partial t} \alpha_j \langle \rho_j \rangle + \frac{\partial}{\partial z} \alpha_j \langle \rho_j u_j \rangle = \langle M_j \rangle_i \qquad (2.1)$$

where the void fraction α_j is the volume fraction occupied by phase j, $\alpha_j = V_j/V$, and $\langle M_j \rangle_i$ is the mass transfer across the interface to phase j per unit volume.

Momentum conservation:

$$\frac{\partial}{\partial t} \alpha_j \langle \rho_j u_j \rangle + \frac{\partial}{\partial z} \alpha_j \langle \rho_j u_j^2 \rangle + \alpha_j \langle \partial P_j / \partial z \rangle$$

$$- \frac{\partial}{\partial z} \alpha_j \langle \tau_{zz,j} \rangle = \alpha_j \langle \rho_j F_{z,j} \rangle - \langle M_j u_j \rangle_i$$

$$+ \langle \vec{n}_j \cdot \vec{\tau}_z \rangle_i + \langle \vec{n}_{jw} \cdot \vec{\tau}_z \rangle_w \qquad (2.2)$$

where

$\vec{n}_j$ = outward drawn normal from phase j

$\frac{\partial}{\partial z} \alpha_j \langle \tau_{zz,j} \rangle$ = normal stress on the fluid element

$F_{z,j}$ = body force per unit mass

$\langle M_j u_j \rangle_i$ = momentum flux across the interface to phase j per unit volume due to mass transfer

$\langle \vec{n}_j \cdot \vec{\vec{\tau}}_z \rangle_i$ = average shear stress acting at the phase interface

$\langle \vec{n}_{jw} \cdot \vec{\vec{\tau}}_z \rangle_w$ = average shear stress acting at the wall interface

The term $\propto_j \langle \partial P_j / \partial z \rangle$ comes from a simplification of the basic momentum equation, using Gauss' Theorem and assuming that the phase pressure at the interface is equal to the bulk phase pressure $P_{ji} = P_j$.

The following simplifications and assumptions are made:

1. For steady state conditions, $\partial / \partial t = 0$.
2. For two-component systems, $\langle M_j \rangle_i = 0$.
3. For vertical upward flow, $F_{z,j} = -g$.
4. The wall is continuously wetted, $\langle \vec{n}_{gw} \cdot \vec{\vec{\tau}}_z \rangle = 0$.
5. The liquid phase is incompressible, $\partial \rho_l / \partial z = 0$.
6. The gas phase behaves ideally and the pressure gradient is linear,

$$\Delta \rho_g = \int_1^2 \rho_g \, dz = (P_1 + P_2) / (2 R T)$$

7. The void fraction, wall shear stress, interfacial shear stress and interfacial area are constant along the integration length L.
8. The phase pressures are equal, $P_l = P_g$.
9. The intraphase distribution is such that the

product of the averages is equal to the average of the products, thus $\langle \rho u \rangle = \langle \rho \rangle \langle u \rangle$. This implies flat cross-sectional profiles for all variables.

10. The interfacial shear stresses act equally and in opposite directions,

$$\langle \vec{n}_g \vec{\tau}_z \rangle_i = - \langle \vec{n}_l \vec{\tau}_z \rangle_i$$

It is assumed that these interfacial shear terms contain no derivative terms.

Under these ten conditions, equation (2.1) requires that $\partial G_j / \partial z = 0$ and after integration, equation (2.2) can be written for each phase as

$$(1 - \alpha)\Delta P/L = -(1 - \alpha)\rho_l g + \tau_i a_i / (A L) - \tau_w a_w / (A L) \qquad (2.3)$$

$$G_g^2 / (\Delta \rho_g \alpha L) + \alpha \Delta P/L = - \alpha \rho_g g - \tau_i a_i / (A L) \qquad (2.4)$$

where the averaging brackets are now assumed and the directions for the shear stresses are those indicated in Figure 2-2. Combining equations (2.3) and (2.4) gives

$$-\Delta P/L = [(1 - \alpha)\rho_l + \alpha \rho_g] g + G_g^2 / (\Delta \rho_g \alpha L) + 4 \tau_w / D \qquad (2.5)$$

This is the most common form of the momentum equation for an idealized adiabatic steady-state two-phase flow. The three terms of the right side of equation (2.5) are the gravitational,

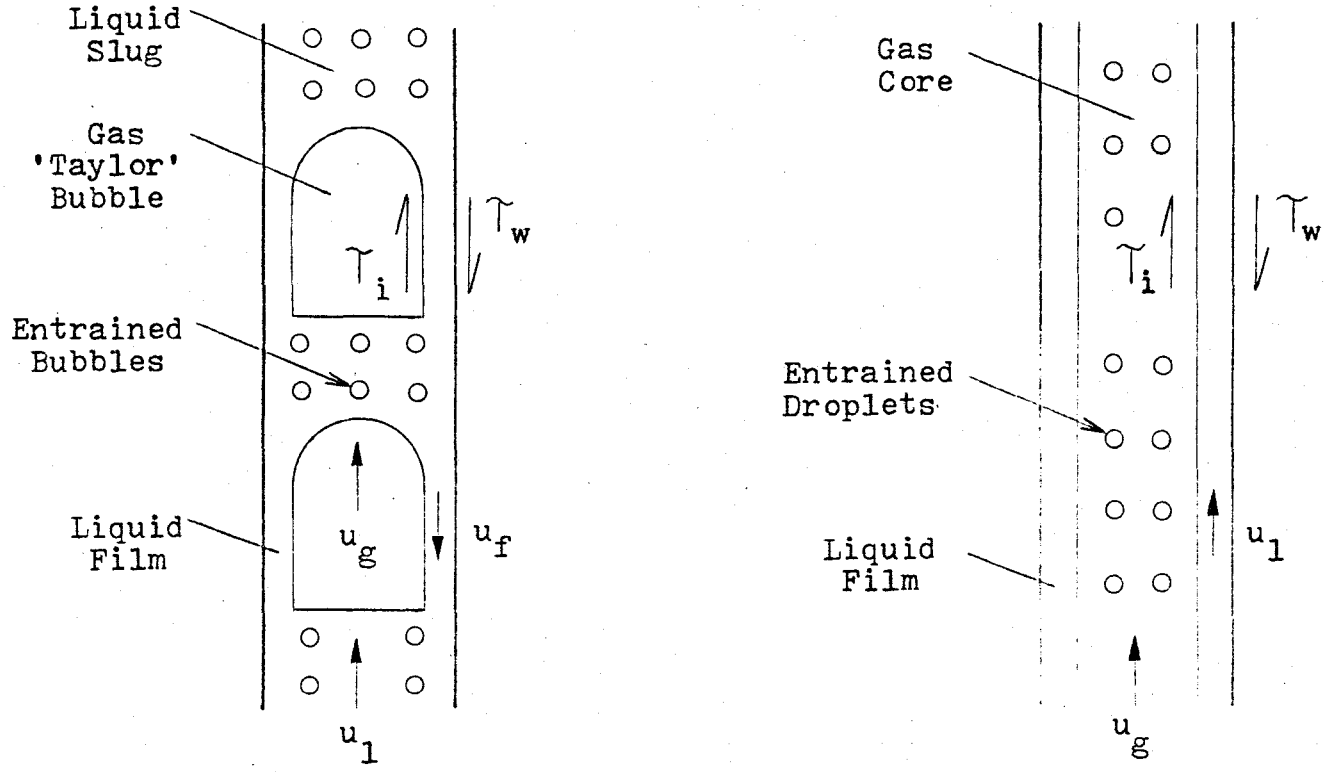

Fig. 2-2. Idealized geometry of the slug and annular flow regimes.

accelerational and frictional components of the pressure drop, respectively. Equation (2.5) is used to calculate the wall shear stress from the measured variables. Equation (2.3) or (2.4) can be used to calculate the wall shear term $\tau_i a_i$.

Earlier work on the measurement of the wall shear stress was prompted by the difficulty of determining the accelerational component of the pressure drop in certain systems, making it necessary to determine the remaining gravitational and frictional components (7, p. 28). If the accelerational component can in fact be neglected, then equation (2.5) can be used to calculate the void fraction, with knowledge of the total pressure drop and wall shear stress.

Under flow conditions such as those experienced in critical or choked flow where the pressure gradients are steep, equations (2.3) and (2.4) may give inconsistent answers for the interfacial shear terms. In these equations the interfacial shear stress represents the interphase momentum transfer constitutive relationship found in the separated flow model. The interphase momentum transfer results from the forces exerted on the phases by each other. These forces can be thought to be made up of two components:

1. The frictional force interaction between the phases. This force is analogous to the frictional force at the wall in a single-phase flow.
2. The force created by the interference between the phases. If the phases are not moving at the

same velocity or direction, one phase must move as it is displaced by the other.

The second force component is referred to as the 'added mass' or 'virtual mass' term. It requires that the constitutive relationship take into account the mass of the phase being accelerated as well as the mass of the phase being displaced. If upon measuring the total pressure drop and its components, the interfacial shear terms do not balance, their form and underlying assumptions must be re-evaluated. Effects such as those of virtual mass and the presence of derivative terms in the interfacial shear terms might have to be considered. For such an analysis to be carried out, there is a need to be able to measure the wall shear stress under conditions where steep pressure gradients exist, and accelerational and interfacial effects become dominant.

2.2 Flow Regime Prediction

Two-phase flow regimes are most often identified in a subjective manner by visual observation in a transparent test section, coupled with conventional photography. More objective identification can be made by signal analysis of the local fluctuations in pressure, void fraction or wall shear stress (1). Analyzing the power spectral density distribution of the fluctuations can provide characterizations of specified flow regime. The results of the study of Kutateladze et al (9) on the spectral characteristics of the

wall shear stress, as measured with the electrochemical method, are presented in Figure 2-3. The spectra for the bubble regime exhibit maxima at frequencies less than 2 Hz. Additional maxima between 4 and 10 Hz appear for the slug flow regime. For the annular regime maxima appear in the spectra between 10 and 16 Hz. By measuring the relative magnitude of the fluctuations it is seen that the slug flow regime can be clearly identified.

The problem of predicting which flow regime will exist under specified flow conditions is still unresolved. Most efforts have taken the approach of plotting the transition boundaries on two-dimensional plots based solely upon experimental observation. One such empirical map is that of Hewitt and Roberts (10), illustrated in Figure 2-4. X-ray photography was used to aid in the identification process. This photographic technique has advantages over conventional photography in that the picture of the flow structure is not confused by light refractions and reflections from the phase interfaces. However such maps are criticized for their non-physical basis, inaccuracy (there is little agreement among them) and restrictive nature. A map based upon observations for one pipe size and set of fluid properties cannot necessarily be applied to another set of conditions. Dukler and Taitel (11) proposed models of the transition mechanisms from one regime to another and subsequently derived a theoretical flow regime map. This map is also given in Figure 2-4. Comparing the map of Hewitt and Roberts with the map of

Ψ = Dimensionless spectral density function of wall shear stress fluctuations.

τ_w'/τ_w = Ratio of rms value of wall shear stress fluctuations to the average wall shear.

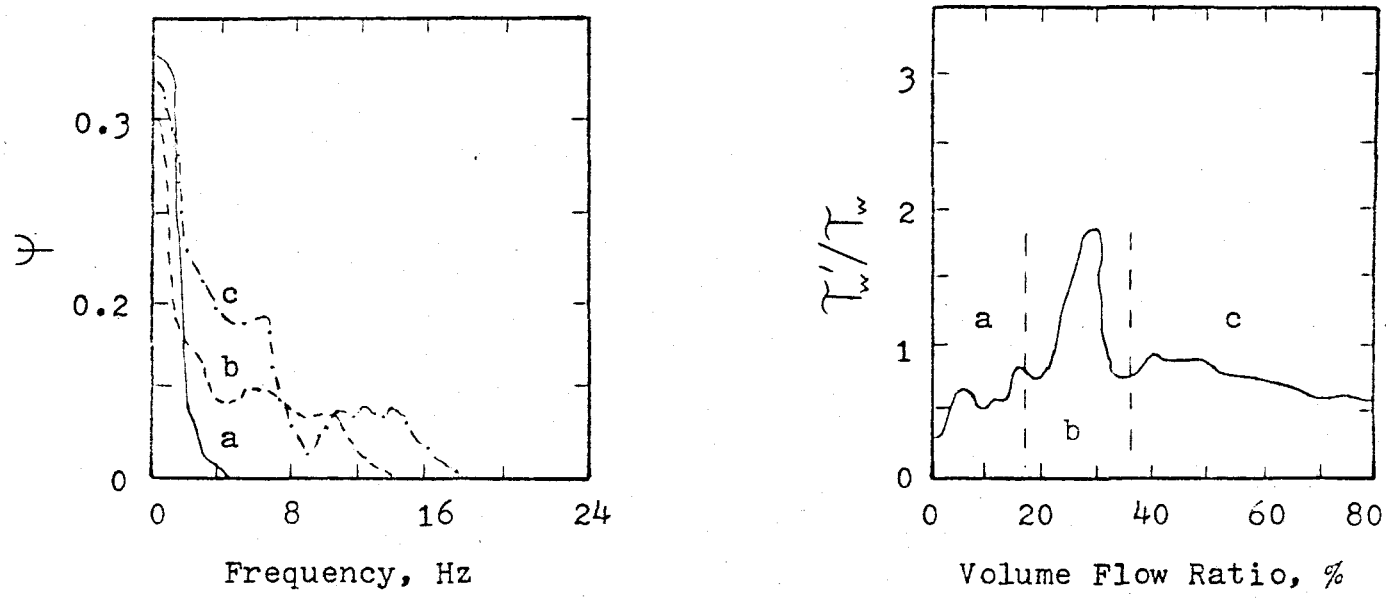

Fig. 2-3. Results of the study by Kutateladze et al on wall shear stress fluctuations in vertical two-phase flow. Observed flow regimes: a, bubble; b, slug; c, annular.

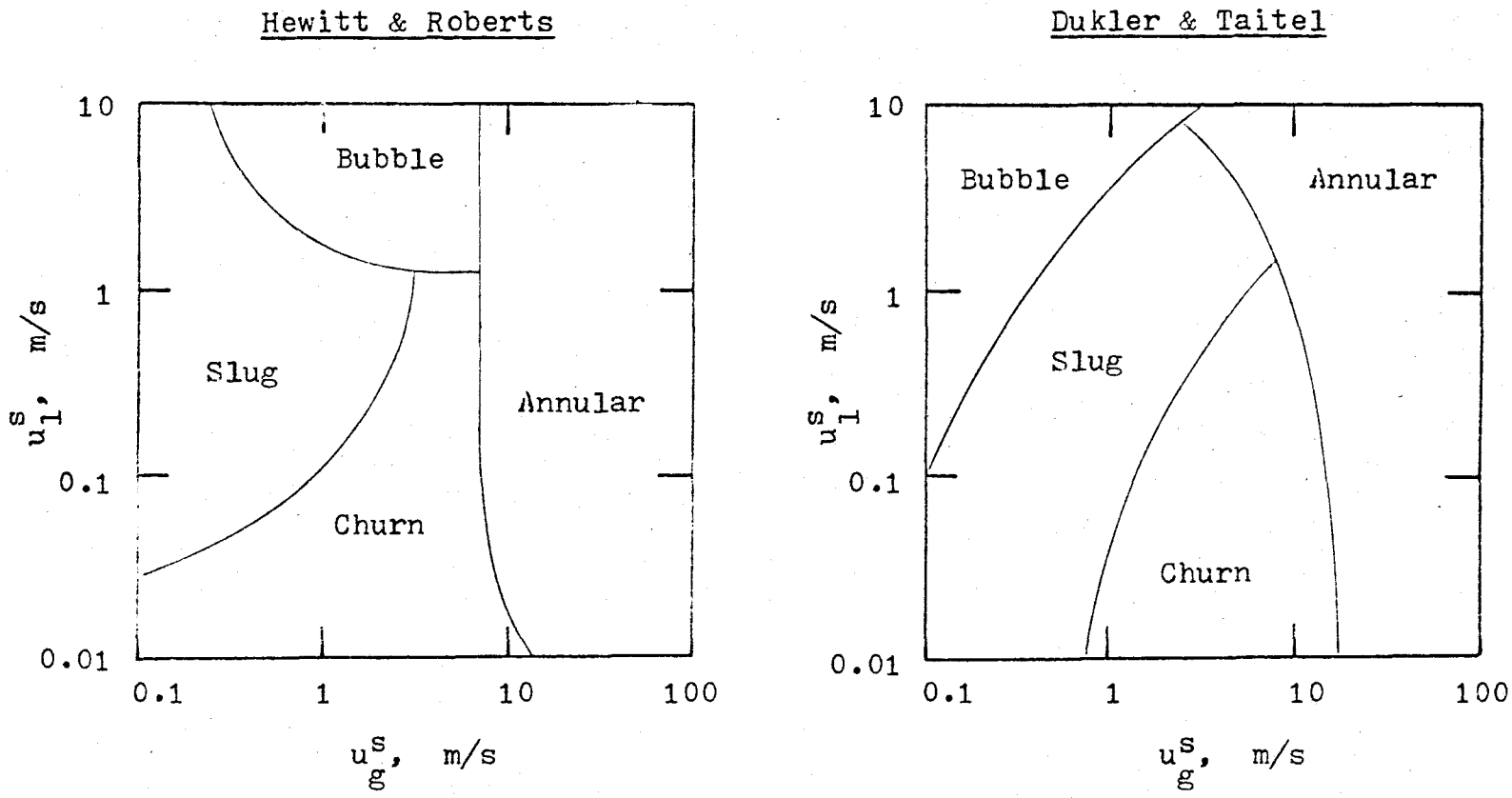

Fig. 2-4. Comparison of the empirical flow regime map of Hewitt & Roberts with the theoretical map of Dukler and Taitel. Both maps are for vertical air-water flow at atmospheric pressure in a 32 mm tube.

Dukler and Taitel, one perceives a similarity. The divergence for superficial liquid velocites above 1 m/s could be attributed to the fact that the flow is quite chaotic in this region and thus the regimes ambiguous. The equations used by Dukler and Taitel to construct their map follow.

Bubble-slug. The bubble-slug transition should occur at the point at which the discrete bubbles in a bubble flow are compelled to agglomerate due to increased bubble density as the gas flow rate is increased. From knowledge of the bubble rise velocity relative to the liquid, and assuming that the point of bubble coalescence takes place at a void fraction of 30%, Dukler and Taitel propose that this transition is defined by

$$u_l^s = 2.33\, u_g^s - 1.07\, (g\, (\rho_l - \rho_g)\, \sigma / \rho_l^2)^{\frac{1}{4}} \qquad (2.6)$$

The assumption of the void fraction equalling 30% is reported to coincide with experimental observation and to have theoretical justification relative to the frequency of collision. This is the only transition found to be independent of the tube diameter.

Slug-churn. The transition from slug to churn flow should occur when the liquid slug bridging consecutive Taylor bubbles shortens to the point where the wake of a bubble disrupts the slug. The transition model must be able to predict the length of the Taylor bubble and liquid slug.

Dukler and Taitel assume that the transition criterion requires that the bubble to slug length ratio equal four. In addition, the void fraction in the slug must be 30% as in the bubble-slug transition model. The following set of equations are then derived from continuity and force balance analyses.

$$u_g = [1.2(u_g^s + u_l^s) + 0.245(g D)^{\frac{1}{2}}]/1.06 \qquad (2.7a)$$

$$u_l = (u_g^s + u_l^s - 0.3 u_g) / 0.7 \qquad (2.7b)$$

$$(u_g + u_f) u^{3/2} = 5.11(u_g - u_l) D (g^5/\nu_l)^{1/6} \qquad (2.7c)$$

$$u_g^s / u_g = 0.56 [1 - (u_g - u_l)/(u_g + u_f)] + 0.3 \qquad (2.7d)$$

A turbulent single-phase friction factor was used to give the wall friction force acting on the liquid film. To obtain the point of transition for a specified superficial liquid velocity equations (2.7a), (2.7b), (2.7c) and (2.7d) are solved in an iterative fashion for the gas velocity, liquid velocity, film velocity and finally the superficial gas velocity, respectively.

Annular-churn, annular-slug. Dukler and Taitel assume that the transition to annular flow takes place when the gas velocity in a churn or slug flow is high enough to break up the liquid slug and support the liquid as entrained droplets and/or an annular film. An analysis of the forces required to suspend an entrained droplet and a liquid film provides

$$u_g^s = [4 \sigma g W (\rho_l - \rho_g)/(3 C_d \rho_g^2)]^{\frac{1}{4}} [1 - (1 / \phi_l)] \qquad (2.8)$$

where the critical Weber number and the drag coefficient C_d are suggested to take on the values 30 and 0.44, respectively. The wall shear stress and void fraction are estimated using the Lockhart-Martinelli correlation (refer to Section 2.4) and accounts for the appearance of the parameter ϕ_l. As ϕ_l is a function of the superficial gas velocity, equation (2.8) requires an iterative solution.

Since ϕ_l is the ratio of the pressure drop of the two-phase mixture to the pressure drop that would exist if the liquid was flowing alone in the tube, at low liquid flow rates the value of ϕ_l goes to infinity. As a consequence, inspection of equation (2.8) shows that the churn-annular transition becomes independent of the liquid flow rate. Wallis (6, p. 339) observed this effect and from experimental data developed the following expression for transition to annular flow at low liquid flow rates.

$$u_g^s = C \left(g D (\rho_l - \rho_g)/\rho_g \right)^{\frac{1}{2}} \qquad (2.9)$$

The constant C can take on a value from 0.75 to 1.0 depending upon the entrance and exit geometries.

In summary, equations (2.6) to (2.9) can be used to predict the existence of a flow regime with knowledge of the flow rates and fluid properties.

2.3 Slug Flow Correlations

Correlations are available to predict the frictional pressure drop and void fraction, based upon the geometry

of the slug flow regime illustrated in Figure 2-2. As the bubble region is nearly one of constant pressure, Griffith and Wallis (12) assumed that the pressure drop could be attributed solely to the liquid slug moving at its mean velocity. The frictional pressure drop would then be given by the expression

$$\Delta P_F / L = 2 f (u^s)^2 \rho_l (1 - \alpha) / D \qquad (2.10)$$

where $u^s = u_g^s + u_l^s$ and $(1 - \alpha)$ represents the length of tube occupied by the slug. The Blasius relation for smooth pipes can be used to calculate the friction factor

$$f = 0.0791 (Re)^{-\frac{1}{4}} \qquad (2.11)$$

where in this application $Re = u^s D / \nu_l$. With this correlation Griffith and Wallis were able to predict the pressure drop in fully developed slug flow to within $\pm 20\%$ of the measured values. Golan (13) reported an accuracy of $\pm 10\%$.

Hughmark (14) suggested a similar correlation, in which he assumed an average liquid velocity acting along the entire tube length. Under these conditions

$$\Delta P_F / L = 2 f (u_l^s / (1 - \alpha))^2 \rho_l / D \qquad (2.12)$$

where the friction factor can again be calculated using the

Blasius relation, but with $Re = u_l^s D / \nu_l (1 - \alpha)$.

Zuber and Findlay (15) presented a general expression for the void fraction in a two-phase flow that takes into account the effect of nonuniform flow across the duct as well as the local relative velocity between the phases. Specific analyses were given for the bubble and slug flow regimes. Beginning with the rise velocity of a large bubble in a stagnant liquid, which is given quite accurately by $u = 0.35 (g D)^{\frac{1}{2}}$, the absolute velocity of the Taylor bubble is

$$u_g = C (u_l^s + u_g^s) + 0.35 (g D)^{\frac{1}{2}} \qquad (2.13)$$

The constant C relates the abolute velocity of the slug to the mean velocity and varies between 1.2 and 1.65. The higher value would reflect a parabolic void profile in the liquid slug, as would exist if there was a high concentration of bubbles. Since $u_g = u_g^s / \alpha$, the void fraction must be

$$\alpha = u_g^s / (C (u_g^s + u_l^s) + 0.35 (g D)^{\frac{1}{2}}) \qquad (2.14)$$

This form of relation for the void fraction has been presented on earlier occasions by a number of authors, including Griffith and Wallis.

2.4 Annular Flow Correlations

The correlation of Lockhart and Martinelli (16) is by far the most widely used method for estimating pressure drops in gas-liquid flows, regardless of the flow regime. However the underlying assumptions are best satisfied by

the conditions of the annular flow regime. The correlation considered each phase to flow separately, occupying a clearly defined portion of the channel. It was further assumed that the conventional single-phase frictional pressure drop relations could be applied along each phase's flow path. The flow regime was not considered, instead four flow types were defined based upon whether the phases were flowing 'viscously' or 'turbulently' as indicated by the individual superficial Reynolds numbers.

Lockhart and Martinelli worked with two parameters ϕ and X, which were defined as

$$\phi^2_{g \text{ or } l} = (dp_F/dz)/(dp_F/dz)_{g \text{ or } l} \qquad (2.15)$$

$$X^2 = (dp_F/dz)_l/(dp_F/dz)_g \qquad (2.16)$$

where $(dp_F/dz)_g$ and $(dp_F/dz)_l$ are the frictional pressure gradients for the gas and liquid phases, flowing alone in single-phase flow. In annular flow both phases are usually flowing 'turbulently', in which case, with the Blasius form for the friction factor, from equation (2.16) is derived

$$X^2 = (u^s_l/u^s_g)^{1.75} (\rho_l/\rho_g)^{0.75} (\mu_l/\mu_g)^{0.25} \qquad (2.17)$$

The correlation ignores the interaction between the phases, and Lockhart and Martinelli presented ϕ^2 as a function of X^2 on empirical graphs. However Chisholm (17) later presented a basis for the correlation in which the

effect of interfacial shear was included. He was able to obtain ϕ_1^2 in terms of the parameter X^2, the void fraction and a function of the interfacial shear stress. For turbulent flow, ϕ_1^2 is best given by

$$\phi_1^2 = 1 + 20/X + 1/X^2 \qquad (2.18)$$

The two-phase frictional pressure drop can then be calculated using equations (2.15), (2.17) and (2.18).

The correlation was based upon data from horizontal pipe flow. Reports of its successful application to vertical annular flow have been quite favourable. Typical accuracy is -40% to +10% (18) with the best being reported as -15% to +0% (13). Most results indicate that Lockhart and Martinelli predicts frictional pressure drops that are too low. Davis (19) modified the correlation to better account for gravity and mass flow effects experienced in vertical flow. A Froude number was added to the parameter X^2 to give

$$X_D^2 = 0.0361 \left[(u^s)^2 / (D g) \right]^{0.37} X^2 \qquad (2.19)$$

Davis achieved an accuracy of ± 20% for liquid Reynolds numbers greater than 8,000. Golan (13) reported an accuracy of ± 10% when using the Davis modified parameter.

The Lockhart and Martinelli correlation can be used to obtain the void fraction. In annular flow

$$\Delta P_F / L = 2 f_{tp} \left(u_1^s / (1 - \alpha) \right)^2 \rho_1 / D \qquad (2.20)$$

where f_{tp} is the effective two-phase friction factor. The pressure drop when the liquid phase flows alone is given by

$$(\Delta P_F / L)_l = 2 f (u_l^s)^2 \rho_l / D \qquad (2.21)$$

Substituting equation (2.20) and (2.21) into equation (2.15) results in

$$\phi_l^2 = (1 - \alpha)^{-2} f_{tp} / f \qquad (2.22)$$

If there is no entrained liquid in the core

$$\alpha = (D - 2m)^2 / D^2$$

or

$$D \cong 4 m / (1 - \alpha) \qquad (2.23)$$

where m is the liquid film thickness.

The Reynolds number of the liquid film, $Re = 4 m u_l^s / \nu_l (1 - \alpha)$, is then equal to the Reynolds number when the liquid is flowing alone in the tube, $Re = D u_l^s / \nu_l$ This implies that $f_{tp} = f$ and from equation (2.22)

$$\phi_l^2 = (1 - \alpha)^{-2}$$

or

$$\alpha = 1 - (1 / \phi_l^2) \qquad (2.24)$$

This relation has been developed by several authors, Chisholm (17) was one of the first. The accuracy of equation (2.24) is judged to be a strong function of the degree of entrainment (18). Oshinowo and Charles (20) found it to be accurate to ±10%.

CHAPTER 3

PREVIOUS WORK AND THEORY ON THE ELECTROCHEMICAL METHOD

The electrochemical method, also referred to as the diffusion controlled electrolysis method or redox method, is a means of measuring the rate of mass transfer at a solid-liquid interface in a fluid flow. Electrodes are mounted flush with the wall to make up an electrochemical cell and an electrolyte is circulated through the channel. This is illustrated in Figure 3-1. As will be explained later in this chapter, the conditions of operation are such that the limiting cell current is a direct measure of the mass transfer coefficient. The mass transfer coefficient can be used to provide the velocity gradient and thus the shear stress at the wall, or by analogy, the heat transfer coefficient. Three values of the mass transfer coefficient can be obtained:

1. Space- time-averaged value
2. Local time-averaged value
3. Local fluctuating value

The time-averaged value of the limiting current of a ring electrode gives the space- time-averaged value of the mass transfer coefficient. A point or wire electrode can provide the local fluctuating value, though one must compensate for edge effects in the subsequent analysis of the data.

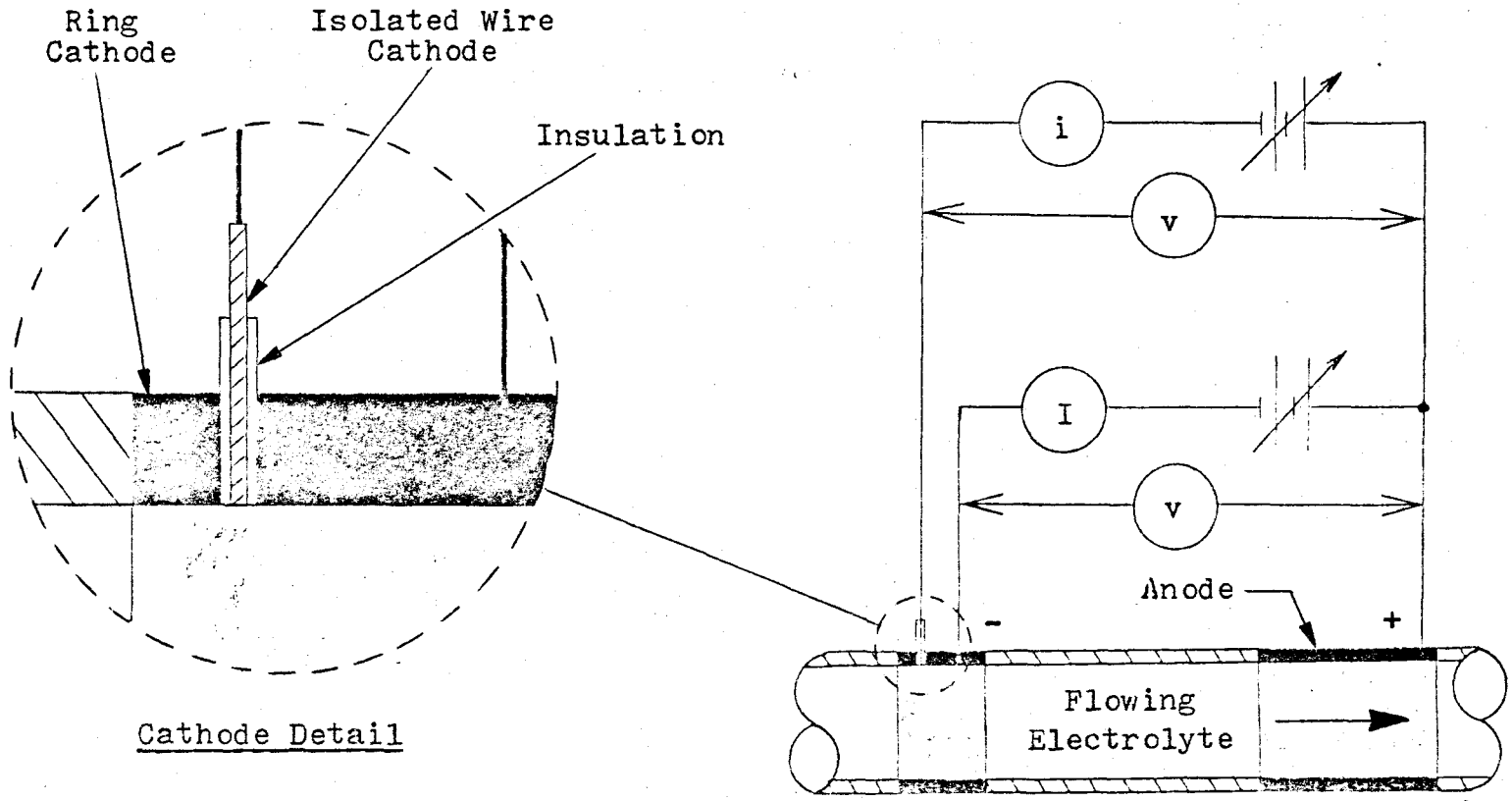

Fig. 3-1. Basic electrical circuit for the electrochemical method.

Placing an electrically insulated wire electrode within a larger electrode will help to eliminate any edge effects, as the larger electrode can be used to develop the concentration boundary layer. This 'isolated' point electrode can be used to obtain either the instantaneous or time-averaged local mass transfer coefficient.

Hanratty noted that the wire electrode is analogous to the constant-temperature hot-wire anenometer in that the surface concentration is kept constant and the current flowing in the circuit is related to the wall shear stress. The advantages over the hot-wire anemometer are that no disturbances to the flow are introduced and measurements are made adjacent to the wall. The electrochemical method has been used in place of conventional heat transfer techniques because it is inherently more accurate and can provide larger quantities of more detailed information in a more practical fashion.

The method has been used in single-phase systems for the past thirty years. Mass transfer in annuli (21), square ducts (22), rectangular channels (23) and tubes (24,25,26) have been examined. Its application to heat transfer studies has ranged from forced convection in tubes (27) to free convection from cylinders (28) to the complex geometry of a shell and tube heat exchanger (29). The fluctuating value of the mass transfer coefficient has been used to gain an understanding of the nature of turbulence near the wall (30,31). This has been only a very brief outline of the application

of the electrochemical method to single-phase flow. Reports of experiments in two-phase flow have been those of Sutey (2) on climbing film flows and Kutateladze et al (3,9) on vertical bubble, slug and annular flows. Kirdyashkin (32) reviews the Russian studies in horizontal and vertical two-phase flows.

Mizushina (33) has written a comprehensive review of the subject. The book by Newman (34) is available and it details the fundamental aspects of electrochemistry and the analysis of related problems in convective transport.

3.1 Electrochemical Cell Analysis

In an electrochemical cell, the steady-state rate of mass transfer of an ion from the bulk of a dilute solution to the surface of the electrode is given by (34, p. 9)

$$N = U c - \mathfrak{D} \nabla c - Z \Psi F c \nabla \Theta \qquad (3.1)$$

The three terms on the righthand side represent transport by convection, transport by diffusion due to the concentration gradient, and transport by migration due to the potential field, respectively.

In a system in which there is no actual chemical deposition at the electrodes and thus no net bulk flow, the convection term in equation (3.1) can be dropped. For systems possessing large Schmidt numbers the concentration boundary layer is extremely thin and the curvature of the wall can be neglected. Equation (3.1) can thus be expressed in cartesian coordinates (see Figure 3-2a).

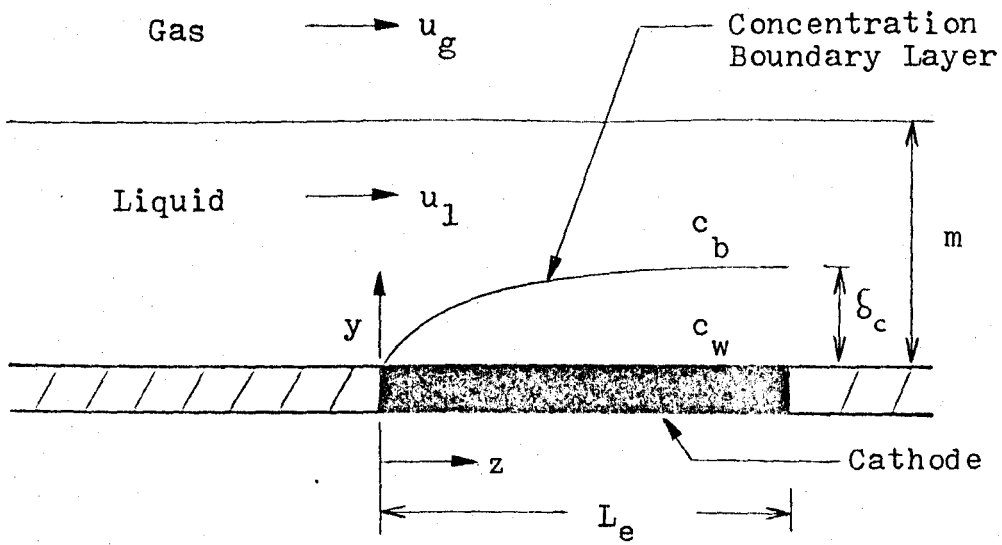

Fig 3-2a. Mass transfer at the wall interface in a two-phase flow.

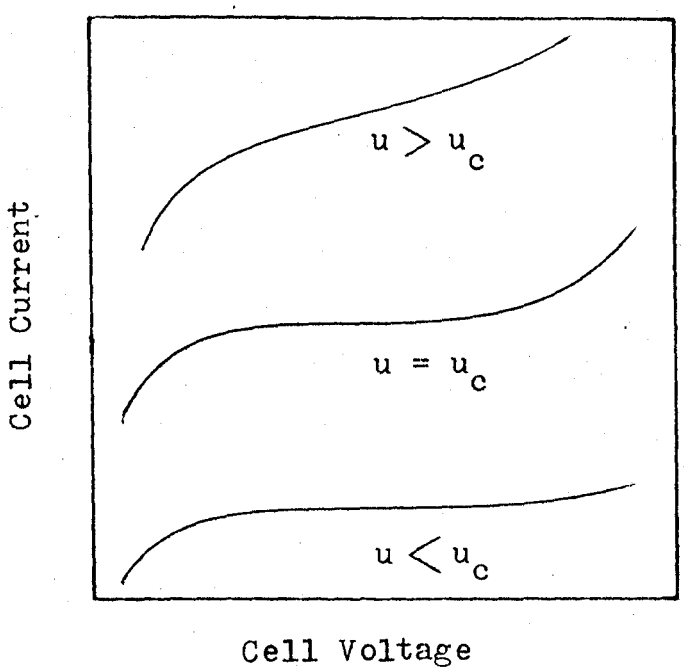

Fig 3-2b. Idealized polarization curves, showing effect of critical velocity.

The migration term can be expressed in an alternate form as

$$- Z \Psi F c \nabla \Theta = I t / (Z a_e F) \qquad (3.2)$$

where the transference number t is the fraction of the current carried by the reacting ion.

Faraday's law relates the rate of mass transfer to the cell current expressed as

$$N = I / (Z a_e F) \qquad (3.3)$$

The mass transfer coefficient is defined by

$$- \mathcal{D} \left(\partial c / \partial y \right)_{y=0} = k (c_b - c_w) \qquad (3.4)$$

Upon substituting equations (3.2), (3.3) and (3.4) into equation (3.1), solving for the mass transfer coefficient provides

$$K = I (1 - t) / (Z a_e F (c_b - c_w)) \qquad (3.5)$$

The most widely used chemical system, and the system used in this study, is equimolar potassium ferricyanide and ferrocyanide in excess sodium hydroxide. The chemical reactions are

At the cathode: $Fe (CN)_6^{-3} + e^- \rightarrow Fe (CN)_6^{-4}$

At the anode: $Fe (CN)_6^{-4} \rightarrow e^- + Fe (CN)_6^{-3}$

The reaction at the anode and cathode are complementary and the bulk concentration should be constant. The sodium hydroxide acts as an indifferent electrolyte, reducing the potential gradient near the electrodes to zero, and thus the migration term in equation (3.1) and the transference number in equation (3.5) go to zero. For 1.0 M sodium hydroxide the transference number can be shown to be less than 1% (2). Thus for an electrochemical system in which there is a large excess of indifferent electrolyte, equation (3.5) can be reduced to

$$K = I / (a_e F (c_b - c_w)) \qquad (3.6)$$

The governing mechanisms are transfer by diffusion to the electrode and reaction kinetics at the electrode. These are commonly referred to as concentration polarization and chemical polarization, respectively.

Equation (3.6) can be further simplified by considering the effect of changing the cell voltage. As the voltage applied between the anode and cathode is increased, the current increases exponentially until the limiting current is reached. At this point the cell is polarized and the concentration at the electrode surface has gone to zero. The current will increase no further until the voltage is increased to the level that a secondary reaction, such as hydrogen evolution, can occur. Figure 3-2b illustrates this behaviour. The plot of current versus voltage is termed a polarization curve and the limiting current I_ℓ is

given by the plateau.

As the fluid flow rate is increased, the limiting current increases. Figure 3-2b shows that there is a critical flow velocity above which a plateau or limiting current is no longer attainable. At this critical velocity the chemical reaction is not fast enough to remove all the ions reaching the electrode surface.

In terms of the limiting current the mass transfer coefficient is given by

$$K = I_{\ell} / (a_e F c_b) \qquad (3.7)$$

By making the area of the cathode much larger than that of the anode, the limiting reaction takes place at the former. The mass transfer coefficient can then be determined from the limiting current, cathode surface area and bulk concentration of the ferricyanide ion.

The potassium ferricyanide and ferrocyanide in excess sodium hydroxide system has found popular usage due to its relative stability and rapid rate of reaction. Schmidt numbers between 1,400 and 34,000 can be attained by varying the concentration of sodium hydroxide. However there are disadvantages. Eisenberg et al (35) first showed that when exposed to light the ferrocyanide decomposes according to

$$Fe\ (CN)_6^{-4} + \text{light} \longrightarrow Fe\ (CN)_6^{-3} + CN^-$$

In alkaline solutions, the ferricyanide decomposes

according to

$$2\ Fe(CN)_6^{-3} + 6\ OH^- \longrightarrow 2\ Fe(OH)_3 + 12\ CN^-$$

and produces a reddish precipitate. Both reactions result in the formation of hydrogen cyanide

$$CN^- + H_2O \longrightarrow HCN + OH^-$$

The hydrogen cyanide is an electrode poison. Depending upon the amount of exposure to light, the buildup of hydrogen cyanide can require disposal of the electrolyte after only a few days of use.

Hicks and Pogotto (36) reported that the ferricyanide reacted with a number of plastics commonly used in the construction of experimental loops. A 3% decrease in the concentration was recorded for both PVC and Lucite in a solution left standing for 200 hours.

In addition to keeping exposure to light to a minumum, the following procedures should be adopted:

1. The electrolyte temperature should be kept constant. The diffusivity is a linear function of temperature and the reaction rate constants vary exponentially with temperature.

2. Ideally the solution should be kept free of dissolved oxygen. This eliminates oxidation of the electrolyte and the cathodic reaction of oxygen at the electrodes. But these effects are time dependent. Sutey (2) found that up to

70% oxygen saturation can be tolerated for four hours and still obtain mass transfer coefficients within 5% of their correct values.

3. The most commonly used electrode material is nickel. For accurate results, the cathode must be scrupulously cleaned before each experiment. A contaminated electrode means that portions of the working surface are blocked and the concentration at the interface is no longer zero. If a cathodic cleaning process is employed, it should be done in a solution separate from that used in the actual experiment because of the oxygen generated.

Once the experiment has commenced, the electrodes can become contaminated due to decomposition products and/or oxygen present in the electrolyte. The actual interactions and mechanisms of contamination are not fully understood, but the result is erroneous measurements.

3.2 Mass Transfer Analysis

For an electrochemical cell in which the reaction takes place only at the electrode-electrolyte interface, a mass balance requires that $\nabla N = 0$. Continuity dictates $\nabla U = 0$. Neglecting the migration term, equation (3.1) yields

$$U \cdot \nabla c = \mathfrak{D} \nabla^2 c \qquad (3.8)$$

The velocity in the z direction being dominant, this reduces to

$$u \, \partial c / \partial z = \mathfrak{D} \nabla^2 c \qquad (3.9)$$

One model of turbulent flow expresses the variables in terms of time-averaged and fluctuating components, having assumed that the flow is characterized by random and rapid fluctuations of velocity, pressure, temperature and concentration about their mean values. Thus the velocity and concentration are expressed in the form

$$u = \bar{u} + u' \tag{3.10}$$

$$c = \bar{c} + c' \tag{3.11}$$

In addition an eddy diffusion coefficient is defined as

$$-\overline{u'\,c'} = \mathcal{E}\,\nabla c \tag{3.12}$$

The concept of an eddy diffusion coefficient does nothing to illuminate the nature of turbulence, but it does provide a method of evaluating the governing equations.

Making use of equations (3.10), (3.11) and (3.12), time-averaging equation (3.9) reduces it to

$$\bar{u}\;\partial\bar{c}/\partial z = (\mathcal{D} + \mathcal{E})\,\nabla^2\bar{c} \tag{3.13}$$

An order of magnitude analysis (31) has shown that only diffusion in the y direction need be considered.

As mentioned previously, the thin concentration boundary layer enables one to neglect wall curvature. It also allows one to assume that the velocity profile is linearly dependent on y, thus $u^+ = y^+$ and

$$\bar{u} = \tau_w\, y/\mu \tag{3.14}$$

Under these conditions, equation (3.13) in dimensionless form becomes

$$y^+ \frac{\partial c^+}{\partial z^+} = \frac{\partial}{\partial y^+}\left[\left(\frac{1}{Sc} + \frac{\varepsilon}{\nu}\right) \frac{\partial c^+}{\partial y^+}\right] \qquad (3.15)$$

The boundary conditions are

$$c^+ = 0 \quad \text{at} \quad z^+ > 0, \quad y^+ = 0$$

$$c^+ = 1 \quad \text{at} \quad y^+ \to \infty$$

$$c^+ = 1 \quad \text{at} \quad z^+ < 0$$

To solve this equation, one must adopt a theory about the nature of turbulence near the wall in order to arrive at the form of the eddy diffusion coefficient, the eddy diffusivity.

For a thin concentration boundary layer, the eddy diffusivity should depend only upon the wall parameters, $\varepsilon/\nu = \varepsilon/\nu\ (y^+)$. Expanding this function in a Taylor series gives for the first term

$$\varepsilon/\nu = b\ (Sc)\ (y^+)^m \qquad (3.16)$$

Using this form for the eddy diffusivity, Son and Hanratty (25) solved equation (3.15) by numerical means, assuming various values for the constants m and b.

For small values of z^+, the boundary layer is so thin that it is essentially laminar in character with $\varepsilon = 0$ and $u^+ = y^+$. Equation (3.15) as solved by Son and Hanratty gives the dimensionless mass transfer coefficient as

$$k^+ = 0.54 \left(z^+ \right)^{-1/3} \left(Sc \right)^{-2/3} \qquad (3.17)$$

The average value over the length of the electrode is given by

$$K^+ = 0.81 \left(L^+ \right)^{-1/3} \left(Sc \right)^{-2/3} \qquad (3.18)$$

This expression for developing mass transfer is identical to the analogous solution of Leveque (36, pp. 363-367) for developing heat transfer to a fluid. He assumed that the thermal boundary layer lay within the viscous sublayer to give a linear velocity gradient. For the case of mass transfer, it is most commonly reported in the form

$$K = 0.275 \left(\mathfrak{D}/L_e \right) (Re)^{0.583} (Sc)^{1/3} (L/D)^{2/3} \qquad (3.19)$$

having assumed that the friction factor could be given by the Blasius relation. The Leveque solution has been found to be in good agreement with experimental results in single-phase turbulent pipe flow for $L^+ < 1{,}000$. Sutey (2) quoted an accuracy of $\pm 8\%$.

The concentration profile becomes fully developed for large values of z^+. In this case, the concentration gradient along the pipe in the z direction is constant and the term $\left(\partial c^+ / \partial z^+ \right)$ is negligible. As shown by Son and Hanratty the solution to equation (3.15) is then

$$K^+ = (m/\pi)\ b^{1/m} \sin (\pi/m)\ (Sc)^{-(m-1)/m} \qquad (3.20)$$

And is independent of the electrode length. The local value of the mass transfer coefficient becomes fully developed

for $L^+ > 1{,}000$. The average value does not become fully developed until $L^+ > 10{,}000$.

Numerous investigators have presented expressions in the form of equation (3.20). They differ in the form of the eddy diffusivity assumed. The more widely used equations are listed in Table 3-1. The relation of Chilton and Colburn has been used successfully in heat transfer studies (29). Notter and Sleicher (40) presented their expression after criticizing the data used by Metzner and Friend (27) as being too high. Metzner and Friend criticized the data of Lin, Moulton and Putnam (41) as being too low. Son and Hanratty's expression has been criticized for its poor data base (40). Van Shaw, Reiss and Hanratty (24) found their data best fit Deissler's theoretical relation.

The reason for the large number of different expressions (Table 3-1 is only a brief listing) proposed for the fully developed mass transfer is thought to be due to the sensitivity of the data to wall roughness effects for mass transfer studies and temperature effects for heat transfer studies.

Shaw and Hanratty performed a statistical fit to their mass transfer data obtained in turbulent pipe flow. Their expression together with the 99.9% confidence limit on the exponent is

$$K_{\infty}^{+} = 0.089 \left(Sc \right)^{-0.704 \pm 0.013} \qquad (3.21)$$

Table 3-1. Relations for the Dimensionless Fully Developed Mass Transfer Coefficient in Single-Phase Turbulent Flow.

Source	Relation
Chilton & Colburn (38)	$K_{\infty}^{+} = 0.116\ (Re)^{-0.075}\ (Sc)^{-2/3}$
Notter & Sleicher (40)	$K_{\infty}^{+} = 0.075\ (Sc)^{-2/3}$
Lin et al (41)	$K_{\infty}^{+} = 0.081\ (Sc)^{-2/3}$
Metzner & Friend (27)	$K_{\infty}^{+} = 0.085\ (Sc)^{-2/3}$
Shaw & Hanratty (26)	$K_{\infty}^{+} = 0.0889\ (Sc)^{-0.704}$
Deissler (39)	$K_{\infty}^{+} = 0.112\ (Sc)^{-3/4}$
Son & Hanratty (25)	$K_{\infty}^{+} = 0.121\ (Sc)^{-3/4}$

This is the most recent relation of those listed in Table 3-1 and is considered to be the most accurate (26).

3.3 Character of the Concentration Boundary Layer

As demonstrated in the analysis given in the previous section, the rate of mass transfer from the tube wall is governed by mechanisms occuring within the concentration boundary layer. If the concentration gradient is assumed linear, then

$$dc/dy = (c_b - c_w)/\delta_c \qquad (3.22)$$

Combining equations (3.4) and (3.22) gives the Nernst diffusion layer equation

$$\delta_c = \mathcal{D}/K \qquad (3.23)$$

Using the Leveque solution, equation (3.19) for the mass transfer coefficient, in dimensionless form the concentration boundary layer thickness becomes

$$\delta_c^+ = 1.24 (L^+/Sc)^{1/3} \qquad (3.24)$$

This relation can be used to estimate the thickness under turbulent conditions. In Figure 3-3 this equation is plotted for a Schmidt number of 1,600, the lowest Schmidt number used in this study. The same relation can be derived for the thermal boundary layer with the Prandtl number replacing the Schmidt number. Figure 3-3 also contains a plot of the thermal boundary layer with a Prandtl number of 10, representative

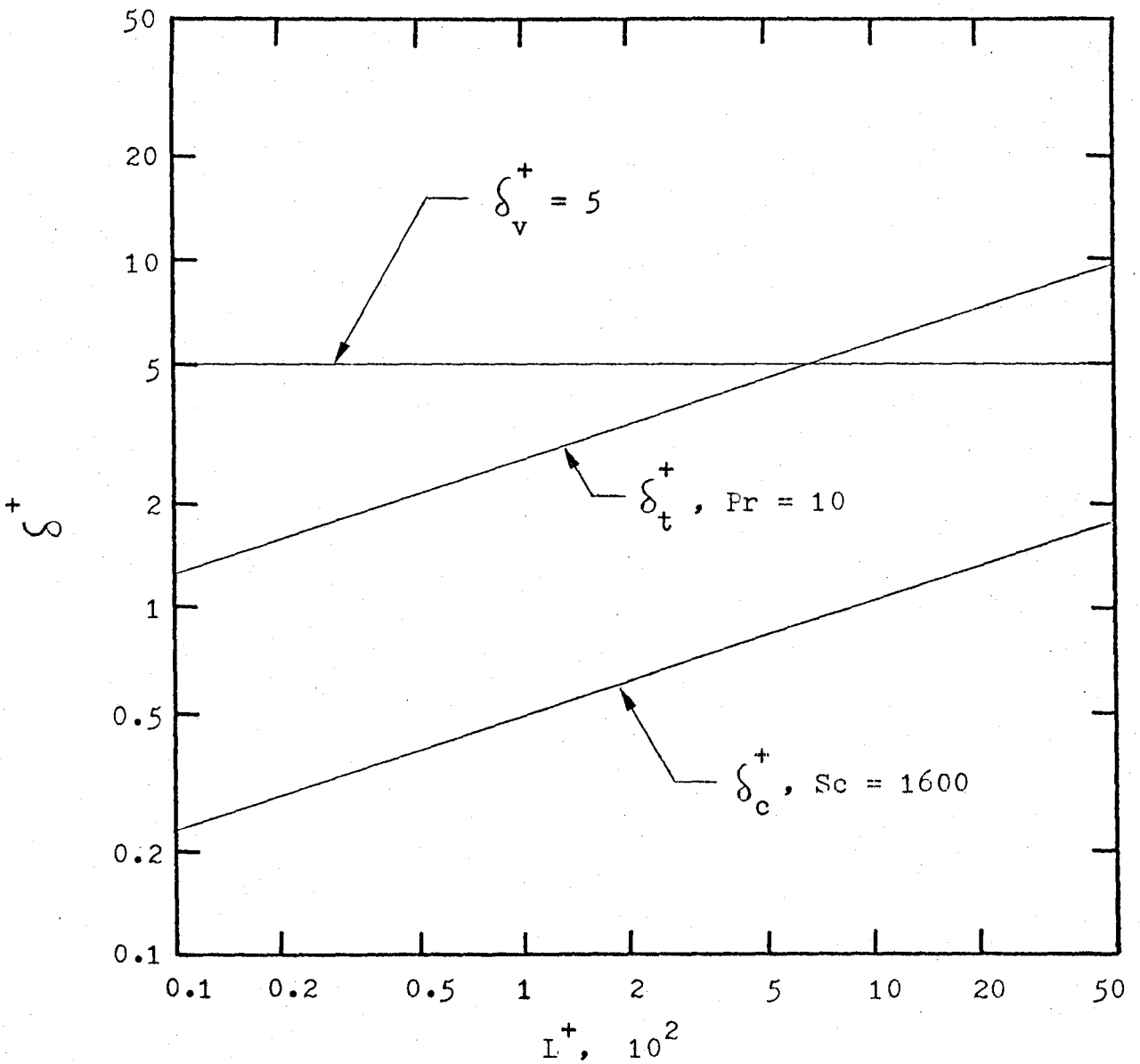

Fig. 3-3. Dimensionless concentration, hydrodyanamic and thermal boundary layer thicknesses versus dimensionless length.

of a 85% glycerol-water mixture. The viscous sublayer, where $u^+ = y^+$, is considered to be bounded by $y^+ = 5$, thus the hydrodynamic boundary layer is also shown with $\delta_v^+ = 5$.

What follows is a discussion of the significance of Figure 3-3 and the character of the boundary layer in hopes of showing the validity of the expressions for mass transfer presented in the previous section. This discussion is made with reference to those systems with Schmidt numbers greater than 1,000.

3.3.1 Single-Phase Flow

The major resistance to mass transfer between a turbulently flowing fluid and a pipe wall is the viscous sublayer at the wall. The degree of resistance is governed by molecular diffusion and convective transport. The concentration boundary layer, as evidenced by Figure 3-3, lies within the viscous hydrodyanamic boundary layer.

Classical theories use the concept of an eddy diffusivity in which the sublayer turbulence is modelled by considering a steady mean flow upon which small turbulent fluctuations have been imposed. This concept was used to develop the expressions presented in Section 3.2 and will be referred to as the 'eddy diffusivity model'.

Experiments have shown that the turbulence structure near a wall is actually characterized by very intense, small scale, three-dimensional ejections or bursts of fluid elements away from the wall (42). The presence of these

disturbances leads to a periodic model of the viscous sublayer in which the wall region is represented by a grid of periodically replaced local viscous elements or patches. This is referred to as the 'periodic' or 'surface renewal' model.

Figure 3-3 shows that the thickness of the concentration boundary layer is on the order of $\delta_c^+ = 1$. Studies have demonstrated (43,44) that the disturbances, as represented by the periodic model, rarely penetrate below $y^+ = 1$. Further studies have been made with the intention of correlating fluctuations in mass transfer with the velocity fluctuations in order to determine the effect that these disturbances have on the concentration boundary layer. The most recent study (30) concludes that the mass transfer fluctuations are not directly related to the velocity fluctuations. The characteristic lengths were observed to differ by a factor of two and the frequencies by an order of magnitude. A turbulence model was proposed to account for these differences (31) which assumed that the eddies were severely damped within the sublayer.

Analyses of mass transfer in turbulent flow using the concept of surface renewal are available. Banerjee (45) presented a theoretical model linking the surface renewal rate to energy dissipation in the boundary layer to give in dimensionless form

$$K_\infty^+ = 0.134 \left(Sc \right)^{-2/3} \qquad (3.25)$$

This expression is similar to those derived from eddy diffusivity models.

With the aid of the computer the unaveraged mass transfer equations have been solved, varying the frequency and magnitudes of the velocity fluctuations as dictated by experimental measurements (46). Again, the frequency of the mass transfer fluctuations were found to be much lower than the basic frequencies associated with the velocity.

Pinezewski and Sideman (47) presented a model of mass transfer in turbulent flow in which the boundary layer is considered laminar ($u^+ = y^+$) and disturbances do penetrate to the wall at a renewal frequency much lower than the frequency exhibited outside of the wall region. The fluid is considered to move a characteristic length before it is disrupted by the disturbance. Their final expression is equivalent to the Leveque solution with a characteristic length of $L^+ = 1{,}740$, which results in

$$K^+ = 0.0671 \quad (Sc)^{-2/3} \qquad (3.26)$$

This expression is empirical as the characteristic length and fluctuation period were chosen so that the final result fit experimental mass transfer data. Equation (3.26) agrees with the eddy diffusivity relationships proposed by Shaw and Hanratty (26) to within $\pm 5\%$ for Schmidt numbers from 1,000 to 10,000.

In conclusion, the eddy diffusivity model does not

represent the actual physical processes taking place near the wall in turbulent flow, but it will predict the rate of mass transfer to the same degree of accuracy as the more realistic periodic models. In addition, the concentration boundary layer can be modelled as having a linear velocity profile.

The thinness of the concentration boundary layer, though providing a form of shielding from outside influences, could in turn lead to an overriding sensitivity to wall roughness. However Dawson (22) studied the effect of wall roughness and concluded that as long as the roughness lay within the concentration boundary layer, the mass transfer rate would be unaffected.

3.3.2 Two-Phase Flow

There have been no investigations directed at the nature of turbulence in the boundary layer in two-phase flow. Any analyses needing information about the turbulence near the wall have been required to use single-phase relationships. This approach has been successfully applied to annular flow (7, p. 60) with single-phase turbulent velocity profiles applied to the liquid film. This would lead one to suggest that the single-phase mass transfer relations could be applied to two-phase flow, especially so in view of

the relative thinness of the concentration boundary layer and its 'insulation' from processes occurring in the core region. The only two mass transfer studies actually performed in two-phase flow (2,3) used the Leveque solution in their analyses.

There have been heat transfer studies performed in slug flow (48) in which the measured values of the heat transfer coefficient were up to twice as large as those predicted by the Leveque solution for turbulent heat transfer. This enhancement in heat transfer has been well documented (49) and is thought to be due to increased convective cooling from the downflowing liquid film adjacent to the Taylor bubble and the resultant radial mixing in the liquid slug. Before it is suggested that by analogy a similar increase in the mass transfer coefficient should be expected, Figure 3-3 shows that the thermal boundary layer is five times as thick as the concentration boundary layer. The Prandtl number used corresponds to that used in the previously referenced heat transfer study. The thinness of the concentration boundary layer could well shield it from the influence of the Taylor bubble in the core.

3.4 Application to Wall Shear Stress Measurement

The following relations can be used to calculate the wall shear stress from the measured mass transfer coefficient in single-phase flow:

For $L^+ < 1{,}000$, from the Leveque solution, equation (3.18)

$$\tau_w = 1.896 \, (K)^3 \, L_e \, \rho_l \, (Sc)^2 / \nu_l \qquad (3.27)$$

For $L^+ > 10{,}000$, From Shaw and Hanratty's fully developed relation, equation (3.21)

$$\tau_w = 126.5 \, (K_\infty)^2 \, \rho_l \, (Sc)^{1.408} \qquad (3.28)$$

These relations were derived by solving for the wall shear stress through the friction velocity. They should also be applicable to two-phase flow for the reasons discussed earlier in this chapter.

CHAPTER 4

APPARATUS AND PROCEDURE

4.1 Loop and Test Section

A loop was constructed to circulate a fully-developed two-phase mixture of gaseous nitrogen and liquid electrolyte through a vertical test section. A schematic of the loop is shown in Figure 4-1.

4.1.1 Description

The electrolyte was circulated in a closed loop formed by the reservoir, pump, mixer, entrance length and test section. A bypass was installed in order that the electrolyte could be circulated in isolation of the test section. As the electrolyte is corrosive, all components were of plastic or stainless steel construction.

The nitrogen flowed through an open loop formed by the nitrogen cylinder, mixer, entrance length, test section and reservoir, where it was separated and then vented. The safety relief valve acted to regulate a gas cover in the reservoir of 120 kPa(a). A line was installed directly between the nitrogen cylinder and reservoir for deoxygenation purposes, enabling nitrogen to be bubbled through the liquid in the reservoir.

The electrolyte was initially circulated with a plastic swimming pool pump, driven with a 3/4 HP motor. The

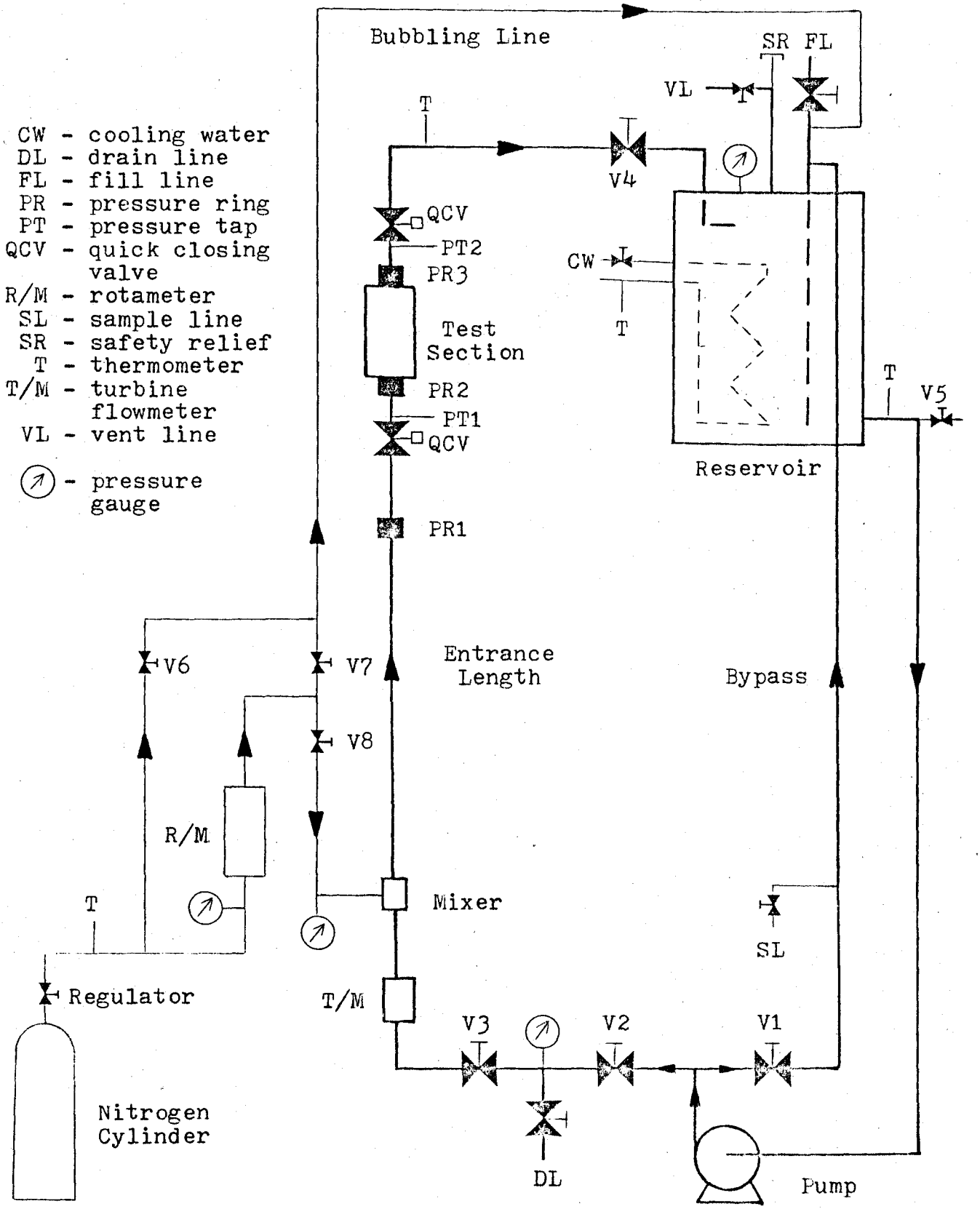

Fig. 4-1. Experimental loop.

impeller of this pump failed after two months service. It was replaced by a more suitable Chemtrol centrifugal pump, driven with a 1 HP motor. The pump casing, impeller and shaft were all moulded polyvinyl chloride (PVC) and the seals were ceramic. The piping was PVC and, excepting the entrance length, 38 mm inside diameter. The entrance length was 13 mm PVC piping and 170 diameters in length to ensure that the flow in the test section was fully-developed. The reservoir was a 95 litre black, polyethylene, neutralization tank with bolt-on cover. All valves for the liquid side were PVC ball valves, excepting V2 and V3. The electrolyte flow rate was controlled with throttling valves V2 (PVC) and V3 (stainless steel).

The flow rate of the electrolyte was first measured with one of three available Flow Technology turbine flowmeters. Two of these units had to be removed from service due to bearing failures. The existing steel ball bearings were to be replaced by tungsten carbide journal bearings. The three units could not be modified in time and the experiments were completed using a Dwyer liquid rotameter. Before the last experiment was finished, the plastic body of the rotameter cracked, and the liquid flow rate had to measured using the throttling valve V3. The number of turns of the valve for a measured flow rate had been previously calibrated, with five turns for full scale.

All the lines between the nitrogen cylinder and mixer

together with the bubbling line to the reservoir were copper with Swagelock fittings. They were isolated from the rest of the loop with stainless steel check valves. Nitrogen flow rates were measured with a Fischer and Porter rotameter, with two floats available for high and low flow rate capacities. Flow rate and pressure were controlled with the throttling valve V8 and the cylinder regulator.

The mixer was constructed from Lucite. The gas was blown radially inward, through four 1.6 mm holes equally spaced around a 25 mm tube, into the upwards flowing liquid. At high gas rates, by delivering the nitrogen to the mixer at a pressure higher than that of the upstream liquid flow, the gas would accumulate in the core with the liquid flowing as an annulus around it. Thus the entrance effect was that of a liquid annular slot injector. This should have resulted in a low degree of liquid entrainment, if the developed flow regime was annular (18).

The liquid temperature was controlled with a cooling coil made up from a 6 m length of 6.35 mm stainless steel tube and placed in the reservoir. Cooling water came from the building supply. The cooling water flow rate was manually adjusted with a throttling valve. Temperature was measured with mercury thermometers.

The test section is illustrated in Figure 4-2. It consisted of three nickel ring cathodes 1.6, 3.2 and 6.4 mm in thickness, and a 25 mm thick nickel anode, all sand-

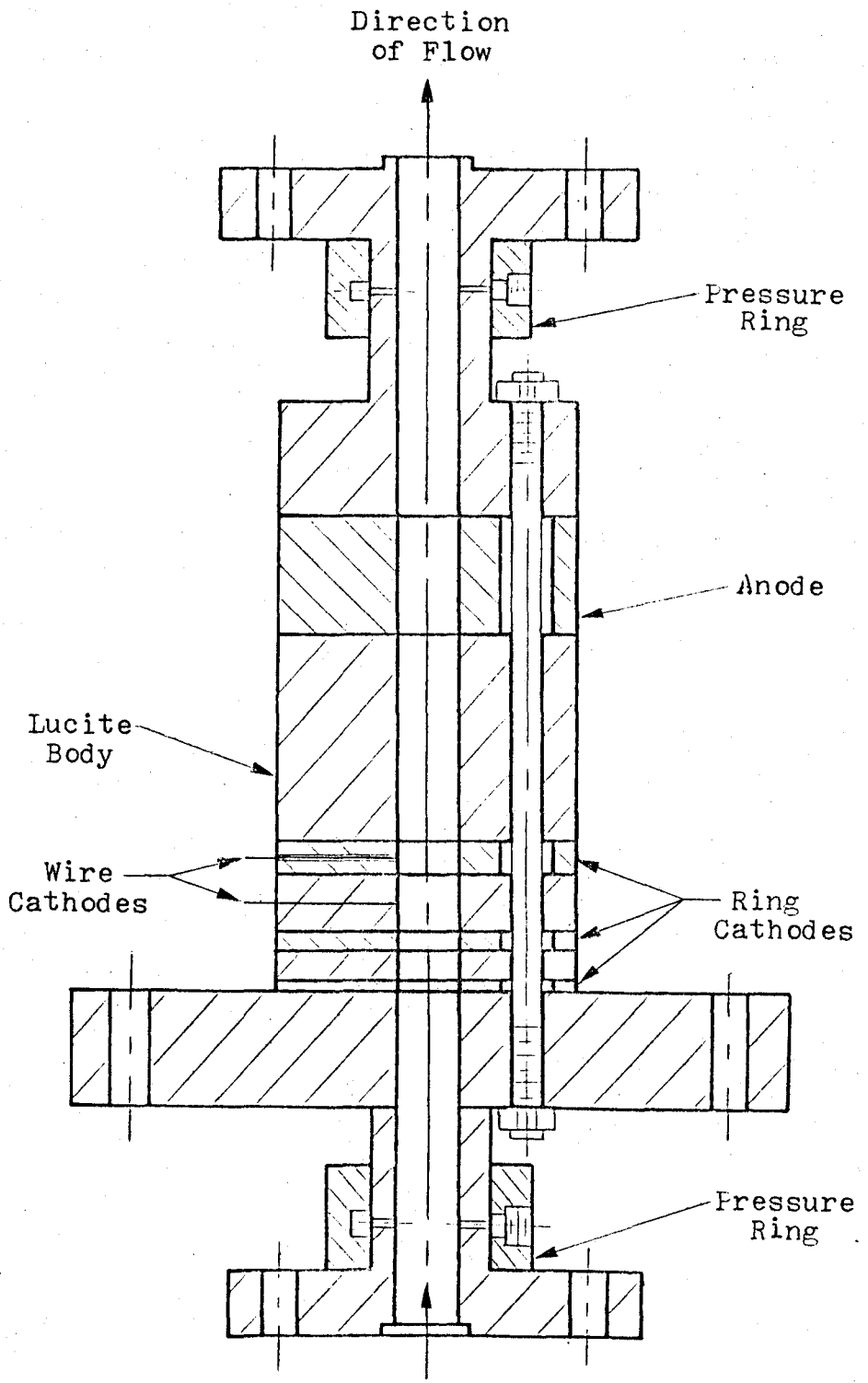

Fig. 4-2. Test section.

wiched between Lucite rings. The rings were held in place with four stainless steel bolts. The test section was reamed when assembled in order that all surfaces would be mated flush. The test section had to be disassembled for cleaning purposes prior to each experiment. Locating pins were initially employed for correct positioning after reassembly. These pins were later discarded in favour of a mandrel. Two 0.5 mm platinum wires were inserted into the 6.4 mm ring cathode. They were epoxied into place, surrounded by an insulating plastic sheath and the tips polished flush with the inside wall of the ring cathode. These isolated wire electrodes provided the fluctuating values of the local mass transfer coefficient, the signals being fed to a spectrum analyzer. Four 0.5 mm platinum wires were also placed in the Lucite ring between the 6.4 mm and 3.2 mm cathodes. The ring cathodes were insulated from one another and operated on an individual basis to provide spatial averages of the mass transfer coefficient.

The test section possessed two pressure rings. Each ring acted as a manifold for four equally spaced 0.8 mm pressure taps, with an annulus connecting the taps to a single port where a pressure transducer was directly attached. An additional ring was located 600 mm upstream of the test section.

4.1.2 Preparation

Prior to an experiment the test section was disassembled and the nickel cathodes cleaned. The standard

cleaning procedure involved scrubbing the electrodes with a commercial cleanser, followed by 2 N hydrochloric acid. They were then treated cathodically for fifteen minutes, in a solution of 5% sodium hydroxide at a current density of 20 mA/cm^2. The test section was then reassembled and immediately installed in the loop.

The loop was then filled with 140 litres of deionized water, displacing all the air in the system. The water had been previously deaerated by pulling a vacuum over it as stored in 20 litre bottles. Next the water was displaced out of the loop through valve V5, by bubbling nitrogen into the reservoir, until the volume remaining in the loop had been reduced to 90 litres. This bubbling served to further remove any dissolved oxygen. Finally the test section was isolated by closing valve V4, displacing the water in the entrance length, introducing nitrogen through the mixer and finally closing valve V3.

At this point the sodium hydroxide was added in solid form to the reservoir via the fill line. The heat of solution brought the water temperature up to about 35 °C. The pump and cooling water were turned on. Fifteen minutes was required to mix the sodium hydroxide and bring the temperature of the solution down to room temperature. At this point the potassium ferri- and ferrocyanide were added, also in solid form. After the electrolyte had been adequately mixed and the loop temperature had reached equilibrium at 25 °C, valves

V3 and V4 were opened. The experiment was then begun. Total elapsed time from the cleaning of the electrodes to the start of the experiment averaged two hours.

4.2 Mass Transfer Measurements

The electrical hookup to the electrodes was basically that shown in Figure 3-1. The supply for the ring cathodes was a Hewlett Packard 6200B D.C. power supply. The power supply for the wire electrodes was a 6 volt lead-acid battery. Both supplies were controlled by individual 10 turn precision potentiometers.

The ring cathode current was measured directly with a Fluke 8000A digital multimeter for the single-phase experiments. For the two-phase experiments, the time-averaged value of the cathode current was measured with the circuit illustrated in Figure 4-3. The voltage across a 10.0 ohm sensing resistor was integrated over a preset time interval. The time constant of the integrator was 100 s. The output of the integrator divided by a tenth of the integration time provided the time-averaged value of the current. An integration time of 20 s was adopted. The error in the analogue circuit, determined by integrating reference D.C. voltages, was measured to be less than 1%.

The procedure for determining the limiting current involved rapidly varying the voltage applied to the cell and noting the current. This served to locate the position of the plateau on the polarization curve. Additional readings of the

A = Anode R_s = 10.0 Ohm Sensing Resistor

C = Cathode PR = Pressure Ring

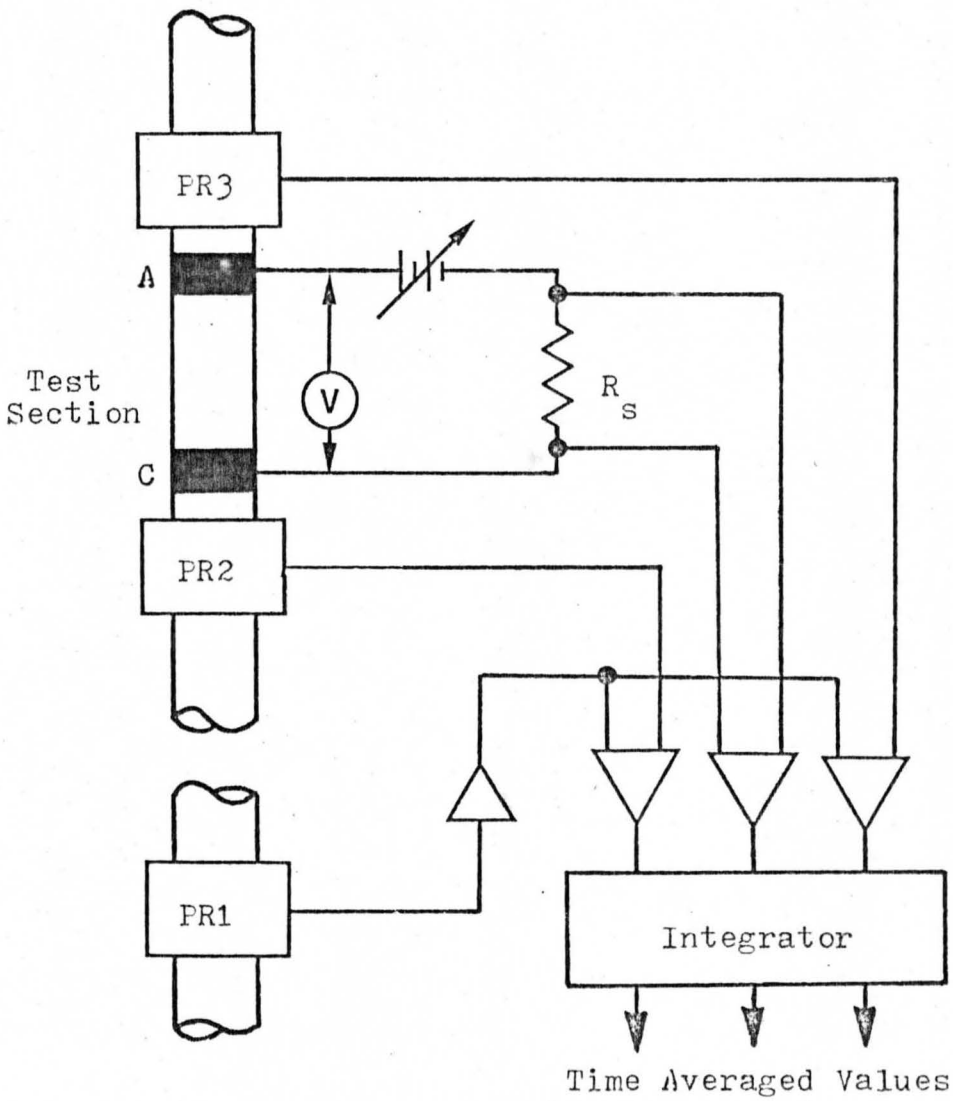

Fig. 4-3. Schematic of circuit used in two-phase experiments for the measurement of time averaged values of ring cathode current and test section pressure drop.

current were then taken spread over the length of the plateau, waiting around a minute at each particular voltage setting before recording the current, to ensure steady-state conditions had been reached. Typical polarization curves obtained in this fashion are shown in Figure 4-4 for single-phase flow, and Figure 4-5 for two-phase flow. The plateaus giving the limiting currents are self-evident.

The isolated wire cathodes were operated by first polarizing the 6.4 mm ring cathode, having predetermined its limiting current. The voltage across the wire electrode and the anode, was then matched with the voltage across the ring cathode and the anode. The fluctuating current in the wire electrode circuit was fed via a sensing resistor to a spectrum analyzer. Details of this circuit are given in Appendix 6.

Initially a sample was drawn from the loop, and the ferricyanide concentration so determined, three times during the course of an experiment. But as it was discovered that the concentration did not change, the standard procedure was to draw only a single sample for each experiment.

To guard against incorrect measurements due to electrode contamination, the limiting current at the highest liquid flow rate, and in most cases at additional flow rates, was checked for excessive drift at the end of every experiment. Readings were to be discarded if the drift was more than 5%. The single-phase experiments lasted about 2 hours,

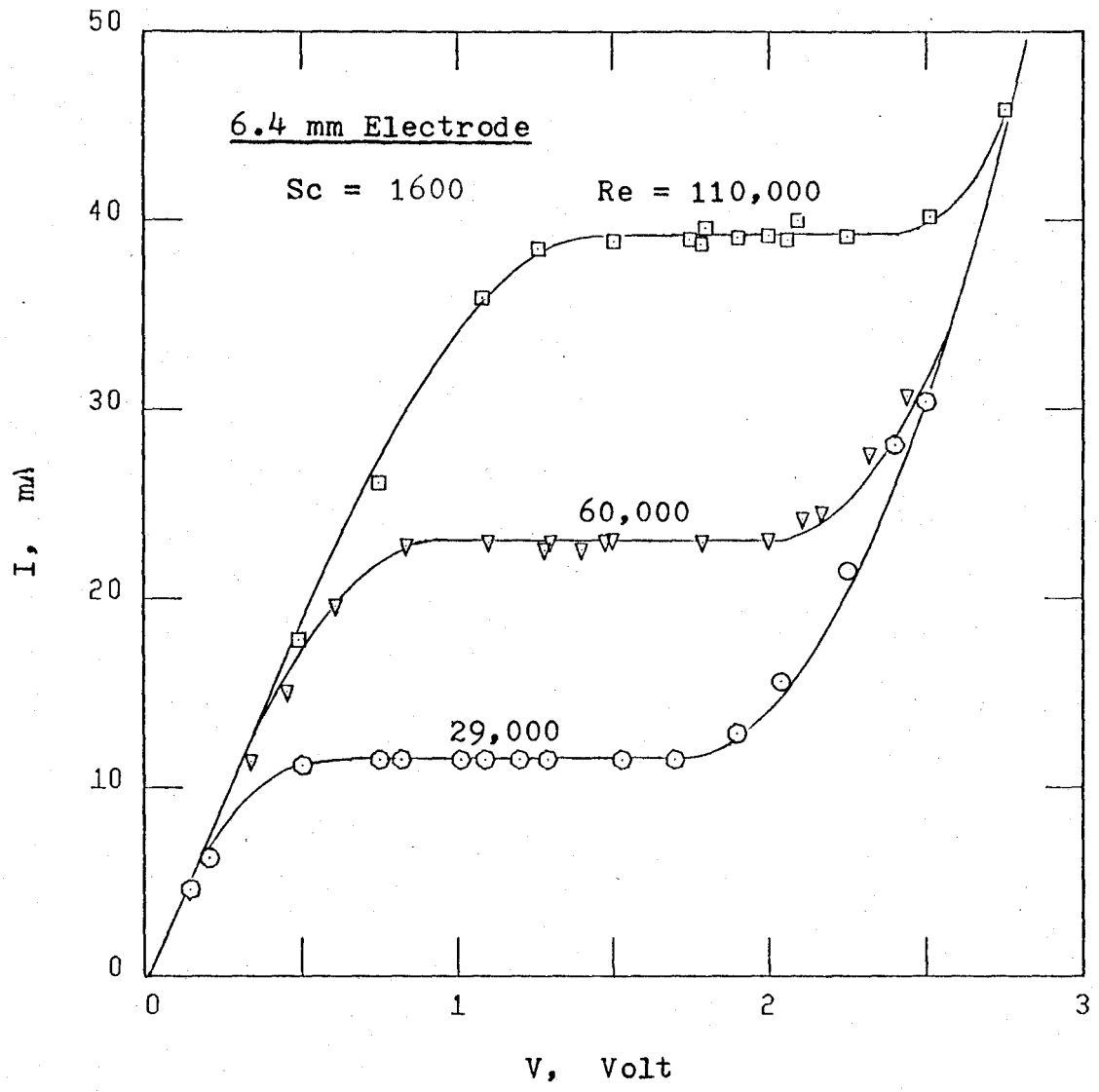

Fig. 4-4. Typical polarization curves obtained in single-phase flow.

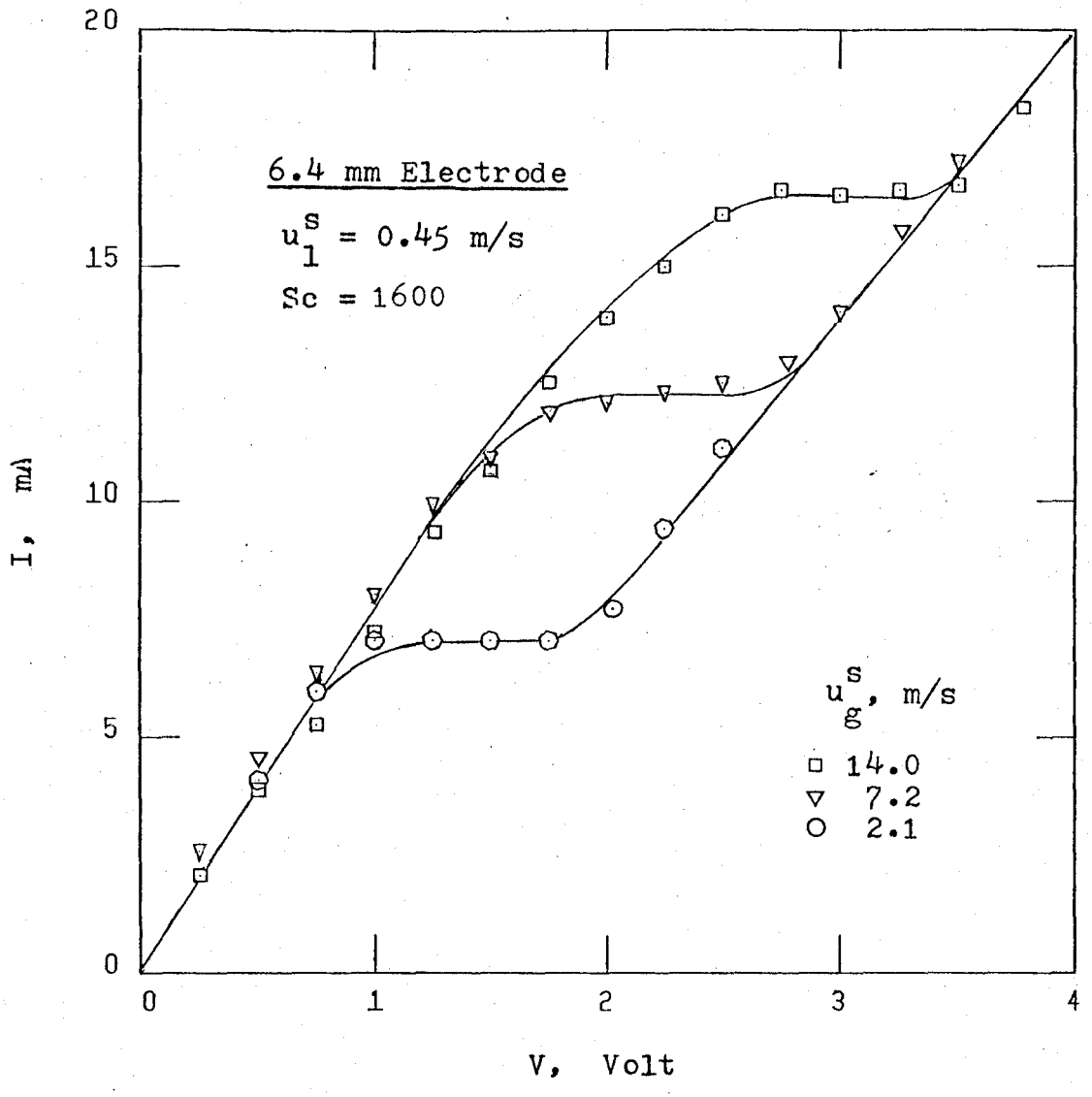

Fig. 4-5. Typical polarization curves obtained in two-phase flow.

the two-phase experiments lasted 5 hours.

If an electrolyte solution was going to be used only once, the water was not deareated before addition to the loop. No single solution was kept for more than five days. However a solution need only be discarded when polarization is no longer attainable. With exposure to light kept to a miminum, other experimenters have been able to use the same solution for up to six months.

4.3 Pressure Drop Measurements

The pressure drop across the test section was obtained using three Validyne differential pressure transducers mounted at the three pressure rings. If manometers had been used, some action would have had to be taken to ensure that the lines were filled with a single phase at all times, otherwise the static head in the lines would be unknown. The mounting of pressure transducers directly onto the pressure rings, though expensive, eliminated this problem. It also facilitated time-averaging. The pressure drops were obtained by differencing the readings of the three transducers.

For the single-phase experiments, the individual transducer readings were read with a Fluke 8800 digital voltmeter. The negative ports of the transducers were interconnected and hooked up to a regulated air supply. The range of the transducers was stepped using 140, 35 and 7 kPa diaphragms at PR1, PR2 and PR3, respectively (refer to

Figure 4-1 or 4-3). When in operation the air pressure on the negative ports was set so that PR3 read close to zero. This arrangement provided maximum sensitivity but could not be used in the two-phase experiments due to the large amplitude of the pressure fluctuations.

In the two-phase experiments, as shown in Figure 4-3, the signals from the transducers were differenced, fed to an integrator and time-averaged in the same fashion as for the ring cathode current.

To correct for the drift exhibited by the demodulators of the transducers, each transducer was calibrated at the beginning and end of each and every experiment.

4.4 Void Fraction Measurements

The average void fraction was obtained with quick-closing ball valves which served to isolate the two-phase mixture in the test section. The valves were pneumatically operated with 1400 kPa(g) nitrogen to give a closure time of 20 ms. Actuation was by means of solenoid valves operated by a relay. The relay also served to provide simultaneous shutoff of the nitrogen supply and pump. The valves closed within 1 ms of each other.

Initially a pressure transducer was used to measure the hydrostatic head and thus the amount of liquid trapped in the test section. This had been thought to be the most convenient and safe method. However problems with transducer drift necessitated the use of the 'drain and measure' method.

The pressure taps shown next to each quick-closing valve in Figure 4-1 were used to vent and drain the test section after closure of the valves.

The void fraction for a particular set of flow conditions was obtained by averaging the results of several measurements. In some cases, such as when slug flow existed, up to twenty measurements had to be taken until the majority of the readings were within 5% of the mean.

Due to time limitations brought on by the temporal nature of electrode contamination, the void fraction measurements were made in an experiment separate from that for the mass transfer and pressure drop measurements. The test section was removed and replaced with a dummy for fear of damage due to the water hammer brought on by the quick-closing valves. The same electrolyte solution was used and the flow settings duplicated.

4.5 Experimental Errors

The estimated experimental error limits on the measured quantities, properties and selected calculated quantities are given in Tables 4-1 and 4-2. Two types of error were considered in the estimates; random errors in the measurements and constant errors, such as those associated with the reading of an instrument. The random errors were estimated by observing the degree of reproducibility of the data from replicate experiments.

As discussed by Acosta (23) the only error associated

Table 4-1. Error Limits of Measured Quantities and Properties.

Quantity	Error
Limiting current	± 1.0 %
Concentration of ferricyanide	± 1.2 %
Concentration of sodium hydroxide	± 0.4 %
Temperature of electrolyte	± 0.3 %
Electrode length	± 0.3 %
Test section inside diameter	± 0.3 %
Pressure transducer readings	± 2.5 %
Distance between pressure rings	± 0.2 %
Liquid volume flow rate	± 2.0 %
Gas volume flow rate	± 2.0 %
Void fraction	± 5.0 %
Ferricyanide diffusivity	± 4.0 %
Electrolyte density	± 0.2 %
Electrolyte viscosity	± 1.0 %
Nitrogen density	± 0.5 %
Nitrogen viscosity	± 1.0 %

Table 4-2. Error Limits of Selected Calculated Quantities.

Quantity	Error
Re, Reynolds number	± 4.0 %
Sc, Schmidt number	± 5.0 %
K, Mass transfer coefficient	± 3.0 %
P, Pressure drop	± 5.0 %
u^*, Friction velocity	± 2.0 %
L^+, Dimensionless length	± 2.0 %
K^+, Dimensionless mass transfer coefficient	± 5.0 %
τ_w, Wall shear stress from developing mass transfer coefficient, equation (3.27)	± 18. %
τ_w, Wall shear stress from fully developed mass transfer coefficient, equation (3.28)	± 14. %
τ_w, Wall shear stress using void fraction and pressure drop, equation (2.5)	± 8. %

with the limiting current for the electrochemical method using a potassium ferri- and ferrocyanide system is the degree of accuracy with which the plateau on the polarization curve can be determined. The uncertainty in the interpretation of the limiting current was estimated to be ±1.0%.

The accuracy of the chemical concentration was derived from the reproducibility of three titrations performed on the same sample. This was recorded to be ±0.3 ml for the ferricyanide and ±0.1 ml for the sodium hydroxide with resulting errors of ±1.2% and ±0.4%, respectively. If the concentration of the ferricyanide had been determined by the potentometric technique as outlined in Hicks and Pagotto (36), the error could be reduced from ±1.2% to ±0.2%.

The temperature of the electrolyte was maintained at 25 ±1 °C. This appears in the diffusivity as as added error of ±0.3%.

There was a significant error introduced by transducer demodulator drift. In the single-phase experiments the pressure drop ranged from 10 to 60 kPa/m, duration was about two hours and there was a demodulator drift of about 1% of full scale. This gave the majority of the pressure drops an accuracy of ±4%. The two-phase experiments had lower pressure drops (4 to 20 kPa/m), longer durations (5 hours) and did not use stepped pressure transducers. These three factors combined to give errors of 10% to 50% for the measured pressure drops in four out of six experiments. Of the remaining two

experiments, one had to be aborted because the transducers were shorted by leaking electrolyte, the other had less than 0.5% of full scale drift to give an accuracy of ± 5% for the majority of pressure drops. This last experiment was the source of the two-phase pressure drops.

The errors for the flow rates were based upon the 95% confidence limits of best line fits to the calibration data. An error of ± 5% was determined for the void fraction measurements based upon the data spread of the replicate measurements.

The reasoning behind the errors quoted for the properties are given in Appendix 2. The errors of the selected calculated quantities fall out from the errors of the measured quantities and properties.

The error in the wall shear stress, as calculated from the mass transfer coefficient, could be reduced by finding more accurate values of the diffusivity and/or improving the method of obtaining the concentration of ferricyanide.

CHAPTER 5

RESULTS AND DISCUSSION FOR SINGLE-PHASE EXPERIMENTS

Ten single-phase experiments, identified as SPR-1 to SPR-10, were performed for familarization with the electrochemical method and debugging of the loop. They were intended to demonstrate the effect of different cleaning techniques, different deareation techniques, and the nature of electrode contamination.

The experiment numbers are quoted in order that one may refer to the original data in Appendix 8.

5.1 Pressure Drops

The calculated frictional pressure drops across the test section are shown in Figure 5-1. Note that the scatter of the data increases when the gravitational pressure drop exceeds the frictional pressure drop, as would be expected. The pressure drops were best correlated using the Colebrook equation

$$f^{-\frac{1}{2}} = -4 \log_{10} (0.27\, \varepsilon/D + 1.26\, f^{-\frac{1}{2}}/Re) \qquad (5.1)$$

with $\varepsilon/D = 0.0025$. This relative roughness corresponded with profilometer measurements made of the test section wall.

For reliable mass transfer measurements, the test section should possess a smooth wall and the frictional pressure drops correlate with the Blasius equation for the

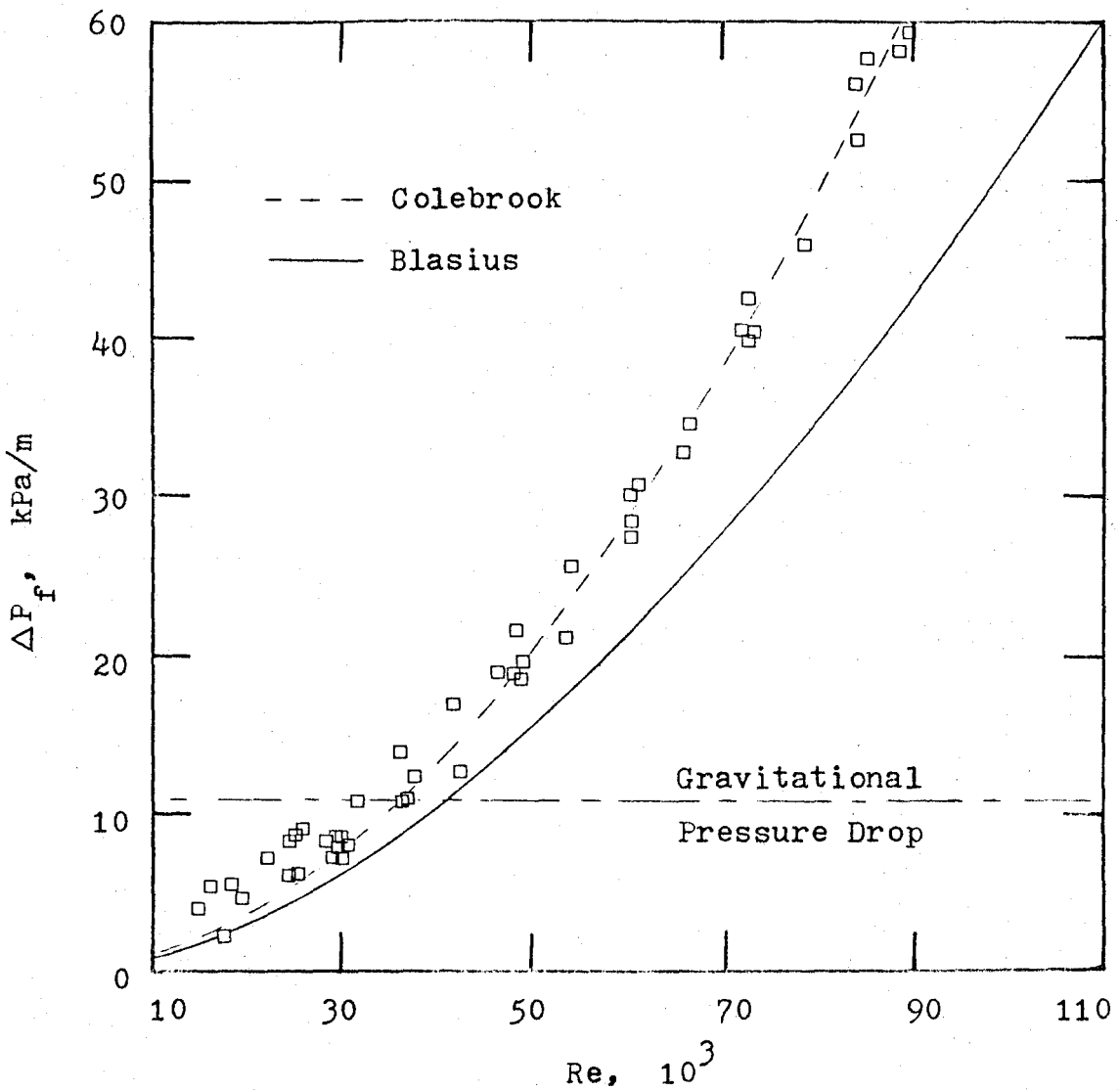

Fig. 5-1. Single-phase frictional pressure drops. The Colebrook relation is calculated with a relative roughness of 0.0025.

friction factor. Evidently this was not the case.

5.2 Mass Transfer Coefficients

Six single-phase experiments, SPR-2, -4, -5, -6, -7 and -9 were performed using the standard procedures as outlined in Chapter 4. The concentration of the ferricyanide was varied from 0.0047 to 0.0072 M. The mass transfer data for these experiments are plotted in Figures 5-2, 5-3, 5-4 and 5-5.

The data for the 6.4 mm electrode is plotted on dimensionless coordinates in Figure 5-2. The data is seen to correlate with the Leveque solution up to $L^+ = 1{,}000$, whereupon it becomes 'fully developed' and matches the predicted value of Metzner and Friend. The values of K^+ predicted by Banerjee, Shaw and Hanratty, and Deissler (refer to Table 3-1) are also plotted for comparison. The agreement with the Leveque solution is expected. The sharp transition to the solution of Metzner and Friend is unexpected. The transition of the average mass transfer coefficient to its fully developed value should occur at $L^+ = 10{,}000$. The transition of the local mass transfer coefficient occurs at $L^+ = 1{,}000$. In addition, when it does become fully developed, the average mass transfer coefficient should correspond to Shaw and Hanratty and not Metzner and Friend. These results could be attributed to the rough wall indicated by the pressure drop measurements.

The mass transfer coefficients for the 6.4, 3.2 and 1.6 mm electrodes are plotted versus the Reynolds number in Figures 5-3, 5-4 and 5-5. The mass transfer coefficient is

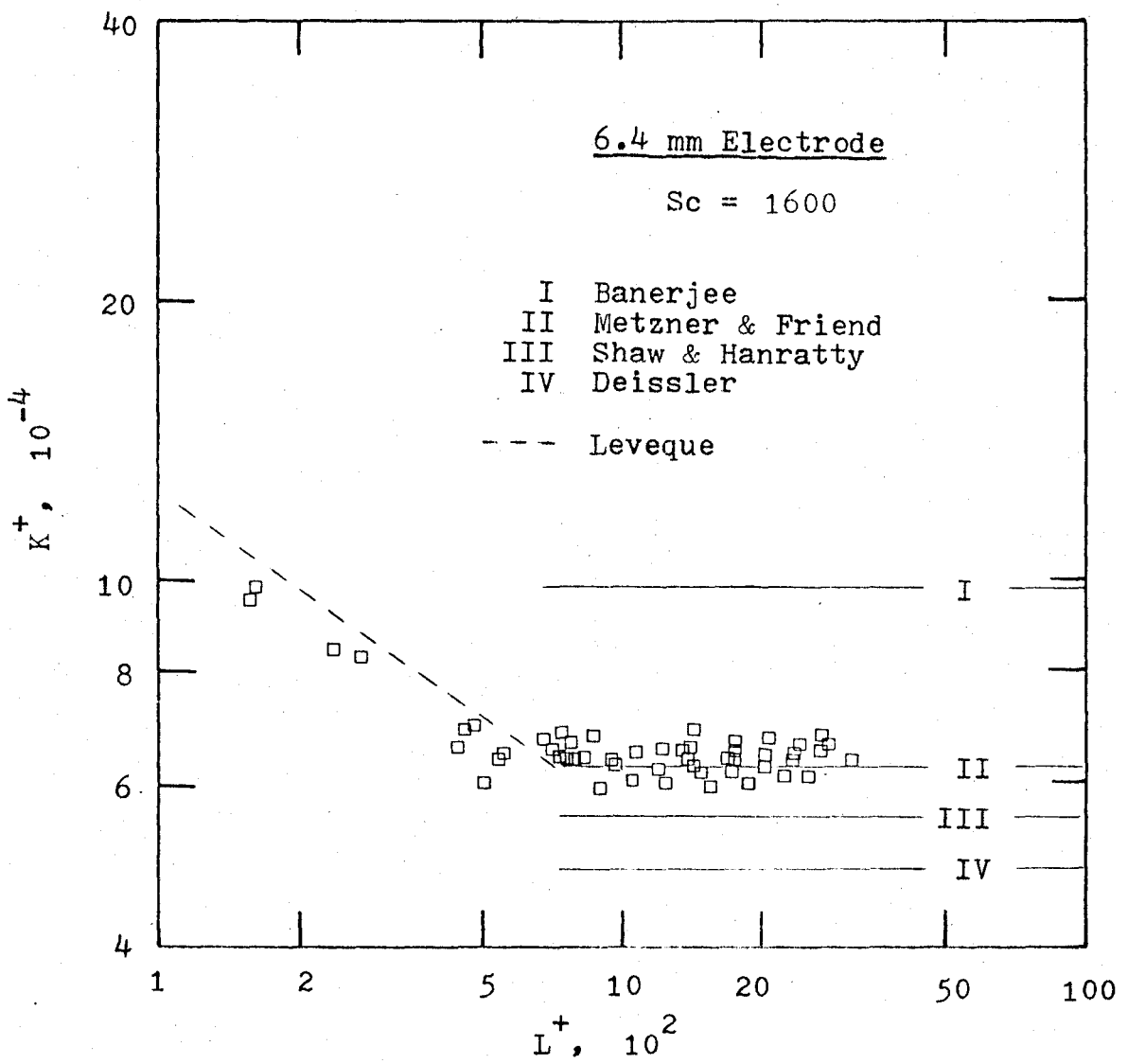

Fig 5-2. Dimensionless plot of single-phase mass transfer coefficients for 6.4 mm electrode.

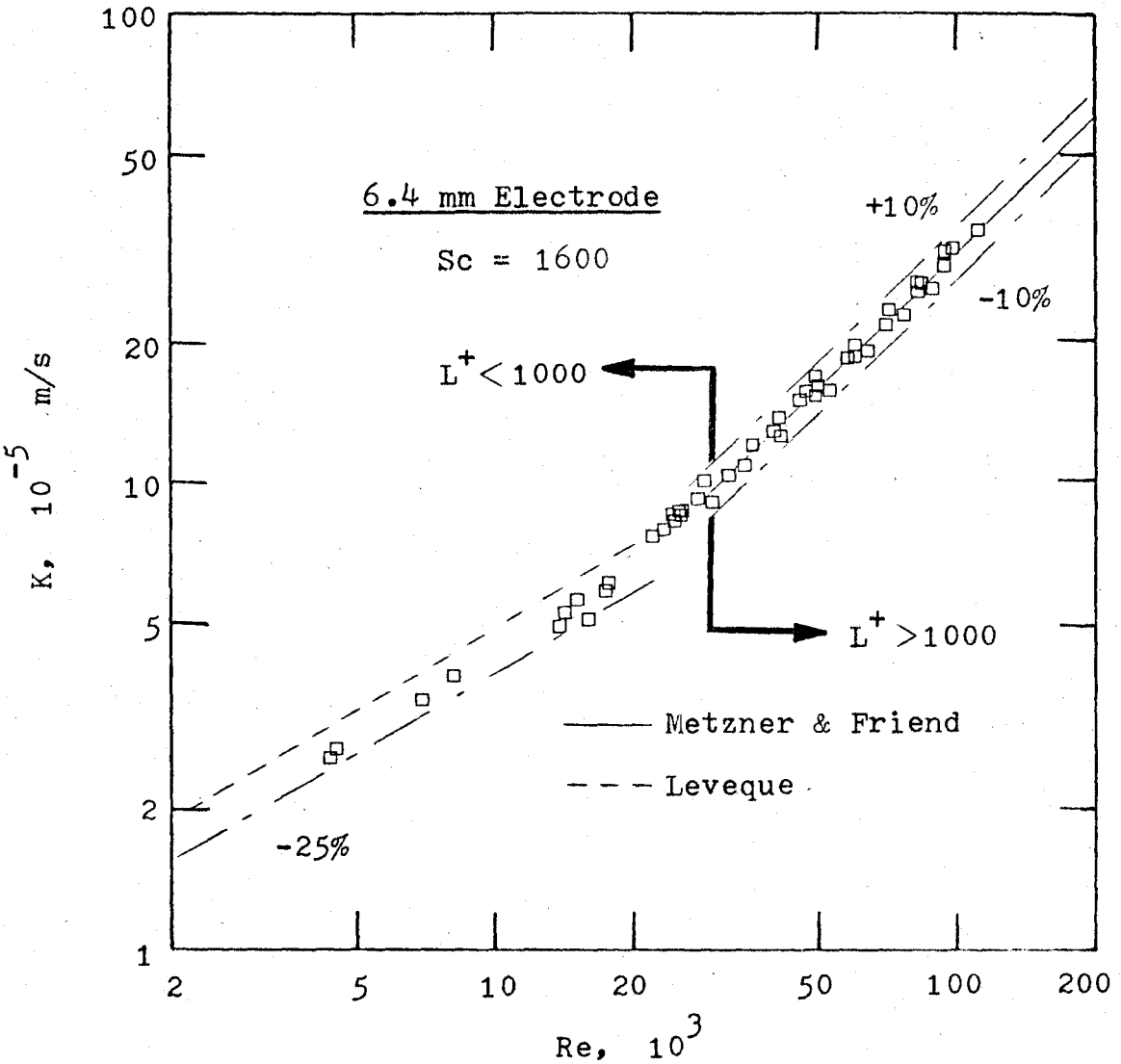

Fig. 5-3. Single-phase mass transfer coefficient versus Reynolds number for 6.4 mm electrode.

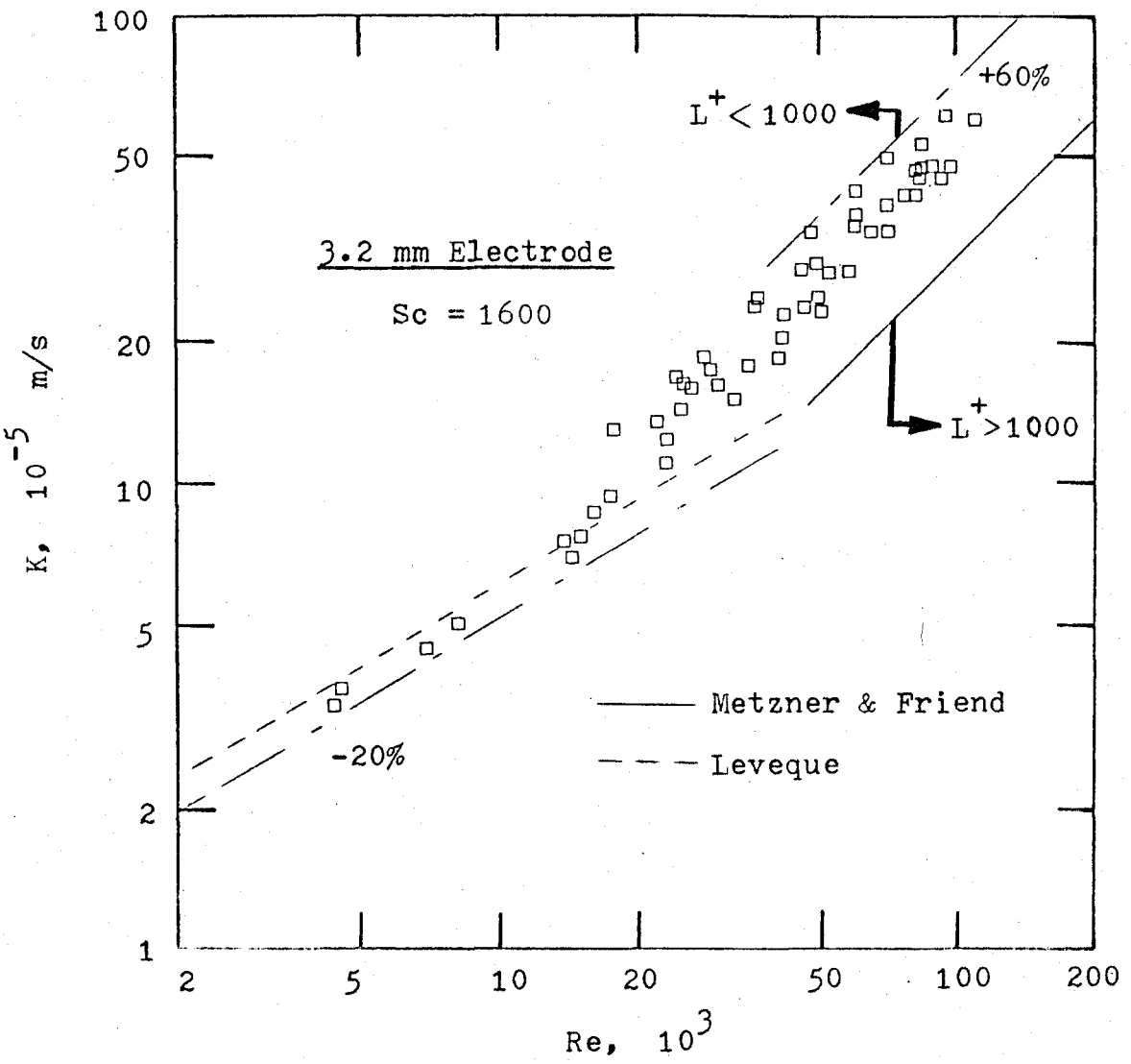

Fig 5-4. Single-phase mass transfer coefficient versus Reynolds number for 3.2 mm electrode.

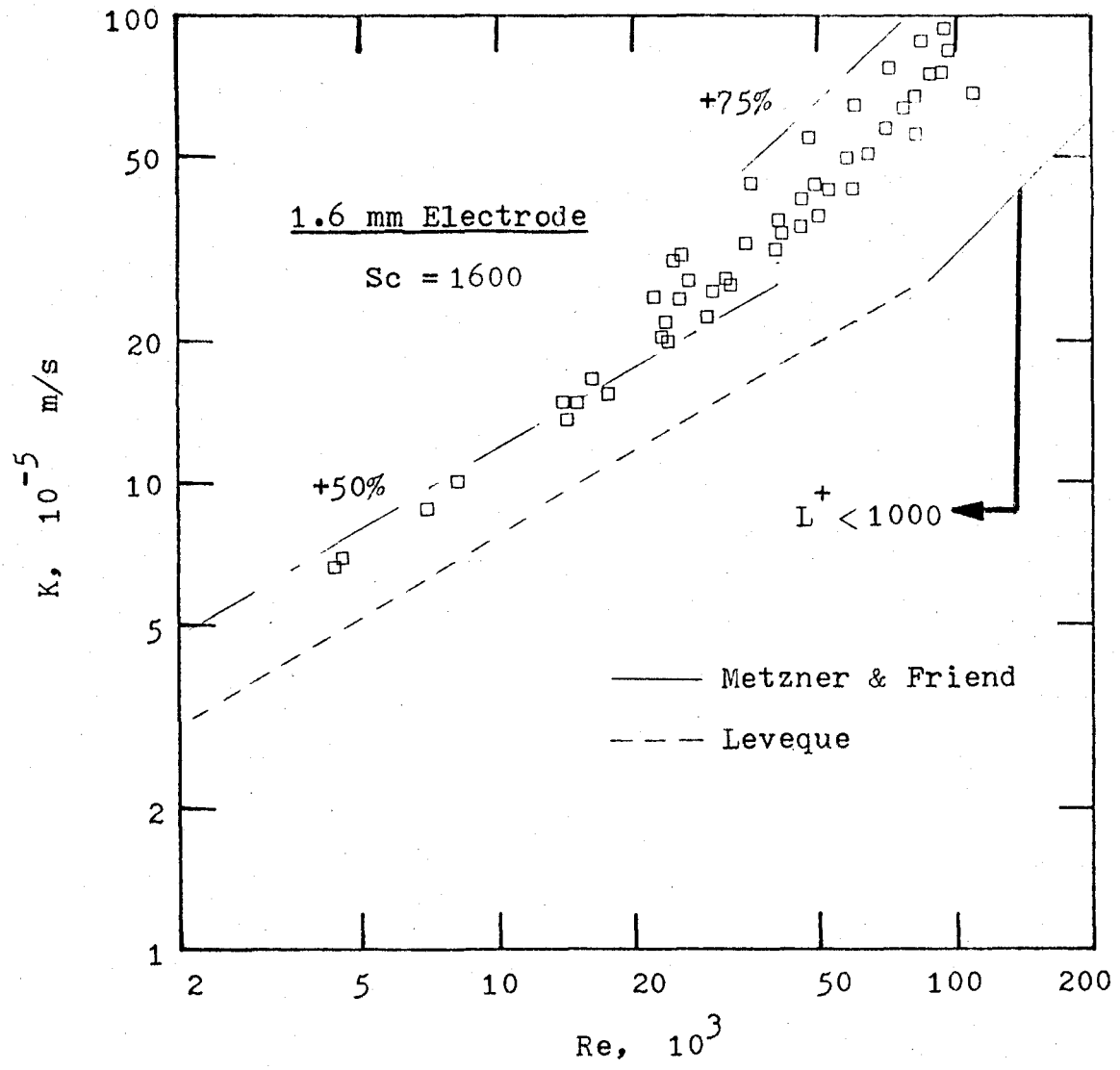

Fig 5-5. Single-phase mass transfer coefficient versus Reynolds number for 1.6 mm electrode.

seen to increase relative to the analytical solutions with decreasing electrode size. This corresponds to increased roughness sensitivity with decreasing electrode size. The average thickness of the concentration boundary layer, as predicted by equation (3.24), is 'pierced' by the wall roughness at Reynolds numbers of 8,000, 6,000 and 4,000 for the 6.4, 3.2 and 1.6 mm electrodes, respectively.

The necessity of cleaning the electrodes is shown in Figure 5-6. In experiment SPR-3, no acid wash was used. In experiment SPR-1, there was no cleaning of the electrodes whatsoever. SPR-5, which used the standard cleaning method, is shown for comparison. Increased electrode contamination reduces the mass transfer coefficient. This effect was borne out in all single- and two-phase experiments. Sutey (2) reported that in some instances electrode contamination resulted in higher mass transfer coefficients. Why this would occur was not explained.

The time-dependent nature of electrode contamination is shown in Figure 5-7. At the beginning of experiment SPR-9, the measurements for SPR-9a were taken. Two hours later the measurements for SPR-9b were taken. The measurements for SPR-9c were taken four hours after the start of the experiment. Comparing SPR-9a and SPR-9b, the drift at the highest Reynolds number was 8%. Comparing SPR-9a and SPR-9c, the drift increased to 16%. The drift decreases with decreasing Reynolds number.

Experiment SPR-8 demonstrated that failing to de-

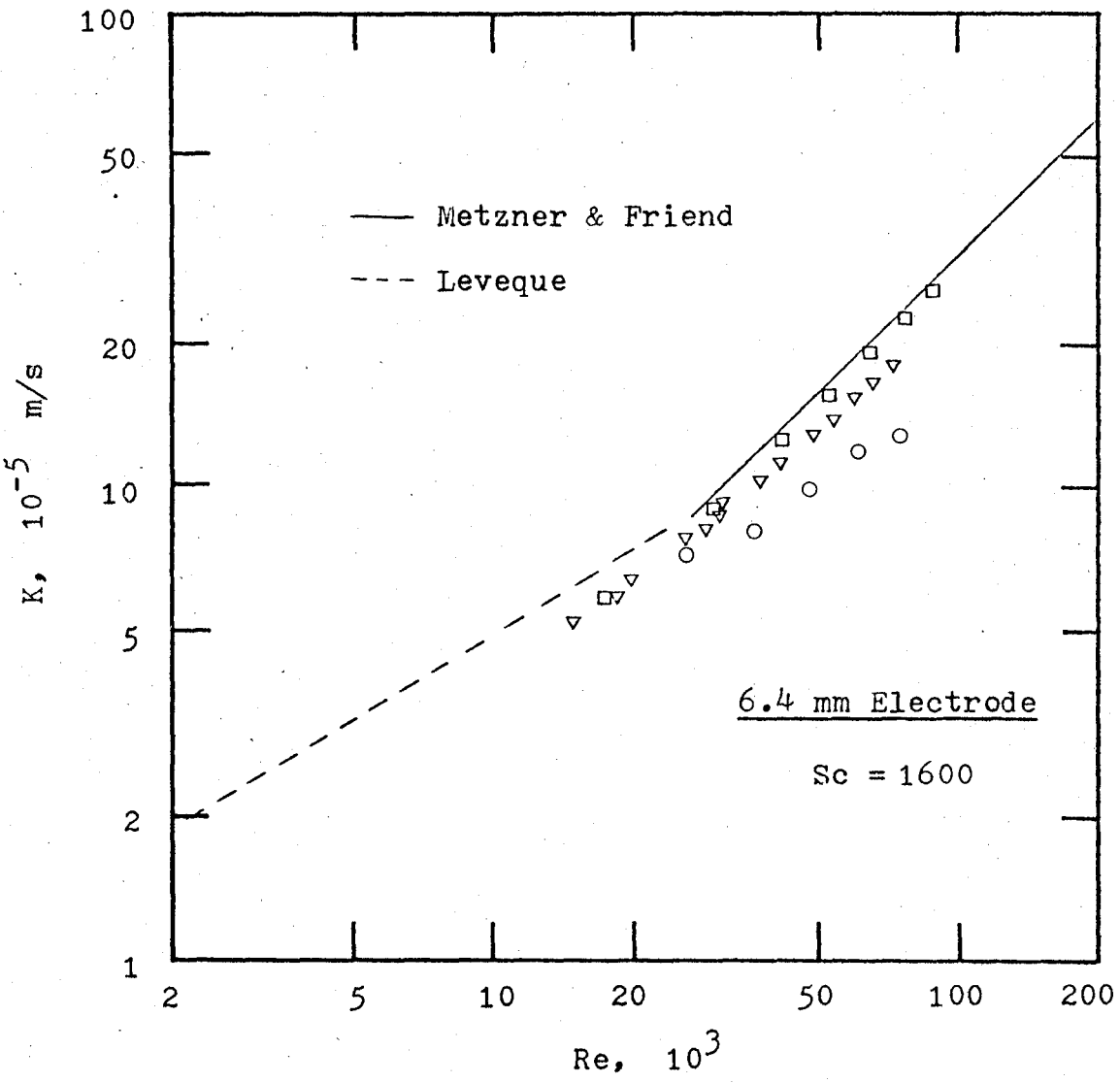

Fig. 5-6. Single-phase mass transfer coefficients for 6.4 mm electrode showing effect of cleaning the electrode prior to the experiment. □ , standard cleaning method; ▽ , standard cleaning method with no acid wash; ○ , no cleaning applied.

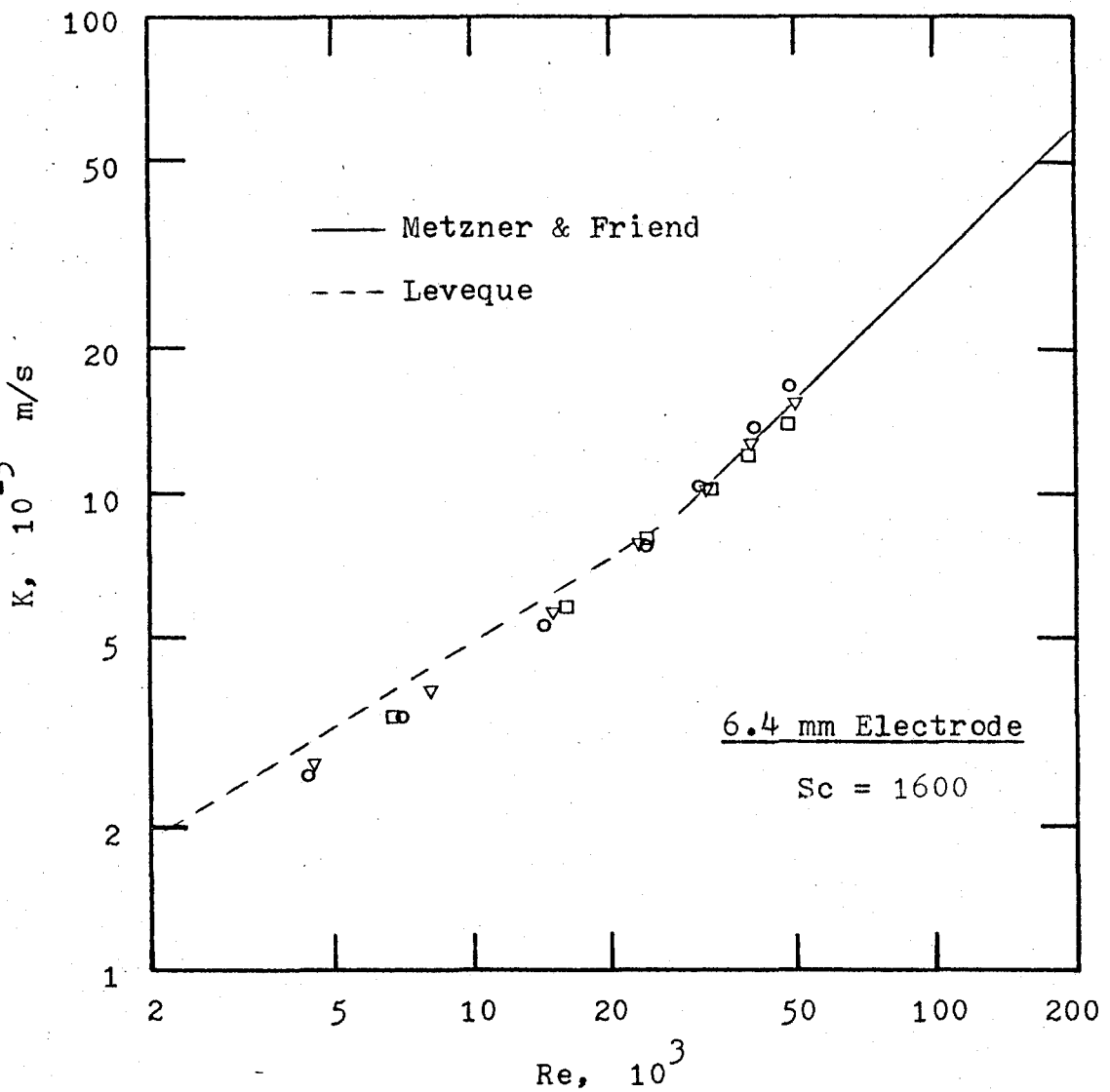

Fig. 5-7. Single-phase mass transfer coefficients for 6.4 mm electrode showing time-dependent nature of electrode contamination. Time elapsed since beginning of experiment: ○ , 1 hour,; ▽ , 2 hours; □ , 4 hours.

aerate the water accelerated the contamination process. The results of experiment SPR-10 indicated that the mass transfer coefficient was inversely proportional to the Schmidt number to the 2/3 power ($K \propto (Sc)^{-2/3}$), agreeing with the majority of expressions in Table 3-1 for fully developed mass transfer.

CHAPTER 6

RESULTS AND DISCUSSION FOR TWO-PHASE EXPERIMENTS

Ten two-phase experiments identified as TPR-1 to TPR-10 were performed. The pressure drops and electrochemical cell currents were not time-averaged in the first four experiments. The measurements for these initial experiments were not considered **reliable** and the results of TPR-1 to TPR-4 are not reported. Experiments TPR-5, -6 and -7 were replicate runs, using 1.0 M sodium hydroxide, employing five levels of electrolyte flow rate and five levels of nitrogen flow rate. TPR-8 was aborted due to cracking of the liquid rotameter. The last two experiments, TPR-9 and TPR-10, used 1.75 and 3.00 M sodium hydroxide, respectively. At each level of liquid flow rate, single-phase mass transfer measurements were made. These are referred to as single-phase benchmark mass transfer coefficients.

To correct the wall roughness that overly influenced the results of the single-phase experiments, the test section was reamed and honed from its original diameter of 12.7 mm to 13.5 mm. A mandrel was made up to provide better alignment of the electrodes upon reassembly. After these modifications, profilometer measurements gave a relative surface roughness of less than 0.0002. This is the equivalent of a smooth tube for Reynolds numbers less than 100,000.

The experiment identification numbers are quoted in order that one may refer to the original data in Appendix 9.

6.1 Flow Regimes

The observed flow regimes were slug, churn and annular. The characteristics and behaviour matched those given in Chapter 2. The observed regimes were identified using visual observations and photographs. Typical photographs of the regimes as they appeared in the test section are given in Figure 6-1. These were obtained with a standard 35mm camera and flash unit. The similarity with Figure 2-1 is self-evident.

In Figure 6-2 the flow regime map of Dukler and Taitel is seen to be in good agreement with the observed flow regimes. The churn-annular transition has been modified. The critical Weber number and drag coefficient in equation (2.8) were, respectively, taken to be 10 and 0.8, as opposed to the recommended values of 30 and 0.44. Making this modification causes the churn-annular transition at low liquid flow rates to match the empirical prediction of Wallis, equation (2.9) with the constant C set equal to 0.9 corresponding to a smooth system geometry. This modification gave better agreement with the observed regimes.

The churn flow regime was further subdivided into churn (flow reversal) and churn (flooding). As the gas flow rate is decreased from an annular regime, a point is reached where the annular film becomes unstable and some of the liquid

Slug Churn Annular

Fig. 6-1. Photographs of observed flow regimes

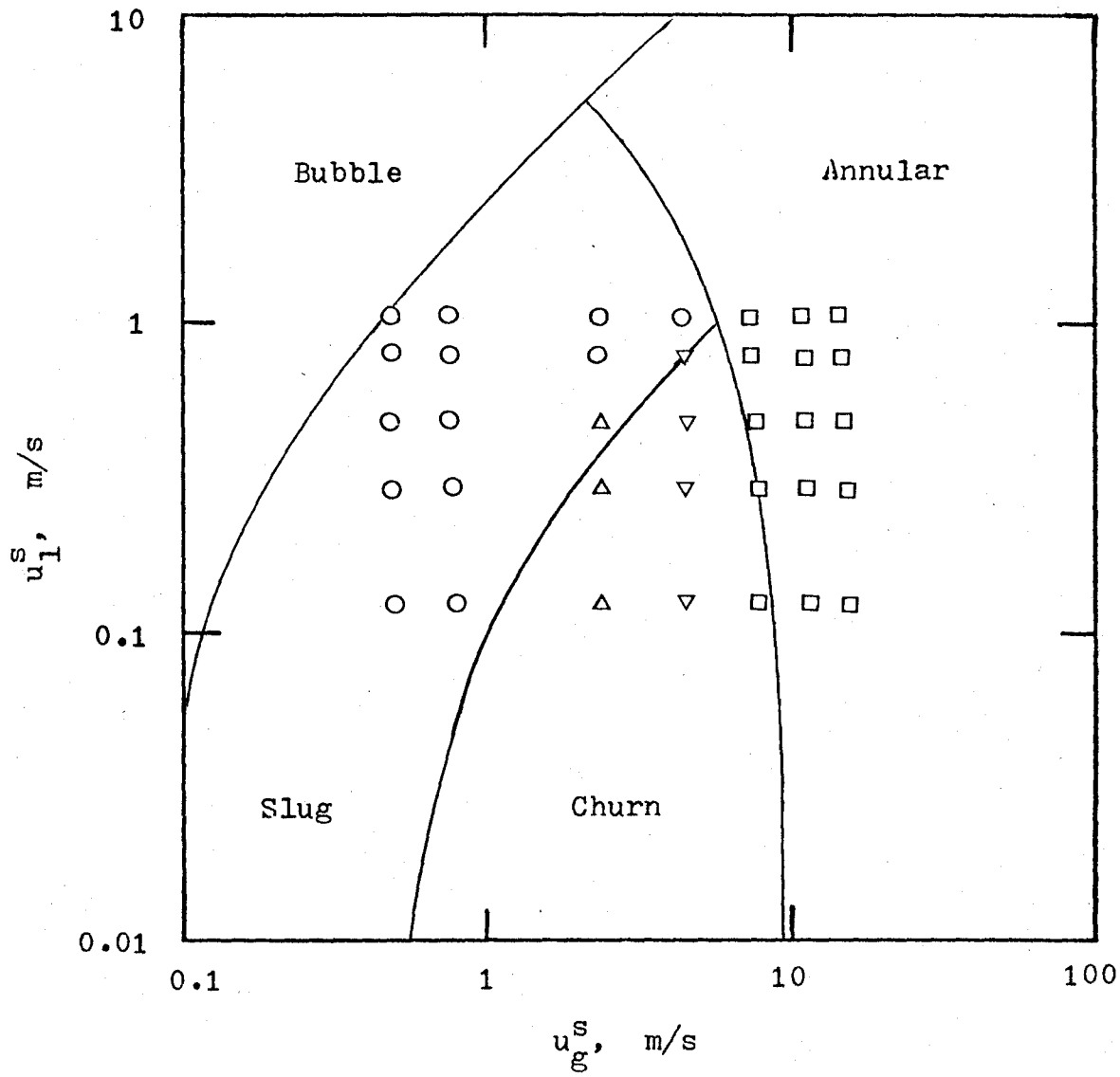

Fig. 6-2. Comparison of observed flow regimes with the modified flow regime map of Dukler and Taitel. The observed regimes are: ○ , slug; △ , churn (flow reversal); ▽ , churn (flooding); □ , annular.

breaks from the wall and falls downwards. The liquid is seen to move upwards and downwards at the same time. This behaviour is identified as churn (flooding). As the flow rate is further decreased, complete flow reversals, in which all of the liquid is seen to fall downwards simultaneously, takes place. This is identified as churn (flow reversal). These distinctions were found to be significant when it came to explaining the two-phase mass transfer data.

6.2 Void Fractions and Pressure Drops

The measured void fraction was successfully correlated using Griffith and Wallis (equation (2.14), C = 1.45) for the slug and churn (flow reversal) regimes. Lockhart and Martinelli (equations (2.17), (2.18) and (2.24)) as modified by Davis (equation (2.19)) was used for the churn (flooding) and annular regimes. Figure 6-3 shows that the accuracy is ±10%. If Lockhart and Martinelli is used without modification, the void fraction is underpredicted because the original correlation ignores the effect of entrainment. Davis' modification compensates for this, though it must be noted that it was formulated to correct the pressure drop and not the void fraction.

The measured pressure drops across the test section are illustrated in Figure 6-4. For all but the highest level of liquid flow rate, the total pressure drop initially drops to a minimum before increasing in the expected fashion, as the gas flow rate is increased from zero. At the highest

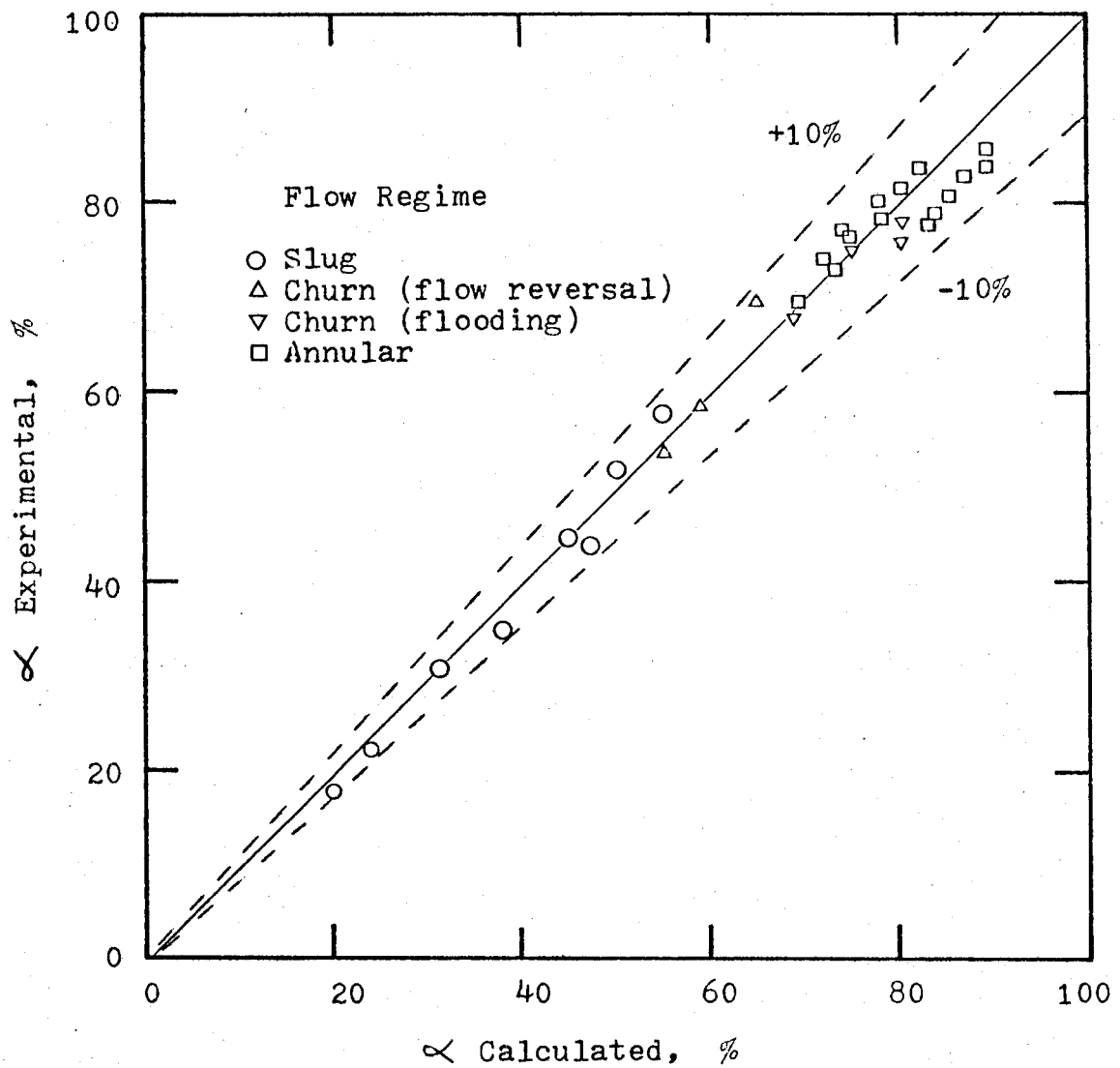

Fig. 6-3. Experimental versus calculated void fraction.

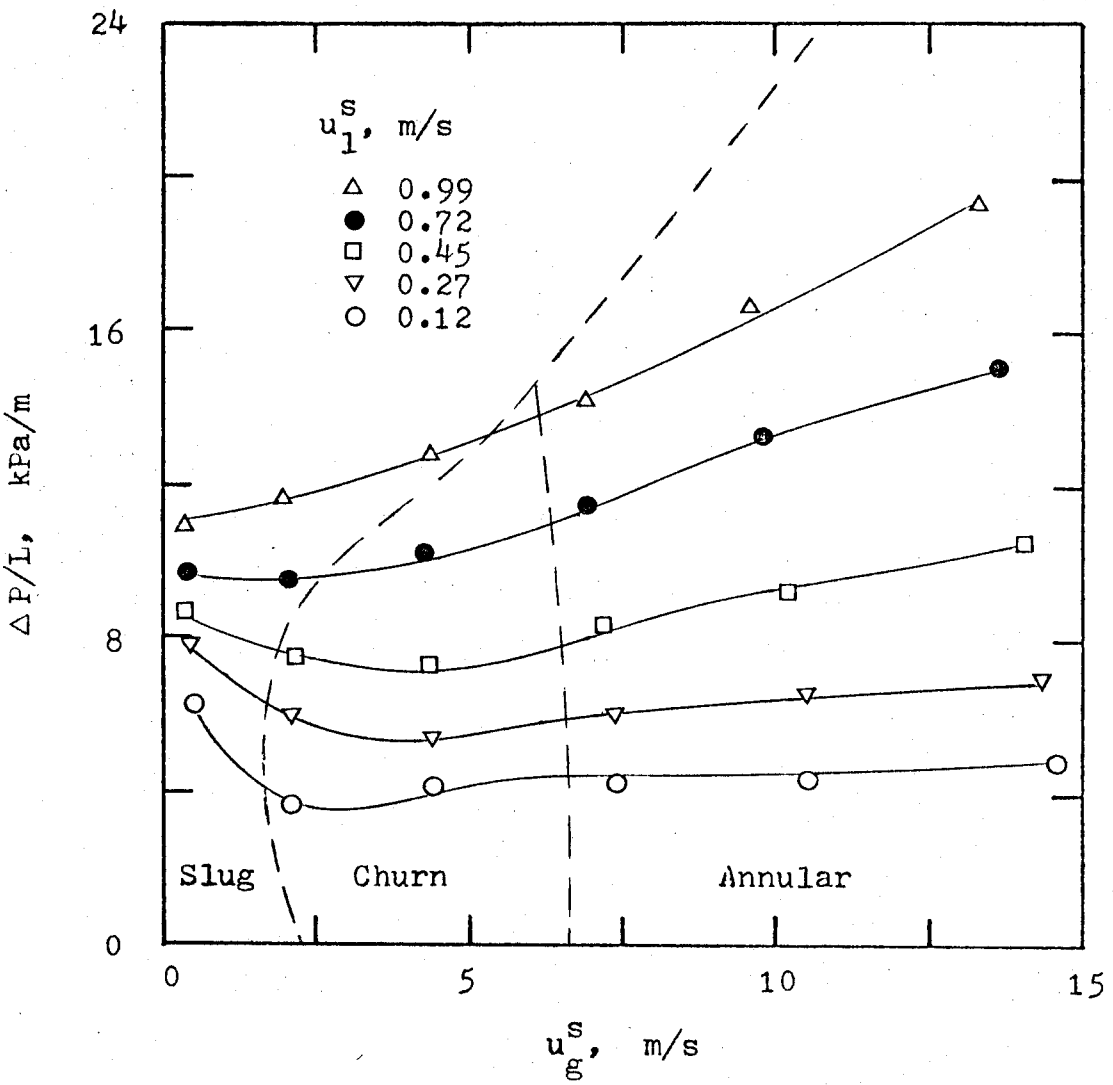

Fig. 6-4. Total pressure drop versus superficial gas velocity, with flow regimes delineated.

level of liquid flow rate, where the churn regime does not exist, the pressure drop does not exhibit a decrease. At the lower levels of liquid flow rate, the pressure drop is relatively constant after passing through the minimum.

This behaviour in the total pressure drop has been documented by other investigators (5, p. 332) and is known to be keyed to the flow regime. The minumum is seen to occur in the churn flow regime. Figure 6-5 shows that the frictional pressure drops exhibit no anomalous behaviour, showing a steady increase with increasing gas flow rate at constant liquid flow rate. This indicates that it is the gravitational pressure drop and thus the variation in the void fraction from one regime to another that is the underlying cause of the behaviour of the total pressure drop. Examination of Figure 6-3 shows that the void fraction increases rapidly in the transition from slug to churn, and then reaches a roughly constant value of 80% as the annular regime is approached.

The frictional pressure drop was successfully correlated using Griffith and Wallis (equation (2.10)) for the slug and churn (flow reversal) regimes. As for the void fraction, Lockhart and Martinelli (equation (2.15)) as modified by Davis was used for the churn (flooding) and annular regimes. Figure 6-6 shows that the accuracy is $\pm$ 15%.

With the churn flow regime acting as a transition regime between slug and annular flow, the application of a slug correlation to churn (flow reversal) and an annular

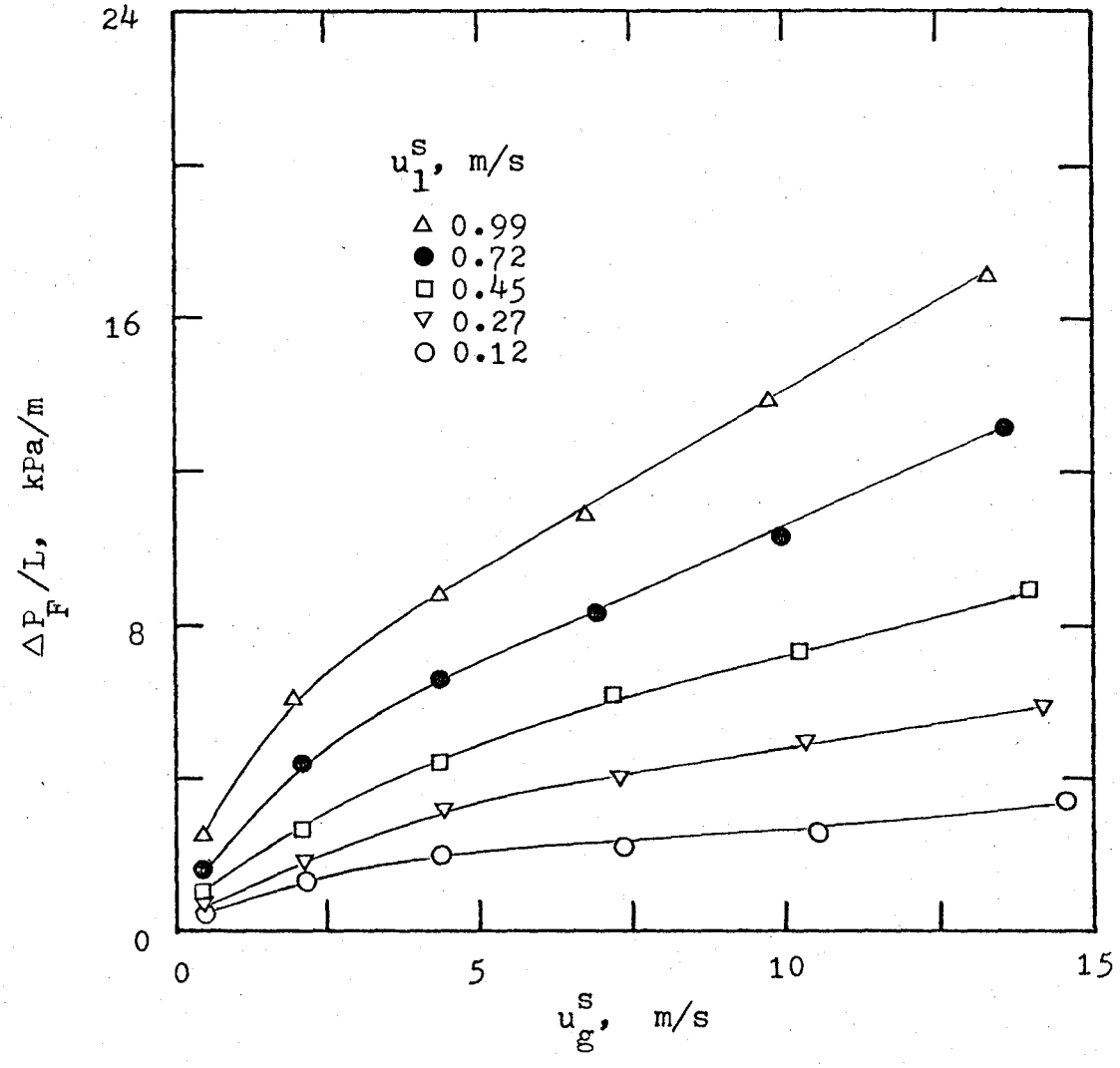

Fig. 6-5. Frictional pressure drop versus superficial gas velocity.

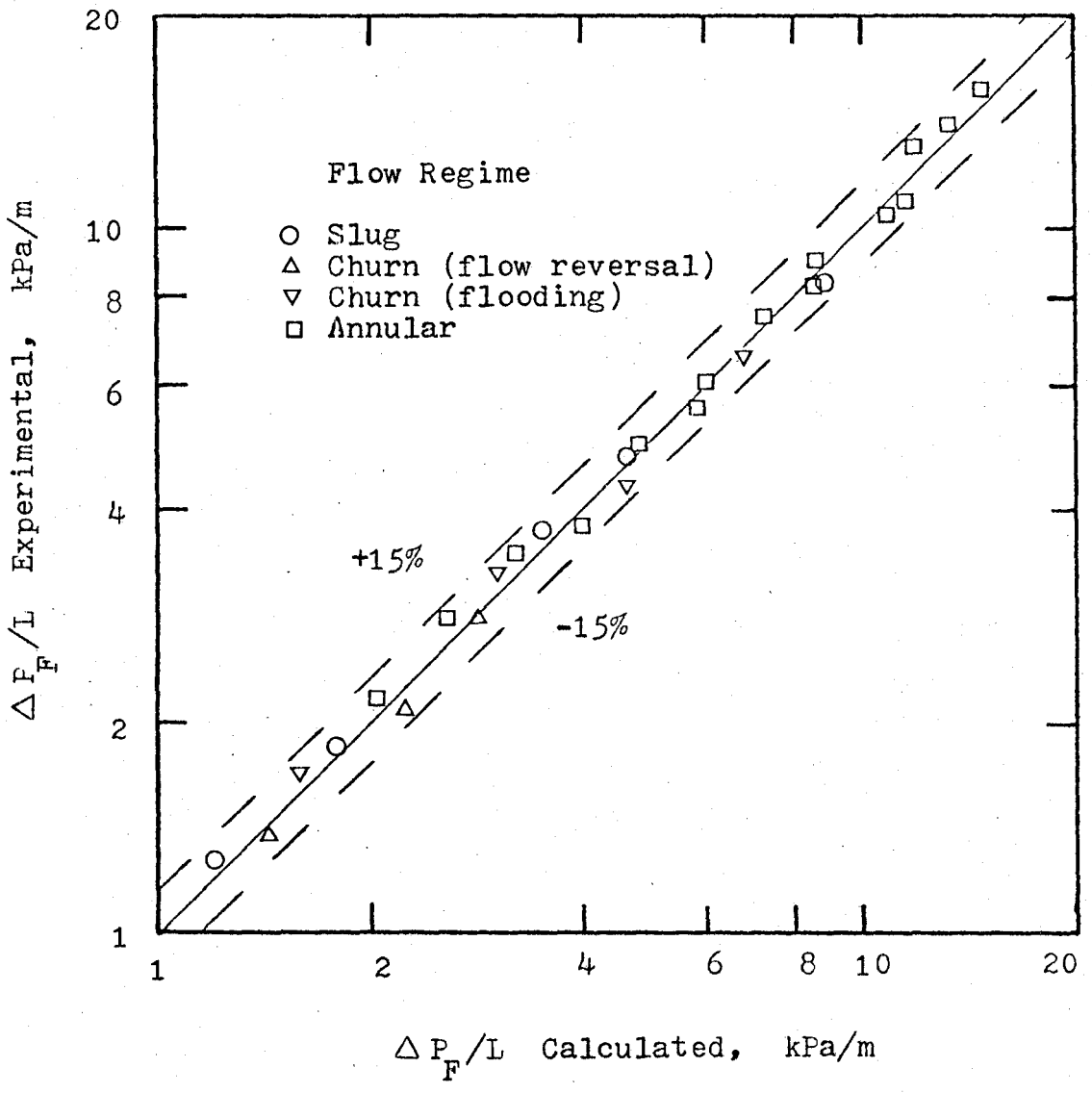

Fig. 6-6. Experimental versus calculated frictional pressure drop in two-phase flow.

correlation to churn (flooding) was thought to be the most logical approach. It also turned out to provide the best correlation between the calculated and measured void fractions and frictional pressure drops. The accuracy obtained in the slug and annular regimes alone equals that obtained by other investigators, as reported in Sections 2.3 and 2.4.

6.3 Mass Transfer Coefficients

Two-phase mass transfer coefficients were measured for the 3.2 and 6.4 mm ring electrodes. The results from experiments TPR-5, -6, -7 and -8 are plotted in Figures 6-7 and 6-8. The spread of the data indicates a reproducibility of 5%. This can be attributed to electrode contamination. The upper limit of a set of replicate data was used in all the calculations.

Comparing Figure 6-7 and 6-5, the mass transfer coefficients are seen to exhibit the same behaviour as the frictional pressure drop except for an inflection in the former at superficial gas velocities between 2 and 5 m/s and superficial liquid velocities less than 0.7 m/s. This region corresponds to the churn flow regime. The flow reversals contribute to a form of gross turbulence and this could account for the enhancement in mass transfer.

The single-phase benchmark mass transfer coefficients for the two-phase experiments are given in Figure 6-9. The agreement with the Leveque solution for all three electrodes and all three Schmidt numbers is good. This would indicate

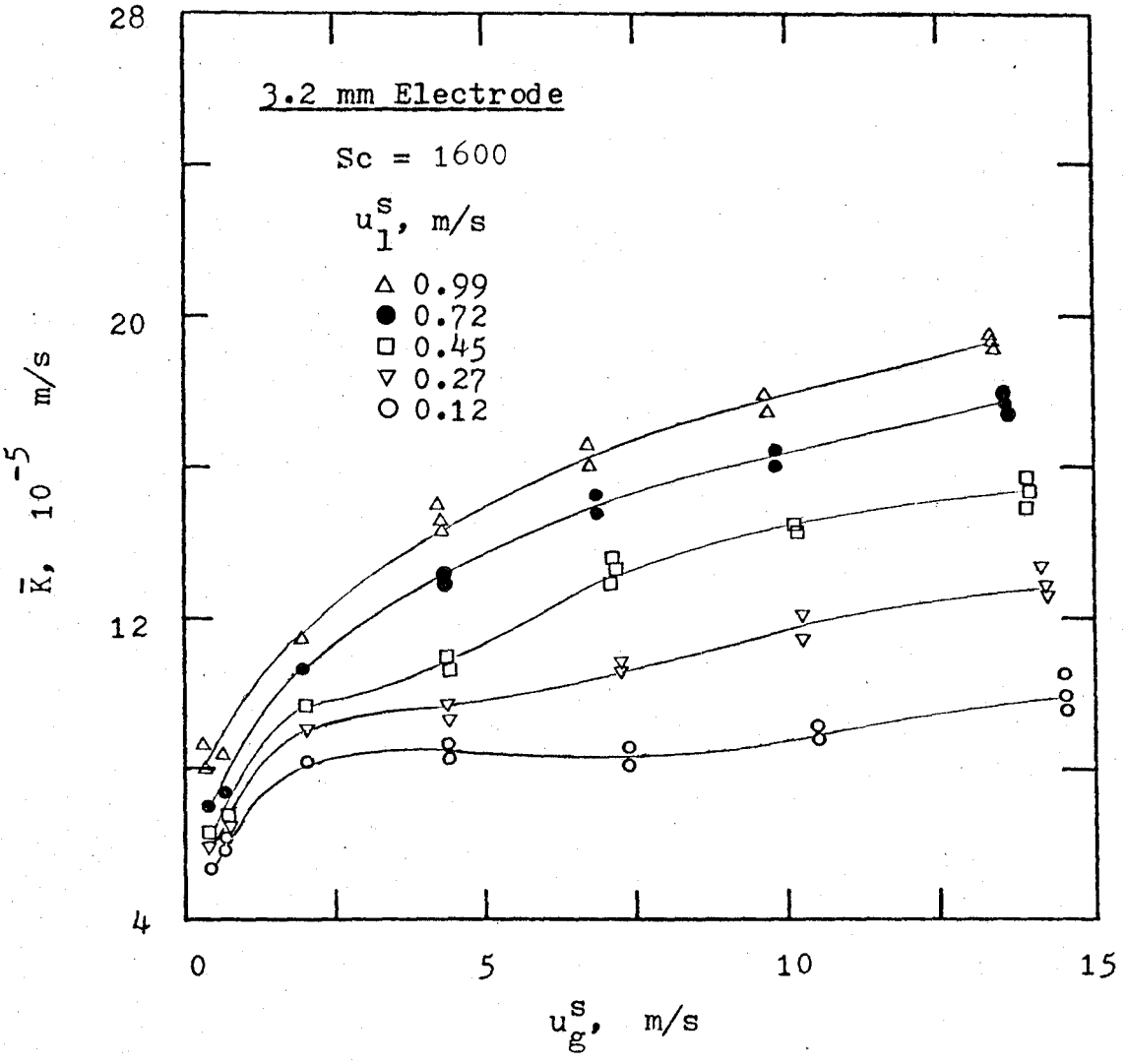

Fig. 6-7. Two-phase mass transfer coefficient versus superficial gas velocity for 3.2 mm electrode.

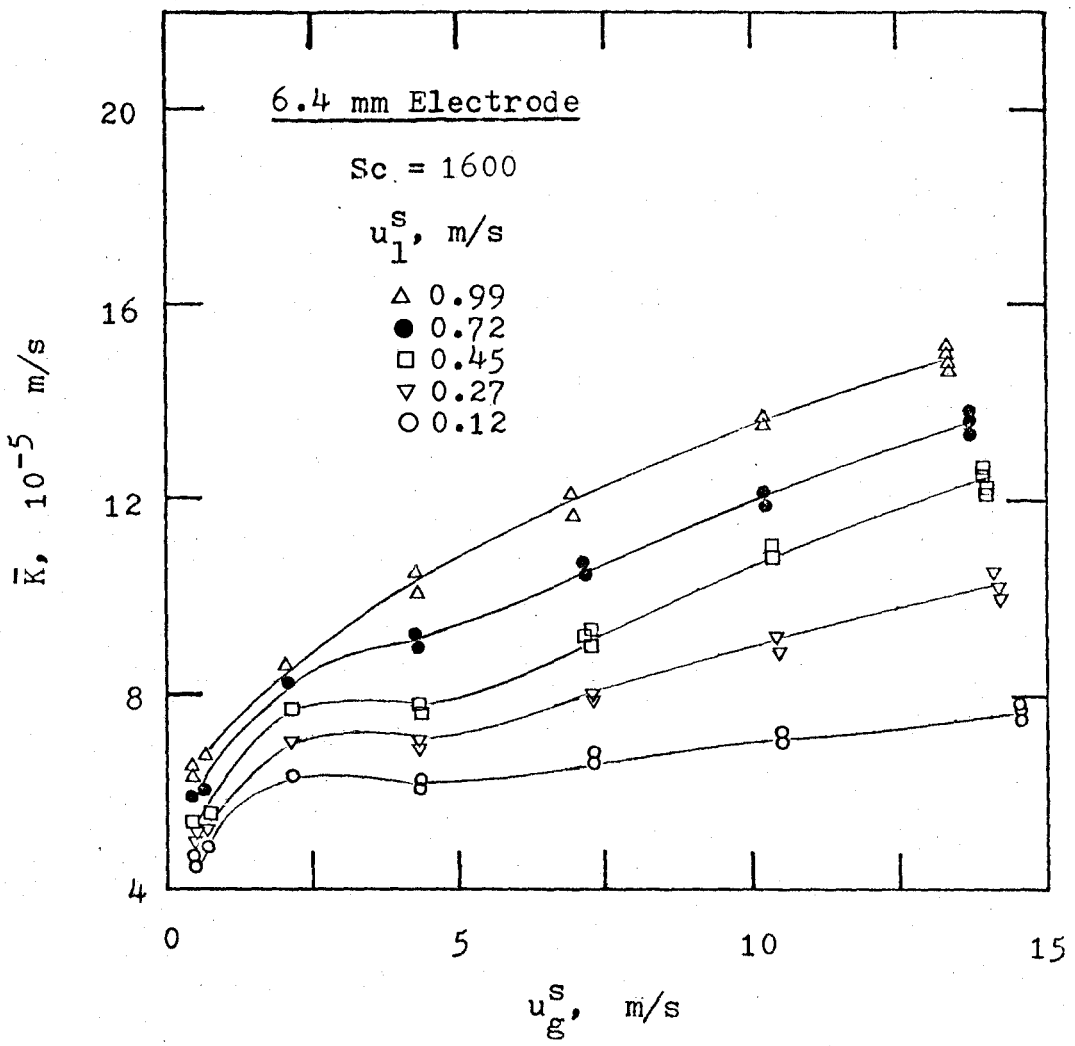

Fig. 6-8. Two-phase mass transfer coefficient versus superficial gas velocity for 6.4 mm electrode.

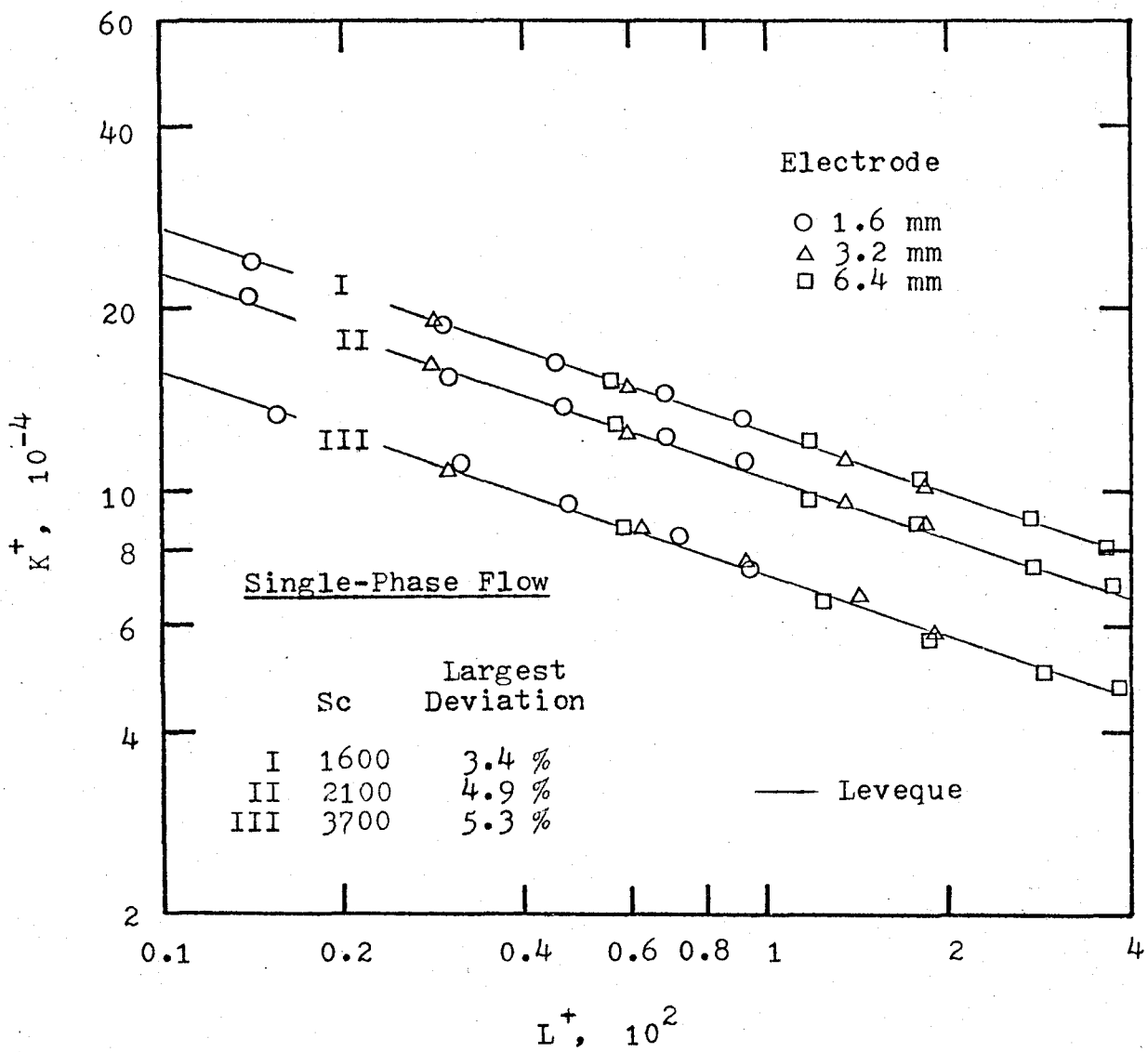

Fig. 6-9. Single-phase benchmark mass transfer coefficients for two-phase experiments.

that the deficiency in the wall roughness had been removed and the two-phase mass transfer coefficients could be considered reliable. It should be noted that the pressure drops for these benchmark coefficients were calculated using the Blasius equation and not actually measured. For the range of liquid flow rates used in the two-phase experiments, the single-phase frictional pressure drops were less than 5% of the total pressure drops, overlapping the 5% accuracy of the measurements. This problem does not exist for the two-phase frictional pressure drops because of the higher total, and lower gravitational, pressure drops involved.

Using the results of the replicate runs , the dimensionless two-phase mass transfer coefficients are plotted in Figures 6-10, 6-11 and 6-12 for the slug, churn and annular regimes, respectively. The mass transfer coefficients are all within 8% of the Leveque solution. The value of K_{∞}^{+} predicted by Shaw and Hanratty is shown for comparison. Except for the churn regime, the mass transfer coefficients are all on the high side of Leveque. This could be attributed to increased turbulence. However this cannot be considered too significant as the accuracy of the data points is $\pm$ 5% and, if the average instead of the highest recorded mass transfer coefficients from the replicate runs had been used, the results would have been lowered by 3%. No significant mass transfer enhancement was experienced in the slug flow regime. This concurs with the discussion given in Section 3.3.2.

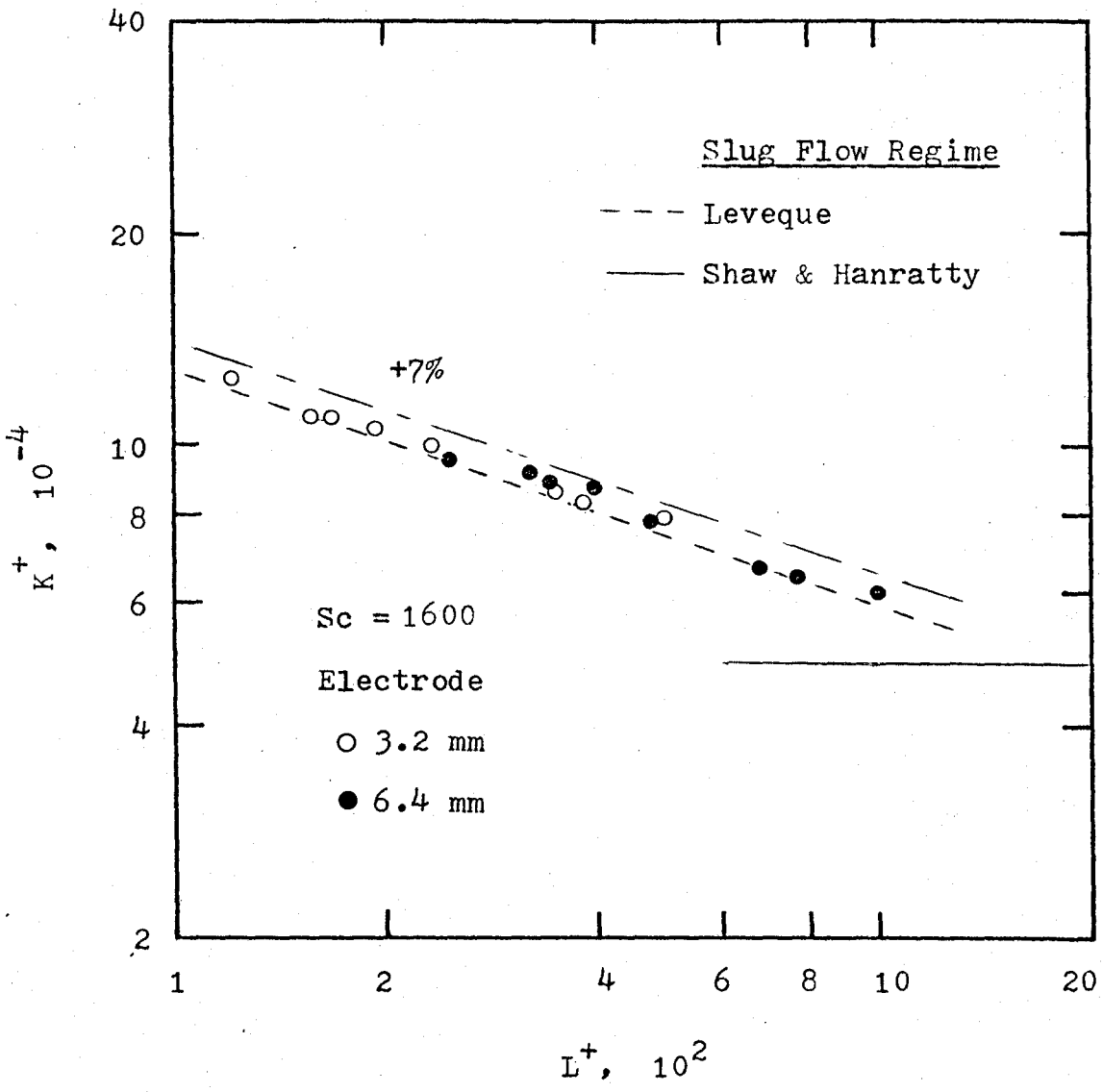

Fig. 6-10. Dimensionless plot of two-phase mass transfer coefficients for the slug flow regime.

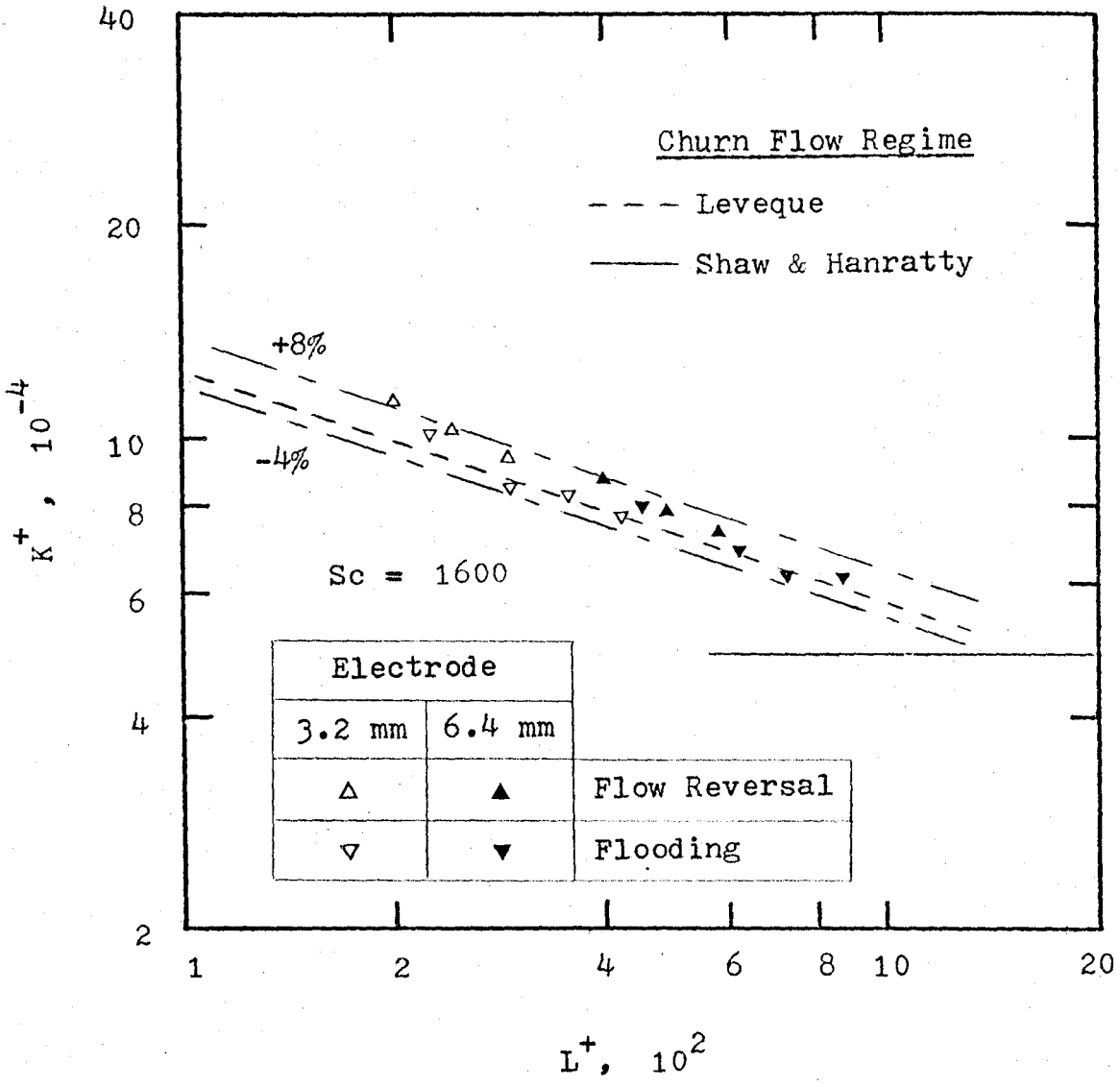

Fig 6-11. Dimensionless plot of two-phase mass transfer coefficients for the churn flow regime.

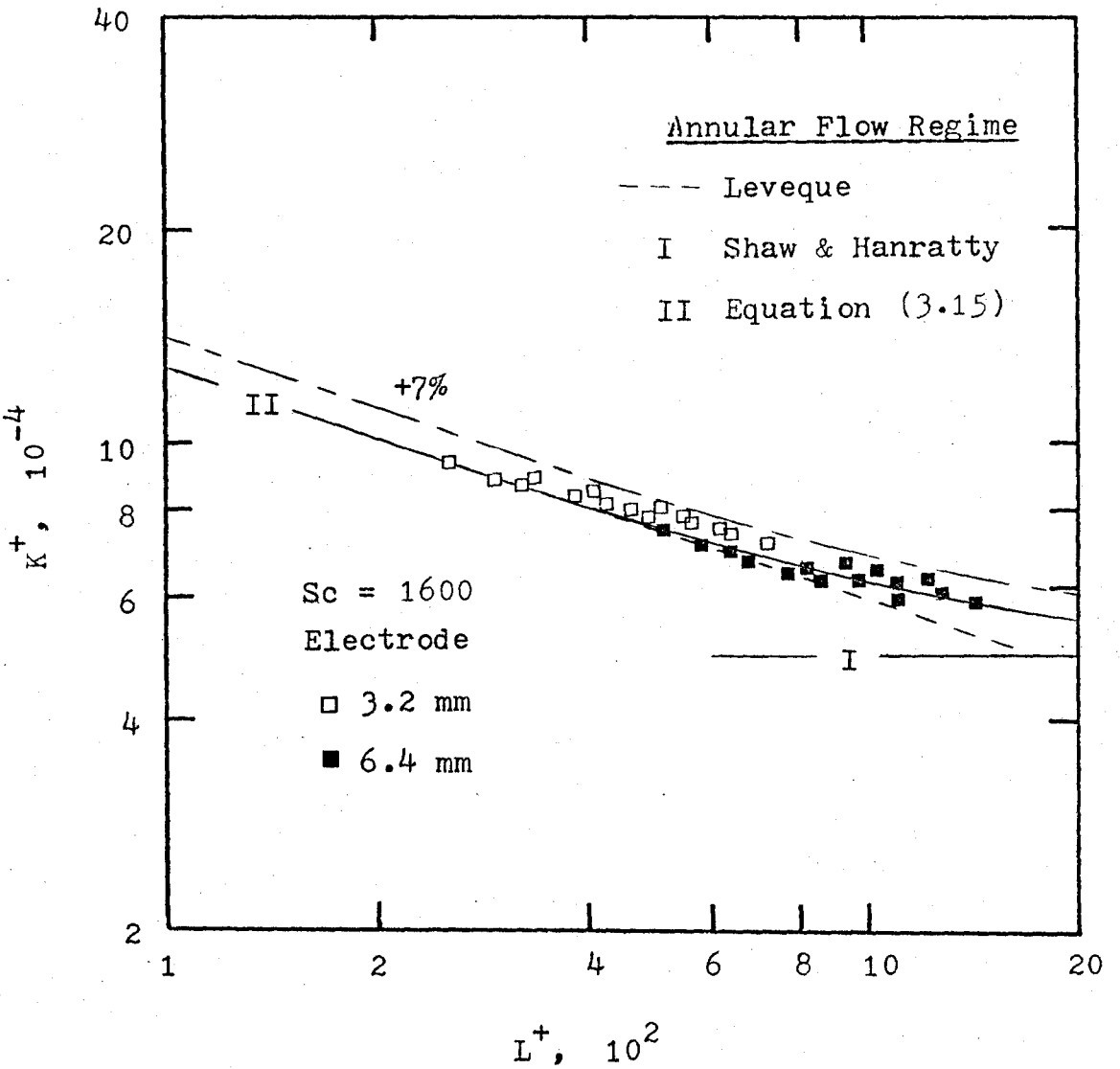

Fig 6-12. Dimensionless plot of two-phase mass transfer coefficients for the slug flow regime.

Son and Hanratty's (25) numerical solution of the governing equation for mass transfer, equation (3.15) with m = 3.4, is given with the annular results in Figure 6-12, and is seen to deviate from the Leveque solution for $L^+ > 600$.

By differencing the currents measured by the 3.2 and 6.4 mm electrodes, obtained at the same flow conditions, one can calculate the fully developed mass transfer coefficient, provided $L^+ > 1{,}000$ for the 3.2 mm electrode alone

$$K^+_\infty = (I_{\ell_{6.4}} - I_{\ell_{3.2}}) / ((a_{6.4} - a_{3.2}) F c_b) \qquad (6.1)$$

This approach has been used by Shaw and Hanratty (26). Figure 6-13 shows the results of such an exercise using the data of TPR-6, -9 and -10 to show the effect of the Schmidt number. The agreement with the expression of Shaw and Hanratty indicates that the eddy diffusivity close to the wall in two-phase flow is the same as that in single-phase flow.

6.4 Wall Shear Stress

The wall shear stresses as calculated from the measured mass transfer coefficients using equations (3.27) and (3.28), are compared with the wall shear stresses as calculated from the measured void fractions and pressure drops using equation (2.5), in Figure 6-14. The agreement is -10% to +20%. This is surprising good considering the calculated errors for equation (3.27), (3.28) and (2.5) are according to Table 4-2 $\pm$ 18%, $\pm$ 14% and $\pm$ 8%, respectively.

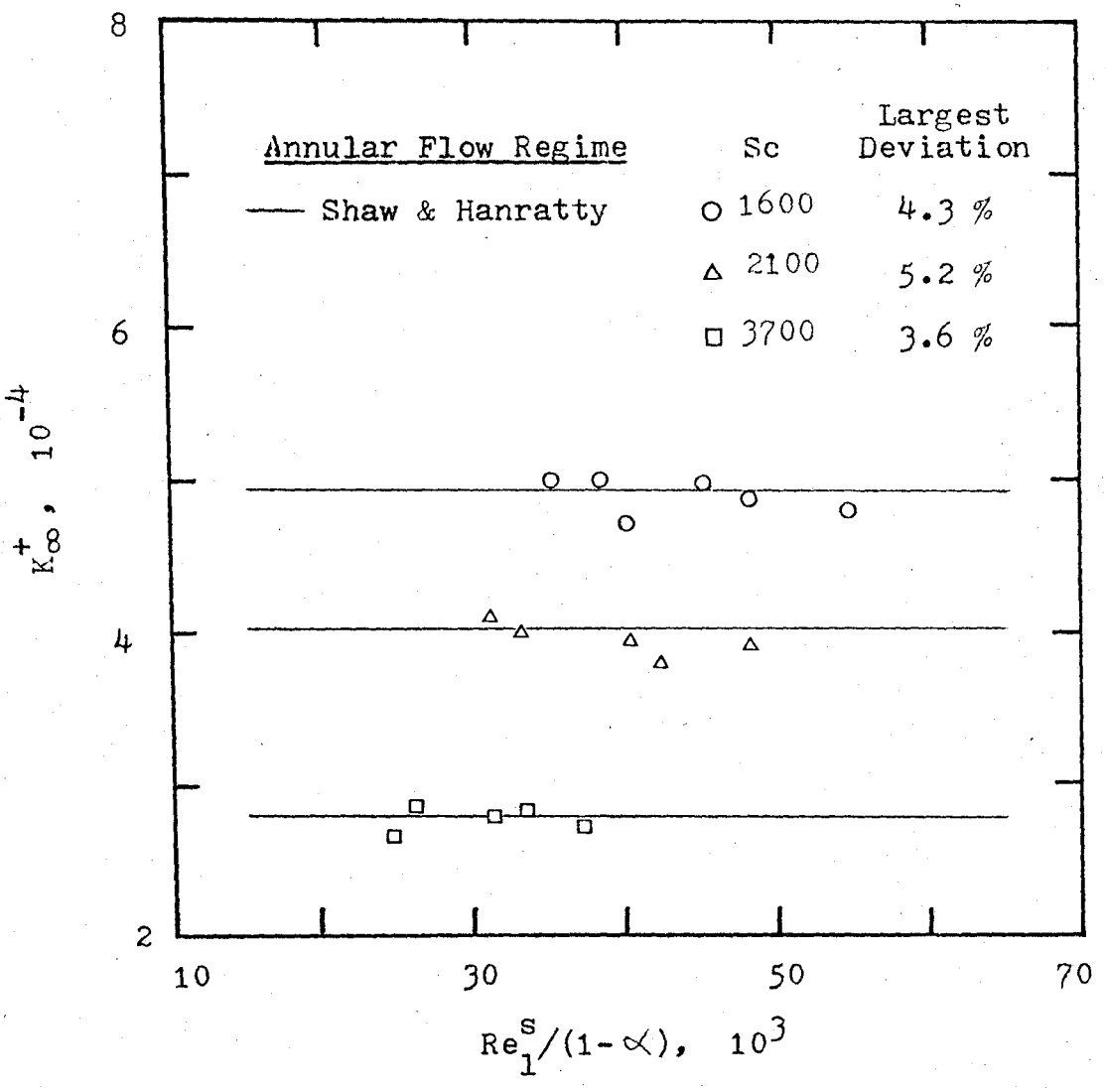

Fig 6-13. Dimensionless fully developed two-phase mass transfer coefficients, obtained by differencing the 3.2 and 6.4 mm electrodes, showing effect of Schmidt number.

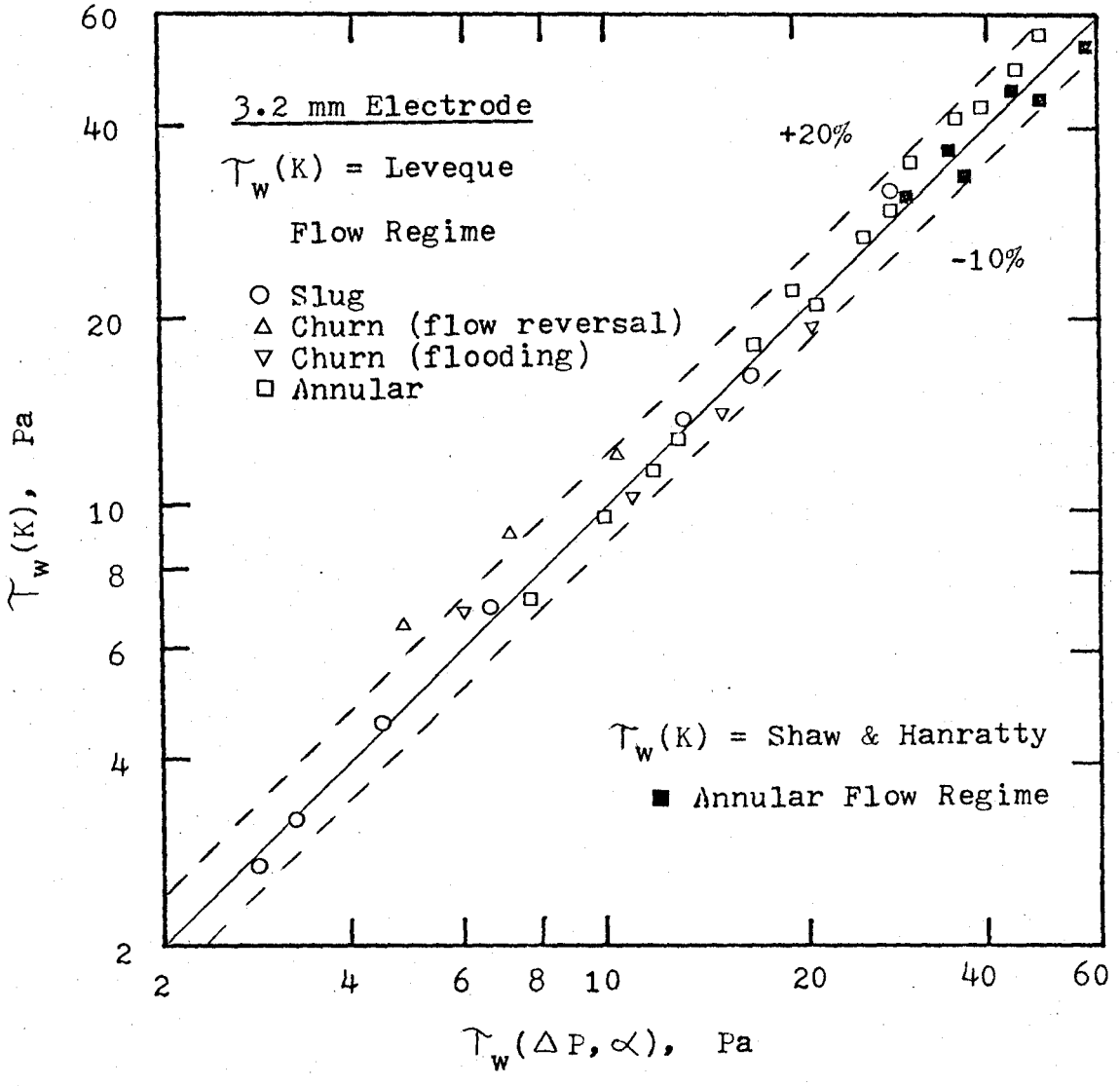

Fig 6-14. Wall shear stress, calculated from two-phase mass transfer coefficients, versus wall shear stress, calculated from measured pressure drops and void fractions.

The significance of dividing the churn flow regime into churn (flow reversal) and churn (flooding) shows up in Figure 6-14. In churn (flow reversal) the shear stress goes negative upon flow reversal, but there is no analogous way that the mass transfer coefficient can go negative. The end result is the mass transfer coefficient predicting wall shear stresses that are over 20% too high. Whereas in the churn (flooding) regime, the mass transfer coefficient predictions of the shear stresses are 10% too low. The rate of mass transfer is observed to remain the same (see Figure 6-7) but complete flow reversals are no longer taking place leading to a higher wall shear stress in churn (flooding) than in churn (flow reversal).

6.5 Interfacial Shear Terms

The interfacial shear terms, calculated from the measured pressures and void fractions using equation (2.4) are plotted in Figure 6-15. The interfacial shear terms, calculated using the pressure drops and void fractions according to Griffith and Wallis, and Lockhart and Martinelli as modified by Davis, are seen to be in good agreement. This is simply a reflection of the accuracy of the correlations as given in Figures 6-3 and 6-6. Little else can be done with the terms without the interfacial area.

The interfacial area can be determined experimentally by measuring the absorption of carbon dioxide in aqueous sodium hydroxide. The reaction is fast enough that the

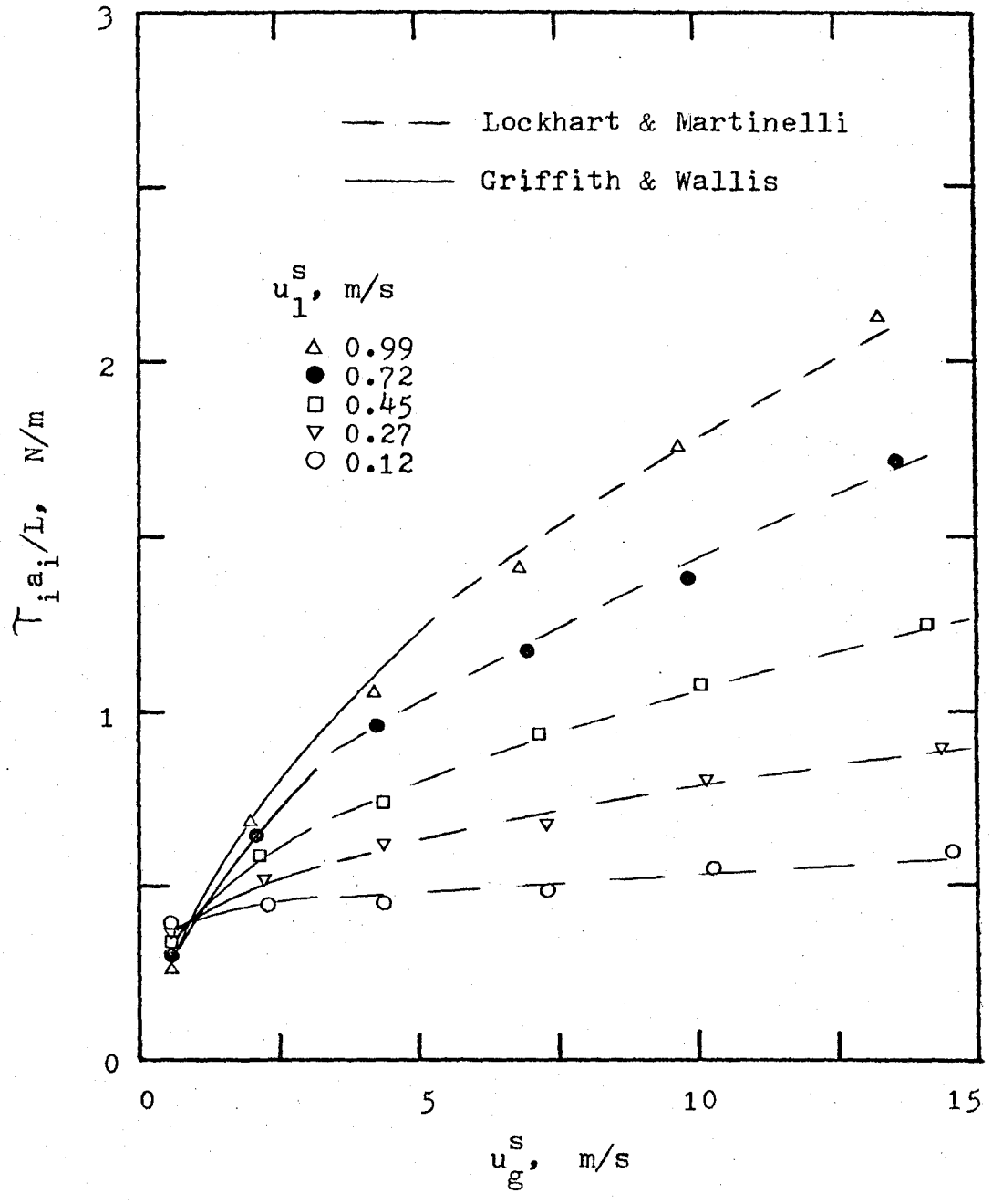

Fig 6-15. Interfacial shear term, calculated from measured pressure drop and void fraction, versus superficial gas velocity.

mass transfer coefficient at the interface is independent of the hydrodynamic conditions. Measurements of the rate of reaction allow the interfacial area to be calculated, providing one knows the reaction kinetic parameters, diffusivities and solubilities. Using this technique, correlations of the interfacial area in terms of the pressure drops, void fractions and flowrates, such as those presented by Shilimkan and Stepandek (50), have been developed. However this method requires relatively long test sections, on the order of 1,500 mm, and thus provides only gross volume averages. In addition, equation (2.4) is one-dimensional, and the interfacial shear term is only that component acting in the direction parallel to the flow. Thus the area whose surface is also parallel to the flow is required.

The interfacial shear term could be further evaluated in the annular flow regime. Likening the effect of the wavy interface of the liquid film on the gas flow to roughness in a pipe wall, the interfacial shear stress is evaluated by applying single-phase methods to the gas core, thus $\tau_i = f \rho u_g^2$. The friction factor is commonly correlated in terms of the film thickness, the thicker the film the 'rougher' the interface. Relations for the friction factor and film thickness are available, such as those of Henstock and Hanratty (51). The interfacial shear stress in the core due to the entrained liquid can be neglected. But knowledge of the amount of entrained liquid is required.

to arrive at the film thickness. Though correlations for the entrained fraction do exist, the degree of entrainment is a strong function of the system geometry, such as the type of mixer (7, p. 151). Thus direct measurement of the entrained liquid fraction is required if a reasonable estimate of the interfacial shear stress in annular flow is to be calculated.

6.6 Mass Transfer Coefficient Spectra

Typical mass transfer spectra obtained with the isolated wire electrodes are shown in Figure 6-16. The slug regime spectrum is seen to be that of a periodic process. The spectrum is not truly periodic because of randomness in the amplitude and frequency, resulting in a peak with a wide base. The annular regime spectrum approximates that of a random process, comparable to spectra obtained in single-phase flow, where the fluctuations are related to the character of the turbulence at the wall. Churn flow is a transition regime between the slug and annular flow regimes and its spectrum is seen to form a transition between the slug and annular regime spectra. For frequencies greater than about 40 Hz, all three spectra are similar in shape. The differences at the lower frequencies are highlighted in Figure 6-17.

Kutateladze el al (52) showed that the wall shear spectrum density function is linearly related to the mass transfer spectrum density function. Thus Figure 6-17 should

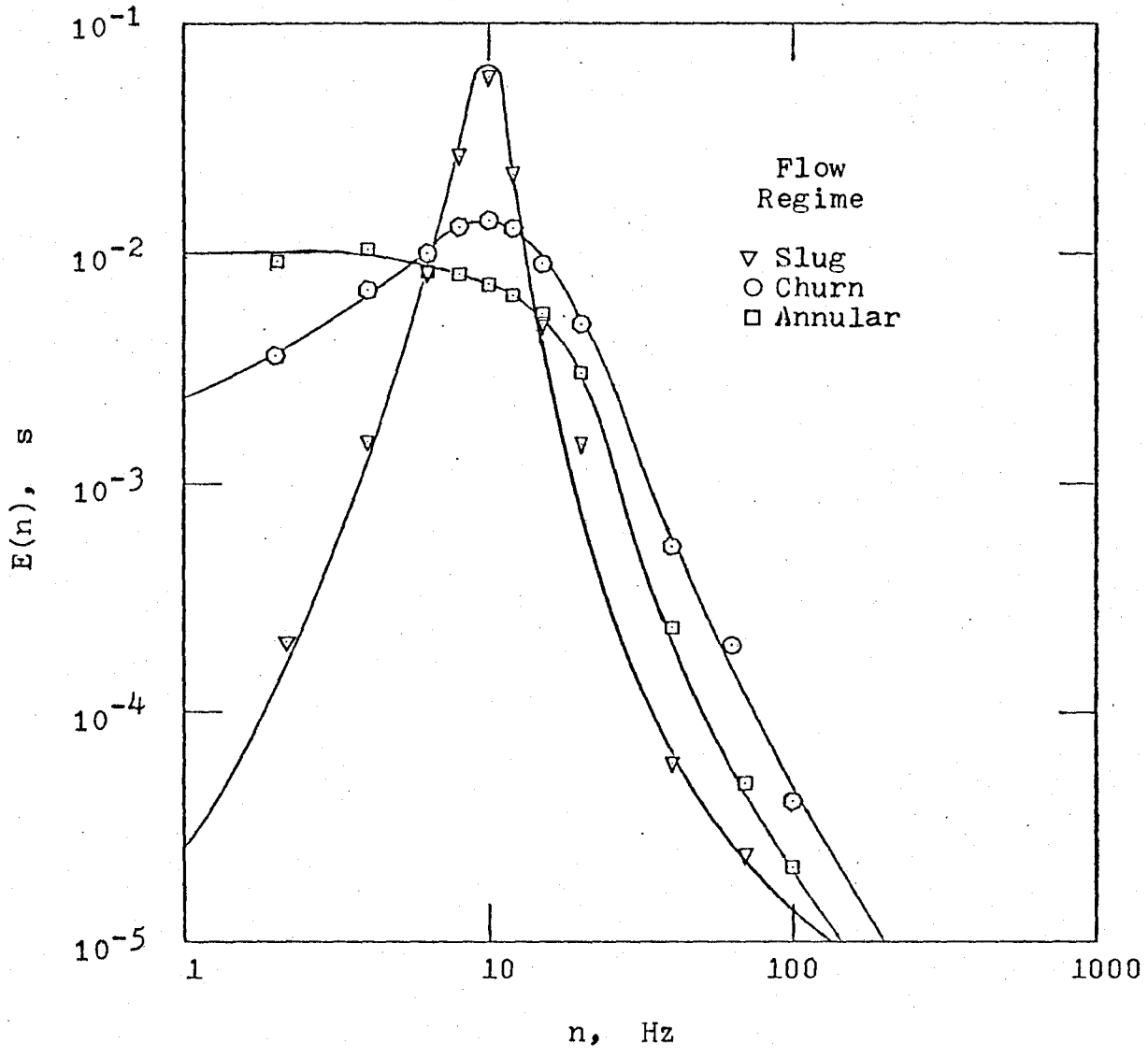

Fig 6-16. Two-phase mass transfer coefficient spectra, log scale.

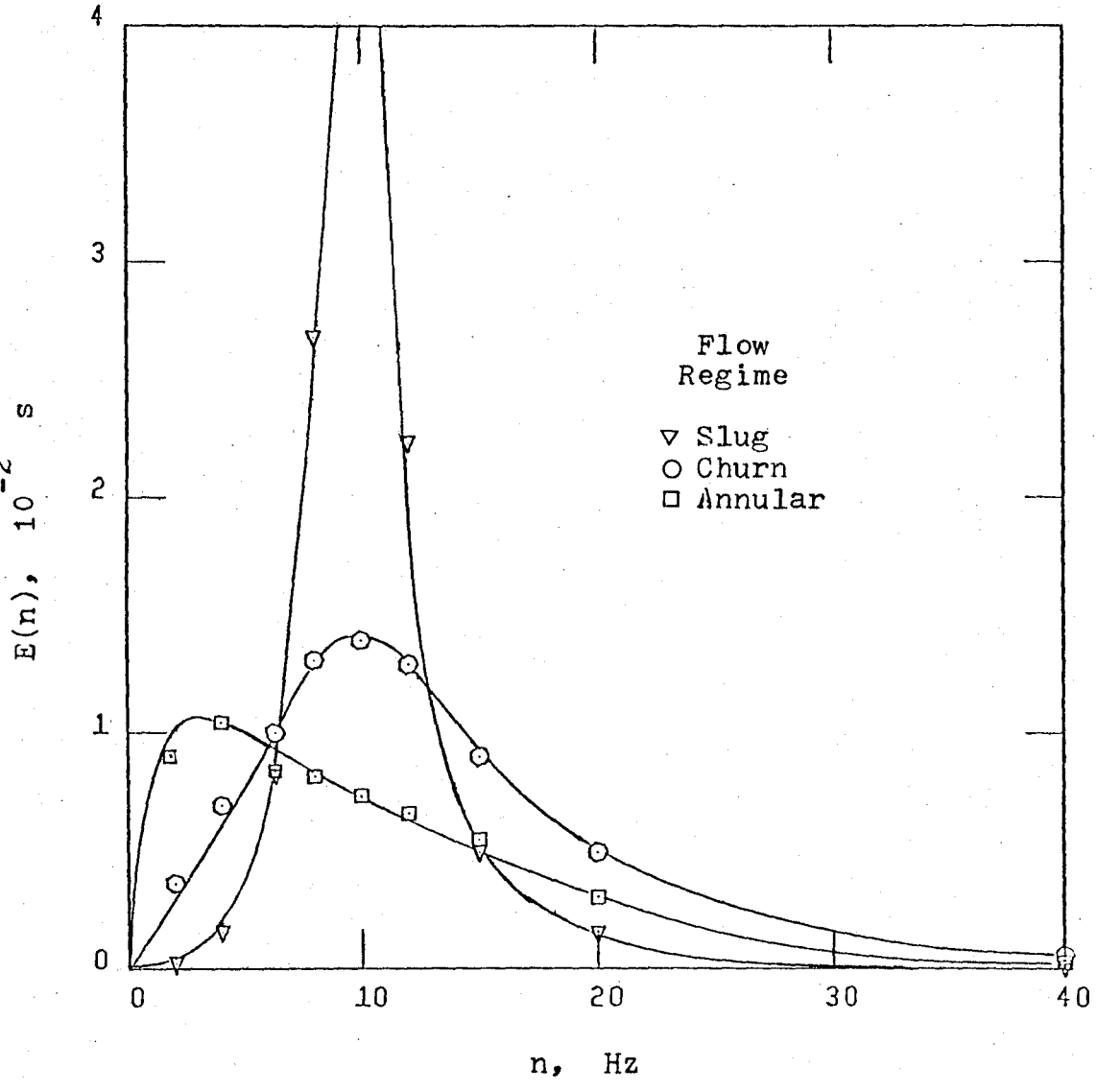

Fig 6-17. Two-phase mass transfer coefficient spectra, linear scale.

be similar to Figure 2-3, the latter giving the wall shear spectra obtained in two-phase flow by Kutateladze et al (9). The observed discrepancy between the two set of spectra could be attributed to the following points.

The spectral density functions are shown going to zero at the origin in Figure 6-17. This was done because the procedure for measuring the spectra involved setting the D.C. level of the mass transfer fluctuations to zero. But this was not actually measured to be so. Kutateladze et al's spectra indicate a significant D.C. component.

The data points at the two lowest frequencies, 2 and 4 Hz in Figure 6-17, were calculated from continuity requirements, that is the sum of the signal components as filtered by the spectrum analyzer must equal the total unfiltered signal. Thus the actual shapes of the spectra less than 6 Hz have only been guessed.

Finally, the data points in Figure 6-17 are shown joined with a smooth line. The line might in fact not be quite so smooth. This could only be proved or disproved by taking additional data points. Kutateladze et al's study did not involve the measurement of discrete values of the spectral density function. Their signals were analyzed on a computer to give a more detailed spectra.

This discussion indicates that the spectra obtained in this study must be considered as qualitative and not quantitative in nature.

CHAPTER 7

CONCLUSIONS AND RECOMMENDATIONS

The results of an investigation of mass transfer and shear stress at the wall for cocurrent gas-liquid flows in a vertical tube have been reported. The electrochemical method was used to measure the mass transfer coefficients at the tube wall. It has been shown that the mass transfer coefficients can be used to obtain the wall shear stresses in two-phase flow to an accuracy ± 20%.

A series of single-phase experiments illustrated the characteristics of the electrochemical method. The most important result was the demonstration of the sensitivity of the method to wall roughness. Future test sections should have the electrodes permanently mounted in the body to ensure flushness with the wall. The use of platinum electrodes should markedly reduce the effect of electrode contamination.

The observed flow regimes were slug, churn and annular. The theoretical flow regime map of Dukler and Taitel successfully predicted these regimes.

With knowledge of the flow regime, void fractions and pressure drops were predicted to an accuracy of ±15% with the correlations of Griffith and Wallis, and Lockhart and Martinelli as modified by Davis. This accuracy is in accordance with the results of other investigators and places confidence in the measured values.

Two-phase mass transfer coefficients have been measured. Their accuracy is estimated to be $\pm 4\%$ with a reproducibiblity of 5%.

Two-phase mass transfer coefficients were predicted using the Leveque solution for $L^+ < 1{,}000$ to an accuracy of $\pm 8\%$. The success of Leveque indicates that the condition of a laminar boundary layer is correct. This follows from the thinness of the concentration boundary layer at high Schmidt numbers. In this study, the dimensionless boundary layer thickness was less than one ($\delta_c^+ < 1$).

Two-phase fully developed mass transfer coefficients were predicted using the single-phase empirical relation of Shaw and Hanratty to an accuracy of $\pm 5\%$. The success of this relationship indicates that the eddy diffusivity at the wall is the same for two-phase flows as it is in single-phase flows. This again probably follows from the thinness of the concentration boundary layer, the rate of mass transfer being dominated by the wall and not events taking place outside of the boundary layer.

The wall shear stresses calculated from the measured mass transfer coefficients using the relations of Leveque, and Shaw and Hanratty, agree with the wall shear stresses calculated from the measured void fractions and pressure drops to within $\pm 20\%$. Calculation of the wall shear stress from the mass transfer coefficient does not require knowledge of the flow regime. The tolerance of $\pm 20\%$ matches the bounds of the estimated experimental error. This error could best be re-

duced by improving the accuracy of the ferricyanide diffusivity and/or the accuracy of the ferricyanide concentration.

The interfacial shear terms were predicted, with knowledge of the flow regime, from the correlations of Griffith and Wallis, and Lockhart and Martinellis as modified by Davis, and provided good agreement with the interfacial shear terms calculated from the measured void fractions and pressure drops.

The ability of mass transfer spectra to identify flow regimes has been demonstrated. Future studies of mass transfer spectra should employ recording of the signal on tape and subsequent spectrum analysis by computer. The analysis should concentrate on frequencies between 1 and 20 Hz.

There would appear to be a paradox in that the rate of mass transfer in a two-phase flow was found to be sufficiently sensitive to events taking place outside of the concentration boundary layer, to enable spectra of the fluctuations to be used for flow regime identification, and yet sufficiently insensitive, to enable single-phase relations to be used to obtain the wall shear stress from the average rate of mass transfer. This can be accounted for in part by the nature of the measurements. The spectra measurements used wire electrodes, the wall shear stress measurements used ring electrodes. The latter have areas two orders of magnitude greater than the former and thus average out the fluctuations over much larger surfaces. However a better explanation of the paradox is required and thus suggests the need for a fundamental experiment directed at seeking its solution.

LIST OF REFERENCES

1. Hewitt, G.F., "The Role of Experiments in Two-Phase Systems With Particular Reference to Measurement Techniques," Progress in Heat and Mass Transfer, 6, 295-343 (1972).

2. Sutey, A.M., "Mass Transfer at the Solid-Liquid Interface for Climbing Film Flow in an Annular Duct," Ph.D. thesis, Oregon State Univ. (1967).

3. Kutateladze, S.S., et al, "Application of the Electrodiffusion Method in the Study of Gas-Liquid Flows," Heat Transfer - Soviet Research, 5, 4, 42-46 (1973).

4. Collier, J.G., Convective Boiling and Condensation, McGraw-Hill (1972).

5. Govier, G.W., and Aziz, K., The Flow of Complex Mixtures in Pipes, Van Nostrand Reinhold (1972).

6. Wallis, G.B., One Dimensional Two-Phase Flow, McGraw-Hill (1969).

7. Hewitt, G.F., and Hall-Taylor, N.S., Annular Two-Phase Flow, Permagon Press (1970).

8. Banerjee, S., and Hancox, W.T., "Transient Thermohydraulics Analysis for Nuclear Reactors", 6th Int. Heat Transfer Conf., Toronto, Keynote Paper KS-23, 6, 311-337 (Aug. 1978).

9. Kutateladze, S.S., et al, "Spectral Characteristics of Vertical Two-Phase Flow," Soviet Physics - Doklady, 16, 9, 718-719 (1972).

10. Hewitt,G.F., and Roberts, D.N., "Studies of Two-Phase Flow Patterns by Simultaneous X-Ray and Flash Photography," AERE-M 2159 (1969).

11. Dukler, A.E., and Taitel, Y., "Flow Regime Transitions for Vertical Upward Gas-Liquid Flow: A Preliminary Approach Through Physical Modelling," Notes from the course 'Two-Phase Flow Measurements', Fluid Dynamics Institute, Dartmouth, short course 78-1 (Aug. 1978).

12. Griffith, P., and Wallis, G.B., "Two-Phase Slug Flow," Trans. A.S.M.E., J. of Heat Transfer, 83, 307-320 (Aug. 1961).

13. Golan, L, "An Air-Water Study of Vertical Upward and Downward Two-Phase Flow," Ph.D. thesis, Lehigh Univ. (1968).

14. Hughmark, G.A., "Holdup and Heat Transfer in Horizontal Slug Gas-Liquid Flow," Chem. Eng. Sci., 20, 1007-1010 (1965).

15. Zuber, N., and Findlay, J.A., "Average Volumetric Concentration in Two-Phase Flow Systems," Trans. A.S.M.E., J. of Heat Transfer, 87, 453-468 (Nov. 1965).

16. Lockhart, R.W., and Martinelli, R.C., "Proposed Correlation of Data for Isothermal Two-Phase, Two-Component Flow in Pipes," Chem. Eng. Progress, 45, 39-47 (1949).

17. Chisholm D., "A Theoretical Basis for the Lockhart-Martinelli Correlation for Two-Phase Flow," Int. J. Heat Mass Transfer, 10, 1767-1778 (1965).

18. Gill, L.E., Hewitt, G.F., and Lacey, P.M.C., "Data on the Upwards Annular Flow of Air-Water Mixtures", Chem. Eng. Sci., 20, 71-88 (1965).

19. Davis, W.J., "The Effect of the Froude Number in Estimating Vertical Two-Phase Gas Liquid Friction Losses," British Chem. Eng. 8, 462-465 (1963).

20. Oshinowo, T., and Charles, M.E., "Vertical Two-Phase Flow: Part II. Holdup and Pressure Drop," Can. J. Chem. Eng., 52, 438-448 (1974).

21. Lin, C.S., Denton, E.B., Gaskill, H.S., and Putnam, G.L., "Diffusion-Controlled Electrode Reactions," Ind. Eng. Chem., 43, 2136-2143 (1951).

22. Dawson, D.A., and Trass, O., "Mass Transfer at Rough Surfaces," Int. J. Heat Mass Transfer, 15, 1317-1336 (1972).

23. Acosta, R.E., "Transport Processes in High Rate Electrolysis," LBL-2242 (1974).

24. Van Shaw, P., Reiss, L.P., and Hanratty, T.J., "Rates of Turbulent Transfer to a Pipe Wall in the Mass Transfer Entry Region," AIChE J., 9, 362-364 (1963).

25. Son, J.S., and Hanratty, T.J., "Limiting Relation for the Eddy Diffusivity Close to a Wall," AIChE J., 13, 689-696 (1967).

26. Shaw, D.A., and Hanratty, T.J., "Turbulent Mass Transfer Rates to a Wall for Large Schmidt Numbers," AIChE J., 23, 28-37 (1977).

27. Friend, W.L., and Metzner, A.B., "Turbulent Heat Transfer Inside Tubes and the Analogy Among Heat, Mass, and Momentum Transfer," AIChE J., 4, 393-402 (1958).

28. Taylor, J.L., and Hanratty, T.J., "Influence of Natural Convection on Mass Transfer Rates for the Electrolysis of Ferricyanide Ions," Electrochimica Acta, 19, 529-533 (1974).

29. Gay, B., Mackley, N.V., and Jenkins, J.D., "Shell-Side Heat Transfer in Baffled Cylindrical Shell- and Tube Exchangers - An Electrochemical Mass-Transfer Modelling Technique," Int. J. Heat Mass Transfer, 19, 995-1002 (1976).

30. Shaw, D.A., and Hanratty, T.J., "Influence of Schmidt Number on the Fluctuations of Turbulent Mass Transfer to a Wall," AIChE J., 23, 160-168 (1977).

31. Sirkar, K.K., and Hanratty, T.J., "Relation of Turbulent Mass Transfer to a Wall at High Schmidt Numbers to the Velocity Field," J. Fluid Mech., 44, 589-603 (1970).

32. Kirdyashkin, A.G., "Investigation of Turbulent Gas-Liquid Flows," Fluid Mechanics - Soviet Research, 6, 5, 31-61 (1977).

33. Mizushina, T., "The Electrochemical Method in Transport Phenomena," Advance in Heat Transfer,7, 87-161 (1971).

34. Newman, J.S., Electrochemical Systems, Prentice-Hall, Englewood Cliffs, N.J. (1973).

35. Eisenberg, M., Tobias, C.W., and Wilke, C.R., "Ionic Mass Transfer and Concentration Polarization at Rotating Electrodes," J. Electrochemical Society, 101, 306-319 (1954).

36. Hicks, R.E., and Pagotto, N., "The Effect of Drag Reducing Polymers and Plastics on the Ferricyanide Concentration in Electrolyte Solutions Used in Mass Transfer Determinations," CSIR Report CENG M-024 (1974).

37. Knudsen, J.G., and Katz, D.L., Fluid Dynamics and Heat Transfer, McGraw-Hill (1958).

38. Chilton, R.H., and Colburn, A.P., "Mass Transfer (Absorption) Coefficients,", Ind., Eng. Chem., 26, 1183-1187 (1934).

39. Deissler, R.G., "Analysis of Turbulent Heat Transfer, Mass Transfer, and Friction in Smooth Tubes at High Prandtl and Schmidt Number," NACA Tech. Note 3145 (1954).

40. Notter, R.H., and Sleicher, C.A., "The Eddy Diffusivity in the Turbulent Boundary Layer Near a Wall," Chem. Eng. Sci., 26, 161-171 (1971).

41. Lin, C.S., Moulton, R.W., and Putnam, G.L., "Mass Transfer Between Solid Wall and Fluid Streams," Ind. Eng. Chem., 45, 636-640 (1953).

42. Heidrick, T.R., "The Structure of Fully Developed Flow in Pipes," Ph.D. thesis, Univ. Manitoba (1974).

43. Meek, R.L., and Baer, A.D., "Turbulent Heat Transfer and the Periodic Viscous Sublayer," Int. J. Heat Mass Transfer, 16, 1385-1396 (1973).

44. Popovich, A.T., and Hummel, R.L., "Experimental Study of the Viscous Sublayer in Turbulent Pipe Flow," AIChE J., 13, 854-859 (1967).

45. Banerjee, S., "A Note on Turbulent Mass Transfer at High Schmidt Number," Chem. Eng. Sci., 26, 989-990 (1971).

46. Brodkey, R.S., McKelvey, K.N., Hershey, H.C., and Nychas, S.G., "Mass Transfer at the Wall as a Result of Coherent Structures in A Turbulently Flowing Liquid," Int. J. Heat Mass Transfer, 21, 593-603 (1978).

47. Pinczewski, W.V., and Sideman, S., "A Model for Mass (Heat) Transfer in Turbulent Tube Flow. Moderate and High Schmidt (Prandtl) Numbers," Chem. Eng. Sci., 29, 1969-1976 (1974).

48. Oliver, D.R., and Hoon, A.Y., "Two-Phase Non-Newtonian Flow. Part II: Heat Transfer," Trans. Instn Chem. Engrs., 46, T116-T121 (1968).

49. Michiyoshi, I, "Two-Phase Two-Component Heat Transfer," 6th Int. Heat Transfer Conf., Toronto, Keynote Paper KS-17, 6, 219-233 (Aug. 1978).

50. Shilimkan, R.V., and Stepanek, J.B., "Interfacial Area in Cocurrent Gas-Liquid Upward Flow in Tubes of Various Size," Chem. Eng. Sci., 32, 149-154 (1977).

51. Henstock, W.H., and Hanratty, T.J., "The Interfacial Drag and the Height of the Wall Layer in Annular Flows," AIChE J., 22, 990-1000 (1976).

52. Kutateladze, S.S., Nakoryakov, V.E., Burdukov, A.P., and Guvakov, A.I., "Spectral Density of Fluctuations of Friction in a Turbulent Wall Flow," Soviet Physics - Doklady, 16, 2, 87-89 (1971).

53. Shafer, M.R.,"Performance Characteristics of Turbine Flowmeters," Trans. A.S.M.E., J. of Basic Eng., 83, 471-485 (1962).

54. Fischer & Porter, "Variable Area Flowmeter Handbook, Volume 1 - Basic Rotameter Principles," Catalog No. 10A1021 (1976).

55. Gordon, S.L., Newman, J.S., and Tobias, C.W., "The Role of Ionic Migration in Electrolytic Mass Transport," Ber. Bunsenges. Physik. Chem., 70, 414-419 (1966).

56. Selman, J.R., "Measurement and Interpretation of Limiting Currents," UCRL - 20557 (1971).

57. Eisenberg, M., Tobias, C. , and Wilke, C.R., "Selected Physical Properties of Ternary Electrolytes Employed in Ionic Mass Transfer Studies," Electrochemical Soc. J., 103, 413-416 (1956).

58. Tonini, R.D., Remorino, M.R., and Brea, F.M., " Determination of Diffusion Coefficients with a Pipe Wall Electrode," Electrochimica Acta, 23, 699-704 (1978).

59. Vogel, A.I., Quantitative Inorganic Analysis, (3rd ed.) Longmans - Green (1961).

NOMENCLATURE

a	Surface area	m^2
A	Cross-sectional area of the tube	m^2
c	Chemical concentration	molar
C	A constant	
C_d	Drag coefficient	
d	Pressure transducer drift	volt
D	Diameter of the tube	m
$\mathfrak{D}$	Molecular diffusivity	m^2/s
$E(n)$	Power spectral density function	s
F	Faraday's constant	A s
$F(n_c)$	Power spectral density of mass transfer fluctuations at the frequency n_c	m^2/s
g	Acceleration due to gravity	m/s^2
G	Mass flux	kg/m^2s
h	Arbitrary scalar field	
i	Electrochemical cell current for wire electrode	mA
I	Electrochemical cell current for ring electrode	mA
k	Local mass transfer coefficient	m/s
$k'(n_c, \Delta n)$	RMS value of mass transfer fluctuations passed by a bandpass filter centred at frequency n_c and having vandwidth Δn	m/s

K	Space-averaged mass transfer coefficient	m/s
L	Length	m
n	Frequency	Hz
N	Chemical mass flux	$mole/m^2s$
P	Pressure	kPa
Q	Volume flow rate	ml/s
r	Instrument reading	
R	Gas constant	J/kg K
T	Temperature	^oC
u	Flow velocity **in z direction**	m/s
u^s	Superficial velocity = Q/A	m/s
u^*	Friction velocity = $(\tau_w/\rho_l)^{\frac{1}{2}}$	m/s
U	**Total flow velocity**	**m/s**
v	Electrochemical cell voltage	volt
V	Volume	m^3
X	Lockhart and Martinelli parameter	
X_D	Davis modified X parameter	
y	Distance from wall, normal to the flow	m
z	Distance downstream, parallel to flow	m
Z	Ion charge	

Greek Symbols

α	Void fraction	%
δ	Boundary layer thickness	mm

δ_c = concentration

δ_v = hydrodynamic

δ_t = thermal

ΔP	Pressure drop	kPa
ε	Eddy diffusivity	m^2/s
ζ	Surface roughness	mm
Θ	Potential field	volt/m
μ	Absolute viscosity	kg/m s
ν	Kinematic viscosity	m^2/s
ρ	Density	kg/m^3
σ	Surface tension	kg/s^2
τ	Shear stress	N/m^2
ϕ	Lockhart and Martinelli parameter	
ψ	**Mobility of transferred ion**	**m^2 mole/J s**

Subscripts

A	Accelerational
b	Bulk
c	Critical
e	Electrode
f	Film
F	Frictional
g	Gas
G	Gravitational
i	Gas-liquid interface
l	Limiting
l	Liquid
r	Rotameter
tp	Two-phase
w	Wall

∞ Fully-developed

Superscripts

s Superficial

+ Dimensionless quantity

- Time-averaged (overscore)

' Fluctuating

Dimensionless Numbers

c^+ Concentration = $(c - c_w)/(c_b - c_w)$

f Friction factor = $2 \tau_w / \rho u_b^2$

K^+ Mass transfer coefficient = K / u^*

L^+ Electrode length = $L_e u^* / \nu_1$

Re Reynolds number = $D u_b / \nu_1$

Sc Schmidt number = $\nu_1 / \mathcal{D}$

t Transference number

W Critical Weber number = $u_c^2 \rho d / \sigma$

y^+ Distance perpendicular to the flow = $y u^* / \nu_1$

z^+ Distance parallel to the flow = $z u^* / \nu_1$

δ^+ Boundary layer thickness = $\delta u^* / \nu_1$

APPENDIX 1

CALIBRATIONS

All the calibration equations presented herein are best line fits to the calibration data. They are reported with the 95% confidence intervals of the slope and intercept.

A.1.1 Pressure Transducers

The pressure drops were measured using three Validyne differential pressure transducers labelled DPT1, DPT2 and DPT3, located at the pressure rings PR1, PR2 and PR3, respectively. A precision Bourdon pressure gauge was used as the reference in the calibration against a specified air pressure. Figure A.1-1 is a typical plot of differential pressure versus the transducer reading.

The calibration equations are

DPT1: (140 kPa diaphragm)

$$\Delta P_1 = (20.6 \pm 0.1)(r - d) \qquad (A.1\text{-}1)$$

DPT2: (35 kPa diaphragm)

$$\Delta P_2 = (6.89 \pm 0.01)(r - d) \qquad (A.1\text{-}2)$$

DPT3: (7 kPa diaphragm)

$$\Delta P_3 = (1.37 \pm 0.01)(r - d) \qquad (A.1\text{-}3)$$

where ΔP is the differential pressure in kPa and the reading r of the transducer is given in volts. The drift of each transducer was measured at the beginning and the end of each experiment and then averaged to give d.

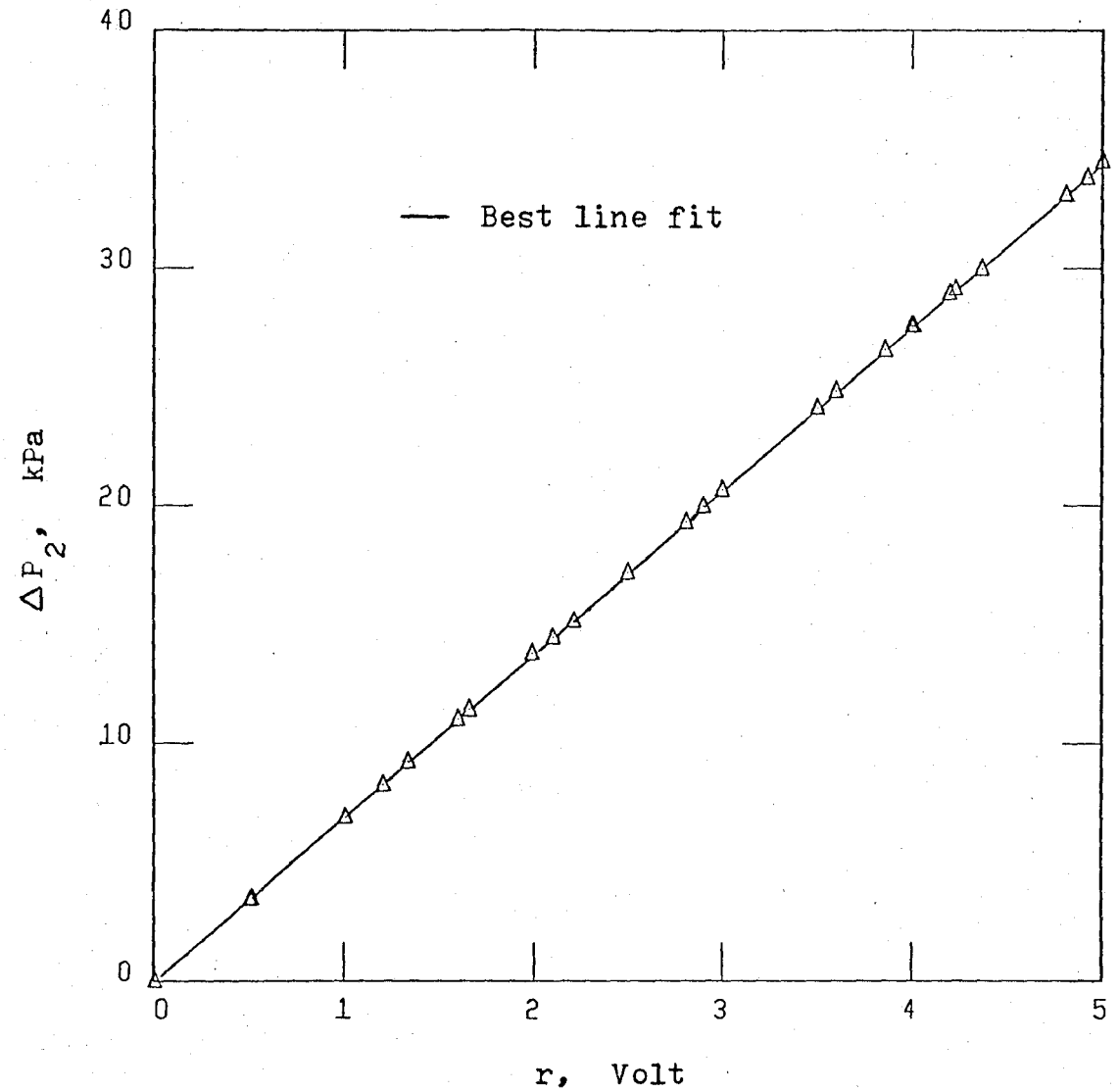

Fig. A.1-1. Calibration curve for pressure transducer DPT2.

A.1.2 Turbine Flowmeters

The volume flow rate of the electrolyte was measured with a turbine flowmeter for the majority of the experiments. Three units, Flow Technology models FT-8M5-LB, FT-810-LB and FT-12M20-LB, were used before bearing failures took them out of service. Figure A.1-2 is a typical plot of flow rate versus flowmeter reading. The calibration was determined by measuring the time for a specified volume of water to pass through the flowmeter. The effect of the change in viscosity when used with the electrolyte is considered negligible (53).

The calibration equations are

FT-8M5-LB: (50 to 500 ml/s)

$$Q_l = (182 \pm 2)\, r - (6 \pm 4) \qquad (A.1\text{-}4)$$

FT-810-LB: (100 to 1000 ml/s)

$$Q_l = (355 \pm 3)\, r - (10 \pm 5) \qquad (A.1\text{-}5)$$

FT-12M20-LB: (200 to 2000 ml/s)

$$Q_l = (637 \pm 5)\, r - (3 \pm 6) \qquad (A.1\text{-}6)$$

where Q_l is the liquid flow rate in ml/s and the reading r is given in volts.

A.1.3 Liquid Rotameter

After the failure of the turbine flowmeters, a Dwyer liquid rotameter was used to measure the electrolyte flow rate. The calibration was determined by measuring the time for a specified volume of water to pass through the rotameter. The effect of the change in viscosity when used with the electrolyte

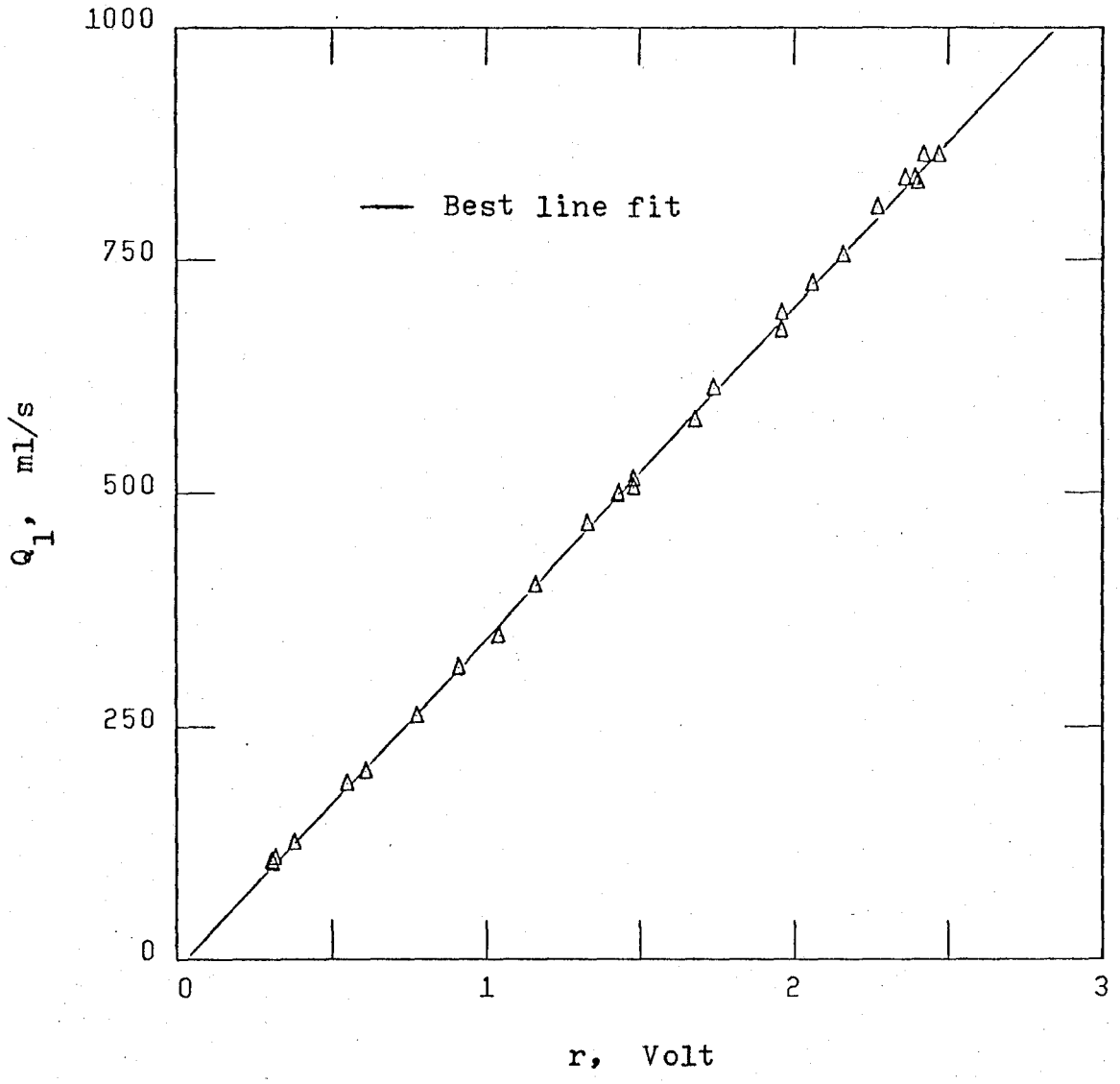

Fig. A.1-2. Calibration curve for turbine flowmeter FT-810-LB.

is considered negligible (54).

The calibration equation is

$$Q_l = (63.9 \pm 0.4)\ r + (1 \pm 1) \qquad (A.1\text{-}7)$$

where Q_l is the liquid flow rate in ml/s and the reading r is given in USgpm.

A.1.4 Gas Rotameters

The flow rate of the nitrogen was measured with a Fischer & Porter series 10A3000 rotameter with two interchangeable floats. The rotameter was calibrated by measuring the time for a specified volume of air to flow through the unit. The volume was measured using a natural gas meter. Figure A.1-3 gives a plot of flow rate, normalized with respect to rotameter temperature and pressure, versus rotameter reading for Float I. For this calibration, the rotameter temperature was constant at 21 °C and the rotameter pressure was varied from 70 to 345 kPa(g).

The calibration equations are

Float 1: (120 to 4450 ml/s)

$$Q_g = \left[(38.4 \pm 0.2)\ r - (230 \pm 10)\right]\left[\frac{P_r + 101}{T_r + 273}\right]^{\frac{1}{2}} \qquad (A.1\text{-}8)$$

Float 2: (40 to 2290 ml/s)

$$Q_g = \left[(20.1 \pm 0.2)\ r - (150 \pm 10)\right]\left[\frac{P_r + 101}{T_r + 273}\right]^{\frac{1}{2}} \qquad (A.1\text{-}9)$$

where

P_r = rotameter pressure in kPa(g)

T_r = rotameter temperature in °C

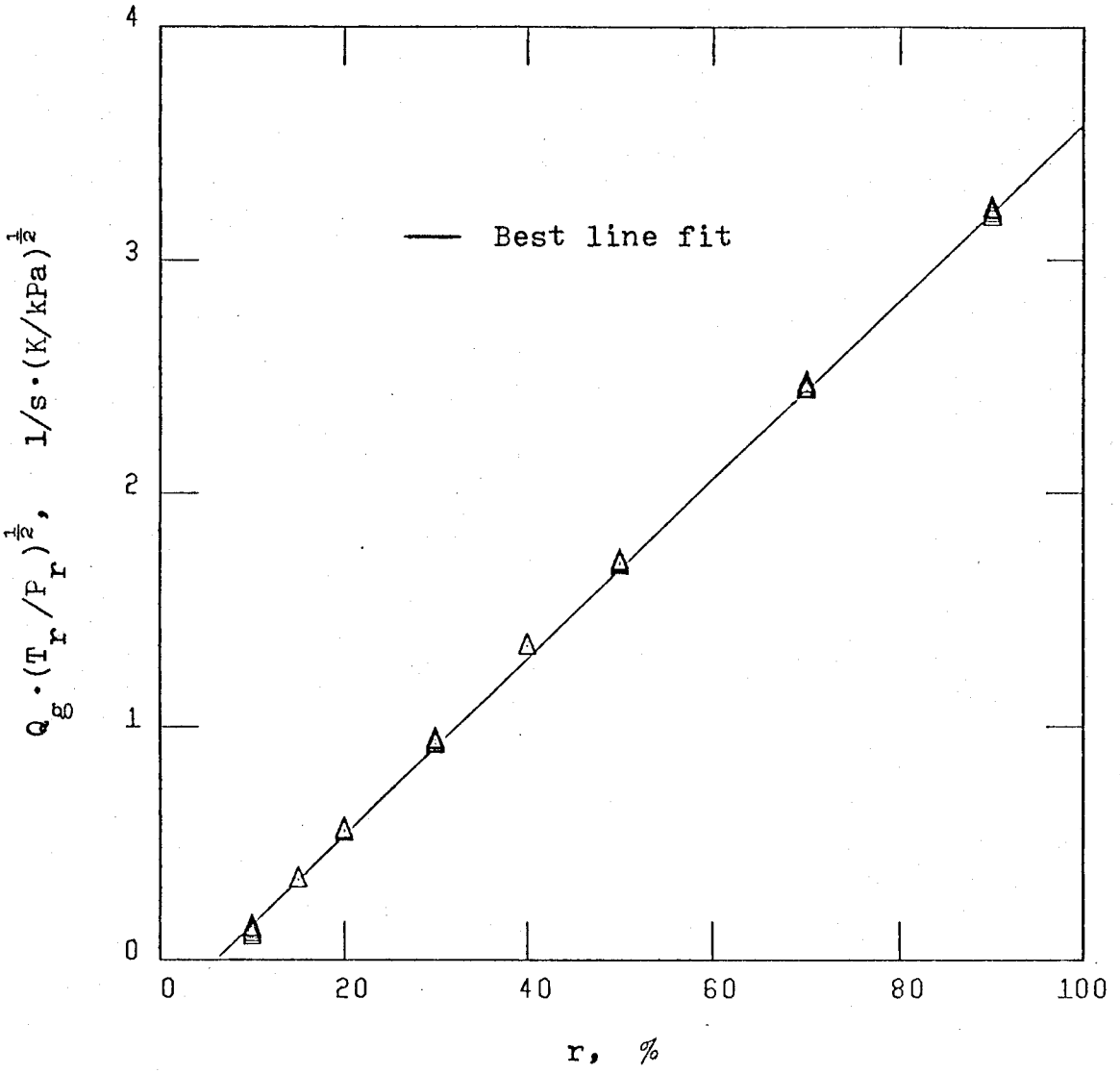

Fig. A.1-3. Calibration curve for gas rotameter with Float I. The measured flow rate is normalized with respect to rotameter temperature and pressure, and is referenced at 21°C and 101 kPa (a).

r = rotameter reading in %

Q_g = flow rate in ml/s referenced at 101 kPa(a) and 21 °C

A.1.5 Voidmeter

The void fraction was calculated from the volume of liquid trapped between the quick-closing valves situated at the ends of the test section. The voidmeter was calibrated by closing the lower quick-closing valve, adding a specified volume of electrolyte through the upper valve, opening the drain and measuring the volume of electrolyte which drained out. In this manner such side effects as viscous holdup in the test section were negated. From knowledge of the total volume between the quick-closing valves, the void fraction was then calculated. The resulting calibration is shown in Figure A.1.4.

The calibration equation is

$$\alpha = (92.0 \pm 0.4) - (1.16 \pm 0.01)\, r \qquad (A.1\text{-}10)$$

where α is the void fraction in % and r the measured amount of trapped liquid in ml.

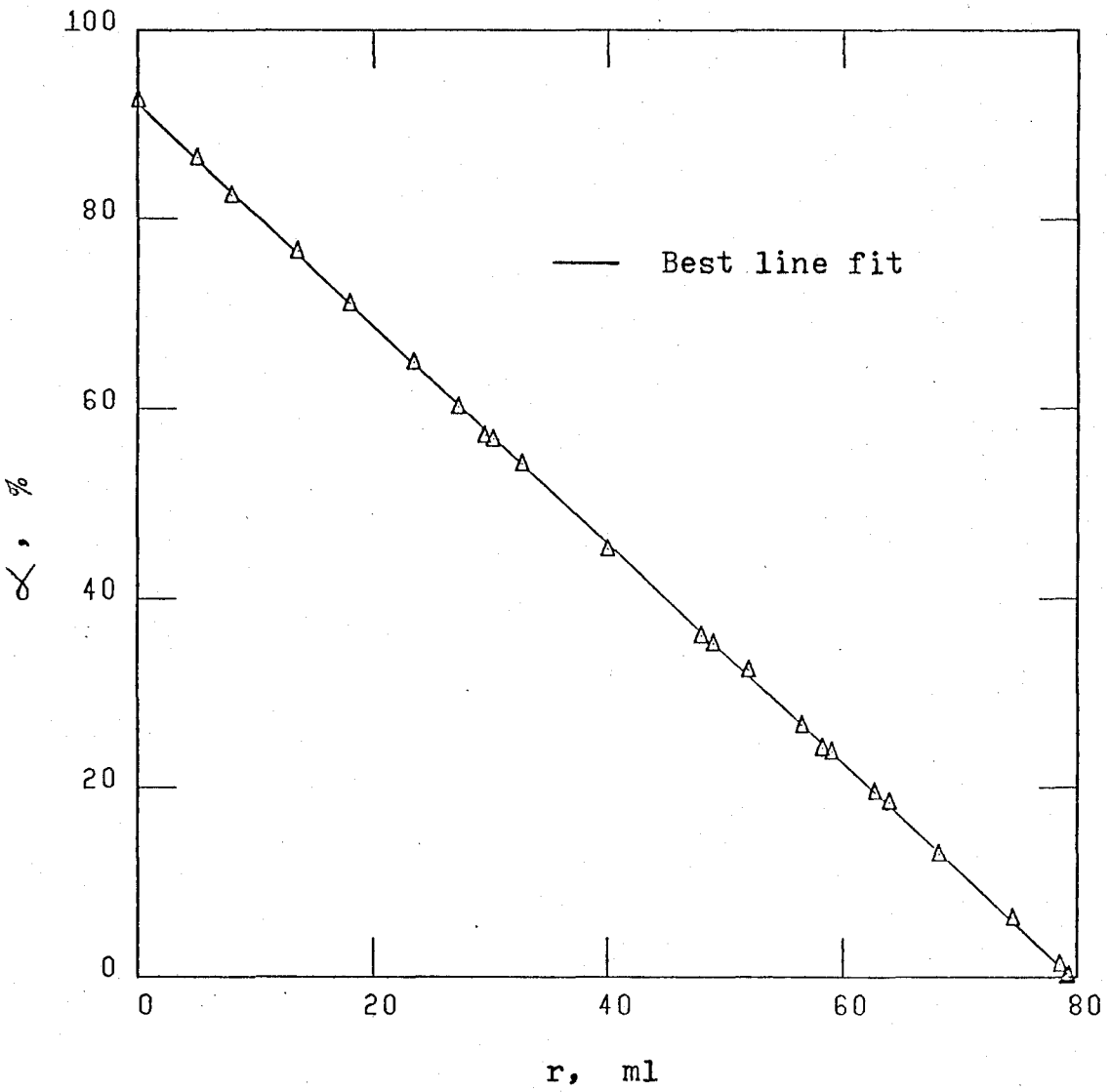

Fig. A.1-4. Calibration curve for voidmeter.

APPENDIX 2

PHYSICAL PROPERTIES

All properties are referenced at 25°C.

A.2-1 Electrolyte

The density and viscosity of the electrolyte were calculated from the polynomial equations of Boeffard as presented by Acosta (23). The equations are

$$\rho_1 = 997.02 + 44.23\, C_h + 171.18\, C_3 + 231.19\, C_4 - 1.33\, C_h^2 - 7.87\, C_h C_3 - 9.78\, C_h C_4 \qquad (A.2\text{-}1)$$

$$\mu_1 = 0.96714 + 0.09622\, C_h - 0.20528\, C_3 + 0.090255\, C_4 + 0.05404\, C_h^2 + 0.53303\, C_3^2 + 0.43505\, C_4^2 + 0.23546\, C_h C_3 + 0.302585\, C_h C_4 + 0.99923\, C_3 C_4 \qquad (A.2\text{-}2)$$

where

ρ_1 = electrolyte density in kg/m^3, ± 0.2%

μ_1 = electrolyte absolute viscosity in g/m s, ± 1.0%

C_3 = molar concentration of potassium ferricyanide

C_4 = molar concentration of potassium ferrocyanide

C_h = molar concentration of sodium hydroxide

The quoted error limits were estimated from the experimental errors in the concentrations and temperature, and the standard deviation of the polynomial fit.

The values calculated for the density with equation (A.2-1) are within ±0.2% of the values derived from

experimental densities for aqueous sodium hydroxide given in the International Critical Tables, Vol. III, page 79. The change in the sodium hydroxide density due to the addition of potassium ferri- and ferrocyanide was allowed for by assuming negligible volume change upon addition of these chemicals.

The values calculated for the viscosity with equation (A.2-2) are within ± 1.0% of the experimental viscosities given in Landolt-Bornstein's "Zahlenwerte und Funktionen aus Physik, Chemic, Astonomie, Geophysik, Technik", Vol. II, Part 5, Section b, page 92.

The diffusion coefficient for the ferricyanide is most often calculated using the Stokes-Einstein equation

$$\mathcal{D}\mu/T = C \times 10^{-15} \qquad (A.2\text{-}3)$$

where

$\mathcal{D}$ = diffusivity in m^2/s

μ = absolute viscosity in kg/m s

T = absolute temperature in K

Depending upon the source, the constant C can vary from 2.2 to 2.7, a 20% range (56). The value of Gordon, Newman and Tobias (55), C = 2.34 with a correction for the ionic strength, has been the most widely used (23, 26, 28, 30). However a recent experimental study in laminar pipe flow concluded that C = 2.6 (58). It was decided to use C = 2.5 in this investigation. This is the value determined by Eisenberg, Tobias and Wilke (57). Thus the

diffusivity for the ferricyanide was calculated using

$$\mathcal{D} = (2.5 \times 10^{-15})\ T / \mu \qquad (A.2\text{-}4)$$

The estimated error is ±4%, based upon the errors for the constant, temperature and viscosity.

Table A.2-1 gives the properties calculated with equations (A.2-1), (A.2-2) and (A.2-4) for the principal concentrations used in these experiments.

A.2.2 Nitrogen

For the nitrogen

$$\mu_g = 1.8 \times 10^{-5} \qquad \text{kg/m s}$$

$$\rho_g = P / R\ T \qquad \text{kg/m}^3$$

where

P = pressure of the gas in Pa(a)

T = absolute temperature of the gas in K

R = ideal gas constant, 297 J/kg K

The values for the viscosity and ideal gas constant for nitrogen were taken from the CRC Handbook of Chemistry and Physics.

Table A.2-1. Electrolyte Properties

[NaOH] M	Density kg/m^3	Viscosity kg/m s	Diffusivity m^2/s	Schmidt Number
1	1042	1.12×10^{-3}	6.65×10^{-10}	1620
1.75	1072	1.305	5.71	2130
2	1082	1.38	5.40	2360
3	1120	1.75	4.26	3670

$$\left[K_3 Fe (CN)_6\right] = 0.005 \text{ M}$$

$$\left[K_4 Fe (CN)_6\right] = 0.005 \text{ M}$$

APPENDIX 3

EQUIPMENT SPECIFICATIONS

A.3.1 Test Section

Main body: material - Lucite
length - 305 mm
I.D. for single-phase experiments - 12.70 mm
I.D. for two-phase experiments - 13.50 mm

Ring electrodes: material - Nickel 200
anode thickness - 25.4 mm
cathode thicknesses - R1 - 1.613 mm
R2 - 3.176 mm
R3 - 6.388 mm
distance between anode and cathode R3 - 50.8 mm

Wire electrodes: material - Platinum
diameter - 0.51 mm

Pressure rings: material - Lucite
annulus - 6.35 mm square
- 25.4 I.D.
tap holes - 0.79 mm diameter
- 6.35 mm long
distance between PR1 & PR2 - 594.0 mm
distance between PR2 & PR3 - 235.0 mm

A.3.2 Loop

Pump I: Sta-Rite swimming pool pump
Model P2RA5D-120F 3/4 HP
Capacity 25 USgpm at 39 psi

Pump II: Chemtrol centrifugal pump
Model CP-3041 1 HP
Capacity 25 USgpm at 30 psi
PVC casing and impeller
High-purity ceramic seals

Reservoir: Rosemount neutralization tank
Capacity 95 litres, black polyethylene

Quick-Closing Valves: Whitey air-operated ball valves
Model MS-131SR stainless steel
Normally open, 90° spring return

Nitrogen supply: Canada Liquid Air standard nitrogen
Tank capacity 224 ft^3

Pressure Transducers: Validyne DP15TL differential
Variable reluctance

Liquid Rotameter: Dwyer Ratemaster Model RMC-142
Capacity 0.2 - 2.2 USgpm

Gas Rotameter: Fischer & Porter 10A3000 Series
Tube FP-½-27-G-10
Float I - ½-GSVT-45-A
Capacity 3.35 scfm air
Float II - ½-GUSVT-40
Capacity 1.82 scfm air

Turbine Flowmeters: Flow Technology

Flowmeter I - FT-8M5-LB 1/2 in capacity 0.5 - 5 gpm

Flowmeter II - FT-M10-LB 1/2 in capacity 1 to 10 gpm

Flowmeter III - 12M20-LB 3/4 in capacity 2 to 20 gpm

APPENDIX 4

CHEMICAL ANALYSIS PROCEDURES

The procedures for the ferricyanide titration and sodium thiosulphate standardization are based upon those given in Vogel (59), pages 356 and 334, respectively.

A.4.1 Sodium Hydroxide

The concentration of the sodium hydroxide was determined at the beginning of every experiment. A 50 ml bulk sample was drawn from the loop. A 10 ml sample was titrated with 1.0 N hydrochloric acid, with phenolphthalein as the indicator. The average of three titrations was used to calculate the concentration.

A.4.2 Ferricyanide

To determine the concentration of the ferricyanide ion, 100 ml of the electrolyte was drawn from the loop. A 25 ml sample was acidified with 4 ml of 12 N hydrochloric acid. After 10 ml of 1.0 N potassium iodide was added, the sample was titrated to a pale yellow colour with standardized sodium thiosulphate. At this point, 25 ml of 0.1 M potassium hydrogen phthalate was added as a buffer, together with 2 ml of a 1% starch solution. The sample was then titrated with the sodium thiosulphate from deep blue to a colourless end-point. The average of three titrations was used to calculate the concentration.

A.4.3 Sodium Thiosulphate

The following procedure outlines the preparation of the standardized solution of sodium thiosulphate. Initially a nominal 0.005 N solution was made up by mixing 1.24 g of sodium thiosulphate with 1 litre of boiled-out distilled water. A reference was prepared by weighing out accurately about 0.5 g of pure, dry potassium iodate. This was dissolved in 1 litre of cold, boiled-out distilled water.

For the actual standardization, 10 ml of the prepared potassium iodate solution was drawn. To this sample was added 0.1 g of iodate-free potassium iodide and 2 ml of 1 N hydrochloric acid. The iodine sample was then titrated with the thiosulphate solution from a deep orange to a pale yellow colour. It was then diluted to 50 ml with distilled water and 2 ml of 1% starch was added. The sample was then titrated with the sodium thiosulphate from deep blue to a colourless end-point. The concentration of the sodium thiosulphate was calculated from the average of three titrations.

Three drops of chloroform were added and the solution stored in the dark to inhibit degradation.

APPENDIX 5

CHEMICAL HAZARDS

Separate to the investigation described in this report, work was carried out on application of the electrochemical method to a larger scale two-phase loop. A result of this additional work was a greater awareness of the hazards of the required chemicals. These hazards are outlined below. The level of precautions required to ensure safe operation of a loop utilizing this technique must be judged on the basis of the individual application.

The toxic nature of hydrogen cyanide is well known. As it is only a decomposition product associated with the potassium ferri and ferrocyanide, it is unlikely that the threshold limit of 10 mg/m^3 for hydrogen cyanide vapour would be exceeded during normal operation. However if thought is given to neutralization of the electrolyte upon disposal, one must recognize that the hydrogen cyanide would no longer be in an alkaline solution and as a result, more significant quantities of HCN could be formed.

The sodium hydroxide presents a much greater hazard as it is extremely corrosive to human tissue, causing burns and deep ulceration. An unfortunate characteristic is that the chemical doesn't cause immediate pain when it comes in contact with the body, but it does start causing immediate damage. Serious injury can result before one realizes that contact has been made. The greatest potential danger comes

from a mist of sodium hydroxide. Such a mist could form from a small leak in the piping with the pressurized gas phase acting as a propellant for the caustic solution. The effects of inhalation of such a mist can vary from mild irritation of the mucous membranes to severe pneumonitis. Particularly sensitive to damage are the delicate tissues of the eyes. The threshold limit for sodium hydroxide in air is 2 mg/m^3. Industrial practice is the requirement of respirators wherever mists might be encountered. In view of these hazards, the need for a fully enclosed loop with remote operation should be considered. Irregardless of the scale of the operation, an operator must ensure that he is wearing adequate protective clothing at all times.

APPENDIX 6

SPECTRUM ANALYSIS

In order to obtain mass transfer spectra, an isolated wire cathode was operated in conjunction with the 6.4 mm ring cathode. The ring cathode acted to develop the concentration boundary layer. They were operated at the same potential. The fluctuating current in the wire cathode cell was amplified and fed to a spectrum analyzer using the circuit given in Figure A.6-1. Shielded cable was used throughout to limit any external pickup. High and low gain were available as well as fine and coarse adjustment of the D.C. offset.

The spectrum analyzer employed was a Bruel and Kjaer model 2107 analog spectrum analyzer. The Bruel and Kjaer is a constant percentage narrow bandwidth band pass filter with variable centre frequency. The power spectral density of the mass transfer fluctuations is given by

$$F(n_c) = \lim_{n \to 0} \frac{(k'(n_c, \Delta n))^2}{n} \qquad (A.6\text{-}1)$$

For finite Δn, a power spectral density function is given by

$$E(n) = (k'(n_c, \Delta n) / k')^2 / \Delta n \qquad (A.6\text{-}2)$$

where

$k'(n_c, \Delta n)$ = rms value of mass transfer fluctuations passed by the analyzer at the frequency n_c

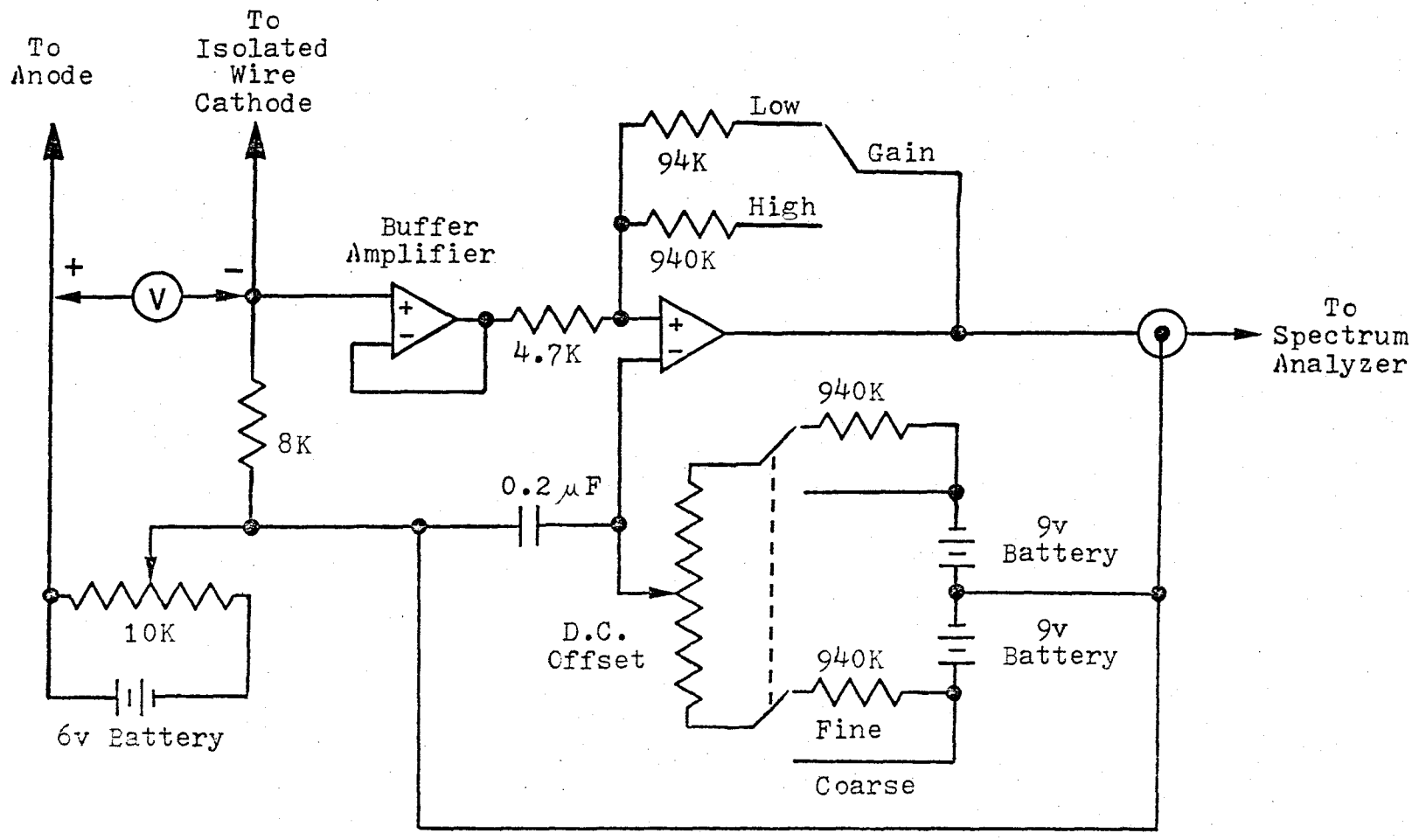

Fig. A.6-1. Circuit for measurement of fluctuations in isolated wire cathode current.

k' = rms value of unfiltered mass transfer fluctuations

Δn = bandwidth

n_c = centre frequency

The bandwidth is 6% of the centre frequency (42).

The rms values of the mass transfer fluctuations were determined with a Bruel and Kjaer model 2417 rms meter with variable time constant.

APPENDIX 7

SAMPLE CALCULATIONS

A.7.1 Single-Phase Experiments

(a) Data for SPR-5a, Run 2 [NaOH] = 1.0 M

Table A.8-6a

r_1 = 1.310 v

r_{P2} = 3.05 v

r_{P3} = 5.75 v

$I_{\ell 3}$ = 29.3 mA

Table A.8-1

(Model 12A20)

(d = -0.01 v)

(d = -0.01 v)

(c_b = 0.0054 M)

Table A.2-1

μ_1 = 1.12 x 10^{-3} kg/m s Sc = 1620

ρ_1 = 1042 kg/m^3

(b) Measured pressure drop

$$\Delta P_2 = 6.89 (r - d) \qquad (A.1\text{-}2)$$

$$= 6.89 (3.05 + 0.01) = 21.08 \text{ kPa/m}$$

$$\Delta P_3 = 1.37 (r - d) \qquad (A.1\text{-}3)$$

$$= 1.37 (5.75 + 0.01) = 7.89 \text{ kPa/m}$$

$$\Delta P_F/L = (\Delta P_2 - \Delta P_3) / L_{23} - \rho_1 g$$

$$= (21.08 - 7.89) / 0.235 - 1.042 (9.81)$$

$$= 45.9 \text{ kPa/m}$$

(c) Measured mass transfer coefficient

$$K = I_\ell / (a_e F c_b) \qquad (3.7)$$

$$= 29.3 / (\pi(12.7)(6.388)(96487)(0.0054))$$

$$= 2.21 \times 10^{-4} \text{ m/s}$$

$$u^* = (\tau_w/\rho)^{\frac{1}{2}} = [\Delta P_F D / (4 \rho L)]^{\frac{1}{2}}$$

$$= [45.9(12.7)/(4(1042))]^{\frac{1}{2}}$$

$$= 0.374 \text{ m/s}$$

$$K^+ = K / u^*$$

$$= 2.21 \times 10^{-4} / 0.374 = 5.90 \times 10^{-4}$$

(d) Empirical pressure drop

$$Q_l = 637 (r) - 3 \qquad (A.1\text{-}6)$$

$$= 637 (1.31) - 3 = 831.5 \text{ ml/s}$$

$$u_l = Q_l / A$$

$$= 831.5 / (\pi(12.7)^2/4) = 6.56 \text{ m/s}$$

$$Re = u D \rho / \mu$$

$$= 6.56(12.7)(1.042) / 1.12 \times 10^{-3} = 77{,}560$$

$$f^{-\frac{1}{2}} = -4 \log_{10}(0.27 \varepsilon/D + 1.26 f^{-\frac{1}{2}} / Re) \qquad (5.1)$$

with $\varepsilon / D = 0.0025$

After four iterations, $f = 0.0067$

$$\Delta P_F / L = 2 f u^2 \rho / D$$

$$= 2 (0.0067)(6.56)^2(1042) / 12.7 = 47.3 \text{ kPa/m}$$

(e) Empirical mass transfer coefficient

$$L^+ = L_e u^* \rho / \mu$$

$$= 6.388 (0.374)(1.042) / 1.12 \times 10^{-3} = 2200$$

Using Metzner and Friend ($L^+ > 1,000$)

$K^+ = 0.085\ (Sc)^{-2/3}$ (Table 3-1)

$= 0.085\ (1620)^{-2/3} = 6.16 \times 10^{-4}$

A.7.2 Two-Phase Experiments

(a) Data for TPR-6, Run 8 [NaOH] = 1.0 M

Table A.9-4

$r_l = 1.00$ USgpm

$r_g = 54$ %

$P_r = 446$ kPa(a)

$I_{\ell 3} = 12.16$ mA

Table A.2-1

$\mu_l = 1.12 \times 10^{-3}$ kg/m s

$\rho_l = 1042$ kg/m^3

Sc = 1620

Table A.9-2

$P_1 = 123$ kPa(a)

$\Delta P_{12} = 5.60$ kPa

$\Delta P_{23} = 1.98$ kPa

(Run 33)

Table A.9-1

$r_\alpha = 11.4$ ml

Annular Flow Regime

(Run 3)

(b) Measured pressure drop and void fraction

$\Delta P / L = \Delta P_{23} / L_{23}$

$= 1.98 / 0.235 = 8.43$ kPa/m

$\alpha = 92 - 1.16\ (r)$ (A.1-10)

$= 92 - 1.16\ (11.4) = 79$ %

$\Delta P_2 = P_1 - \Delta P_{12}$

$= 123 - 5.6 = 117$ kPa(a)

$P_3 = P_2 - \Delta P_{23}$

$= 117 - 1.98 = 115$ kPa(a)

ρ_g = average density in test section

$= (P_2 + P_3) / (2 R T)$

$= (117 + 115) / (2 (0.297)(273 + 25))$

$= 1.31$ kg/m^3

$\Delta P_G / L = [(1 - \alpha) \rho_l + \alpha \rho_g] g$ (from (2.5))

$= [0.21 (1042) + 0.79 (1.31)] 9.81 / 1000$

$= 2.16$ kPa/m

$Q_g = (20.1 (r) - 150) (P_r / T_r)^{\frac{1}{2}}$ (A.1-9)

$= (20.1 (54) - 150) (446/(21 + 273))^{\frac{1}{2}}$

$= 1152$ ml/s

ρ_r = reference density for Q_g

$= 101 / (0.297 (21 + 273)) = 1.16$ kg/m^3

$G_g = Q_g \rho_r / A$

$= 1152 (1.16) / (\pi(13.5)^2 / 4) = 9.34$ kg/m^2 s

$u_g^s = G_g / \rho_g$

$= 9.34 / 1.31 = 7.13$ m/s

$\Delta P_A / L = G_g^2 / (\alpha L \Delta \rho_g)$ (from (2.5))

$= (9.34)^2 / \left[0.79 (235) / \left(0.297(25+273)\left(\frac{1}{113} - \frac{1}{117}\right)\right)\right]$

$= 0.006$ kPa/m

$$\Delta P_F/L = \Delta P/L - \Delta P_G/L - \Delta P_A/L$$
$$= 8.43 - 2.16 - 0.006 = 6.26 \text{ kPa/m}$$

(c) Measured mass transfer coefficients

$$K = I_\ell / (a_e F c_b) \qquad (3.7)$$
$$= 12.16 / (\pi(13.5)(6.388)(96487)(0.005))$$
$$= 9.30 \times 10^{-5} \text{ m/s}$$
$$u^* = [\Delta P_F D / (4 \rho_l L)]^{\frac{1}{2}}$$
$$= [6.26 (13.5) / (4 (1042))]^{\frac{1}{2}} = 0.142 \text{ m/s}$$
$$K^+ = K / u^*$$
$$= 9.30 \times 10^{-5} / 0.142 = 6.55 \times 10^{-4}$$

(d) Empirical pressure drop and void fraction

As the flow regime is annular, Lockhart and Martinelli with Davis' modification will be used.

$$Q_l = 63.9 (r) + 1 \qquad (A.1\text{-}7)$$
$$= 63.9 (1.0) + 1 = 64.9 \text{ ml/s}$$
$$u_l^s = Q_l / A$$
$$= 64.9 / (\pi(13.5)^2 / 4) = 0.45 \text{ m/s}$$
$$X^2 = (u_l^s / u_g^s)^{1.75} (\rho_l/\rho_g)^{0.75} (\mu_l/\mu_g)^{0.25} \qquad (2.17)$$
$$= (0.45/7.13)^{1.75} (1042/1.31)^{0.75} (112/1.8)^{0.25}$$
$$= 3.34$$
$$X_D^2 = 0.0361 [(u^s)^2/(D g)]^{0.37} X^2 \qquad (2.19)$$
$$= 0.0361 [(0.45+7.13)^2/(0.0135(9.81))]^{0.37} 3.34$$
$$= 1.14$$

$$\phi_l^2 = 1 + 20 / X_D + 1 / X_D^2 \qquad (2.18)$$

$$= 1 + 20/1.07 + 1/1.14 = 20.60$$

$$Re_l^s = u_l^s D \rho_l / \mu_l$$

$$= 0.45\ (13.5)(1.042) / 1.12 \times 10^{-3} = 5650$$

$$f = 0.0791\ (\ Re\ )^{-0.25} \qquad (2.11)$$

$$= 0.0791\ (5650)^{-0.25} = 0.0091$$

$$(\Delta P_F / L)_l = 2\ f\ (\ u_l^s\ )^2 \rho_l / D$$

$$= 2\ (0.0091)(0.45)^2(1042) / 13.5 = 0.285\ kPa/m$$

$$(\Delta P_F / L) = (\Delta P_F / L)_l\ \phi_l^2$$

$$= 0.285\ (20.60) = 5.86\ kPa/m$$

$$\alpha = (\ 1 - 1/\ \phi_l\ ) \qquad (2.24)$$

$$= 100\ (\ 1 - 1/4.54\ ) = 78\ \%$$

(e) Empirical mass transfer coefficient

$$L^+ = L_e\ u^*\ \rho_l / \mu_l$$

$$= 6.388\ (0.142)(1.042) / 1.12 \times 10^{-3} = 844$$

Using Leveque $(L^+ < 1000)$

$$K^+ = 0.81\ (\ L^+\ )^{-1/3}\ (\ Sc\ )^{-2/3} \qquad (3.18)$$

$$= 0.81\ (844)^{-1/3}\ (1620)^{-2/3} = 6.21 \times 10^{-4}$$

APPENDIX 8

DATA FOR SINGLE-PHASE EXPERIMENTS

The data for the single-phase experiments are tabulated on the following pages. Note that the inside diameter of the test section was 12.7 mm for this set of experiments.

The potassium ferri- and ferrocyanide were in equimolar concentrations. The sodium hydroxide concentration was 1.00 M for SPR-1 to SPR-9 inclusive. For SPR-10 the sodium hydroxide concentration was 1.95 M.

The turbine flowmeters used, concentration of ferricyanide ion, pressure transducer drifts, cleaning methods and pertinent comments are given in Table A.8-1. The principal data are listed in Tables A.8-2 to A.8-11.

With reference to Table A.8-1, the key for the cleaning methods is:

0 = no cleaning

I = cleanser scrub and cathodic cleaning at 40 mA @ 1.5 v for 30 minutes

II = cleanser and acid scrub, and cathodic cleaning at 40 mA @ 1.5 v for 30 minutes

III = cleanser and acid scrub, and cathodic cleaning at 500 mA @ 2.1 v for 15 minutes

The electrolyte temperature was 25 °C for all the experiments.

The nomenclature for Tables A.8-1 to A.8-11 is

c_b = concentration of ferricyanide ion

I_{ℓ_1}, I_{ℓ_2}, I_{ℓ_3} = limiting currents of 1.6, 3.2 and 6.4 mm ring cathodes, respectively

r_{P1}, r_{P2}, r_{P3} = pressure transducer readings at pressure rings PR1, PR2 and PR3, respectively

r_1 = reading of turbine flowmeter

Table A.8-1. Run Parameters for the Single-Phase Experiments, SPR-1 to SPR-10.

Expt. Number	Turbine Flowmeter Model	$[Fe(CN)_6^{3-}]$ c_b, M	Pressure Transducer Drift, volt DPT1	DPT2	DPT3	Cleaning Method	Comments
-1	12M20	0.0050	0.0	0.0	0.0	0	
-2	12M20	0.0047	-0.01	-0.01	0.0	II	
-3a	12M20	0.0098	0.0	0.0	+0.01	I	3b measurements taken 1 hr after 3a measurements
-3b							
-4	12M20	0.0072	0.0	+0.01	0.0	II	dull polarization curves
-5a	12M20	0.0054	0.0	-0.01	-0.01	II	5b measurements taken 1 hr after 5a measurements
-5b							
-6	12M20	0.0053	-	-	-	II	no pressure measurements
-7	12M20	0.00565	0.0	-0.03	+0.06	III	
-8a	8M5	0.0056	0.0	-0.03	+0.07	III	8b measurements taken 1 hr, 8c measurements taken 2 hrs, after 8a measurements
-8b							
-8c							non-deaerated water used
-9a	8M5	0.0055	+0.01	-0.02	-0.06	III	9b measurements taken 1 hr, 9c measurements taken 3 hrs, after 9a measurements
-9b							
-9c							
-10	8M5	0.0054	+0.04	-0.04	-0.01	III	new Schmidt number

Table A.8-2. Experiment SPR-1 Data.

Run	r_1 volt	r_{P1} volt	r_{P2} volt	r_{P3} volt	I_{ℓ_1} mA	I_{ℓ_2} mA	I_{ℓ_3} mA
1	0.445	1.5	1.9	7.0	-	-	8.8
4	0.620	1.2	1.7	5.0	9.0	15.0	9.8
3	0.820	1.3	1.6	3.0	11.8	19.3	12.3
2	1.010	1.6	1.7	2.0	12.8	23.6	14.8
5	1.215	1.9	1.8	0.5	13.4	24.3	15.2

Table A.8-3. Experiment SPR-2 Data.

Run	r_1 volt	r_{P1} volt	r_{P2} volt	r_{P3} volt	I_{ℓ_1} mA	I_{ℓ_2} mA	I_{ℓ_3} mA
1	0.49	0.77	0.95	2.35	6.5	10.2	11.5
5	0.78	1.27	1.65	4.10	10.2	16.6	17.2
2	1.025	1.63	2.10	4.50	12.2	21.5	22.8
6	1.02	1.63	2.00	4.00	12.1	20.7	21.3
4	1.40	2.47	2.75	4.25	16.15	27.35	29.4
3	1.89	4.00	4.40	5.00	19.7	34.5	39.5

Table A.8-4a. Experiment SFR-3a Data.

Run	r_1 volt	r_{P1} volt	r_{P2} volt	r_{P3} volt	$I_{\ell 1}$ mA	$I_{\ell 2}$ mA	$I_{\ell 3}$ mA
2	0.25	0.83	1.60	5.70	4.2	8.2	12.5
3	0.33	0.87	1.50	5.00	5.3	11.0	15.3
4	0.43	0.97	1.65	5.00	6.2	15.0	18.8
1	0.50	1.00	1.63	4.95	7.95	20.0	22.3
5	0.53	1.03	1.70	4.95	7.3	19.3	22.4
6	0.63	1.17	1.75	4.95	8.2	21.5	24.7
7	0.82	1.40	2.05	5.20	9.5	28.8	31.0
8	1.01	1.77	2.35	4.95	11.5	35.5	37.1
10	1.11	1.93	2.50	4.95	13.5	39.0	39.6
9	1.22	2.20	2.80	5.45	13.5	40.8	43.5

Table A.8-4b. Experiment SFR-3b Data.

Run	r_1 volt	r_{P1} volt	r_{P2} volt	r_{P3} volt	$I_{\ell 1}$ mA	$I_{\ell 2}$ mA	$I_{\ell 3}$ mA
14	0.31	0.83	1.50	4.88	6.0	11.5	14.1
18	0.48	0.97	1.60	4.95	6.9	15.9	19.0
17	0.48	0.97	1.60	4.95	7.1	16.0	19.5
16	0.49	0.98	1.58	4.75	7.2	16.5	19.3
15	0.49	0.97	1.55	4.58	7.2	16.9	19.5
13	0.52	0.98	1.55	4.65	8.0	19.0	20.5
12	0.70	1.27	1.93	5.00	9.9	26.7	26.9
11	0.91	1.60	2.20	4.95	12.0	33.9	33.3

Table A.8-5. Experiment SPR-4 Data.

Run	r_1 volt	r_{P1} volt	r_{P2} volt	r_{P3} volt	I_{f1} mA	I_{f2} mA	I_{f3} mA
9	0.27	0.66	1.50	4.88	7.4	7.7	9.0
10	0.37	0.93	1.60	5.00	11.0	12.2	13.5
11	0.42	0.97	1.69	5.00	10.9	12.8	14.5
8	0.41	0.84	1.48	4.25	13.3	15.0	15.0
1	0.43	0.95	1.65	5.50	13.5	14.4	15.3
7	0.61	0.97	3.26	4.75	19.2	22.0	20.9
6	0.81	1.40	2.08	5.00	24.1	30.3	27.5
5	1.02	1.68	2.45	5.35	28.4	37.4	34.2
4	1.21	2.13	2.70	4.60	34.0	44.0	41.3
3	1.42	2.67	3.40	5.50	38.6	46.7	47.8
2	1.60	3.27	4.09	6.50	41.7	54.2	54.7

Table A.8-6a. Experiment SPR-5a Data.

Run	r_1 volt	r_{P1} volt	r_{P2} volt	r_{P3} volt	$I_{\ell 1}$ mA	$I_{\ell 2}$ mA	$I_{\ell 3}$ mA
7	0.2955	0.87	1.40	4.95	4.9	6.0	7.5
6	0.505	1.03	1.58	4.95	8.1	10.4	11.5
5	0.709	1.32	1.85	5.40	10.9	14.7	16.0
4	0.900	1.58	2.10	5.20	13.5	18.3	20.0
3	1.100	1.97	2.55	5.50	16.1	22.0	24.4
2	1.310	2.47	3.05	5.75	20.2	26.3	29.3
1	1.500	2.93	3.53	5.80	24.0	30.5	33.5

Table A.8-6b. Experiment SPR-5b Data.

Run	r_1 volt	r_{P1} volt	r_{P2} volt	r_{P3} volt	$I_{\ell 1}$ mA	$I_{\ell 2}$ mA	$I_{\ell 3}$ mA
8	0.410	0.97	1.60	5.25	6.3	8.1	9.4
9	0.610	1.17	1.80	5.45	8.8	11.7	13.2
10	0.805	1.47	2.08	5.45	11.3	15.5	17.0
11	1.007	1.85	2.58	6.35	13.7	19.1	20.8
12	1.200	2.23	2.93	6.05	15.8	22.5	24.8
13	1.406	2.67	3.25	5.60	18.2	25.7	28.9
14	1.502	2.93	3.58	6.15	19.0	27.2	30.0

Table A.8-7. Experiment SFR-6 Data.

Run	r_1 volt	r_{P1} volt	r_{P2} volt	r_{P3} volt	I_{ℓ_1} mA	I_{ℓ_2} mA	I_{ℓ_3} mA
9	0.235				4.9	4.9	6.42
8	0.397				7.1	8.0	10.20
1	0.448				8.8	10.5	11.31
7	0.596				10.5	11.6	14.0
6	0.791				13.1	15.5	19.4
5	0.990				16.1	18.8	23.9
4	1.198				18.5	22.7	29.0
3	1.390				21.8	27.0	33.6
10	1.590				24.7	29.3	38.3
2	1.647				27.3	31.0	40.5

Table A.8-8. Experiment SFR-7 Data.

Run	r_1 volt	r_{P1} volt	r_{I2} volt	r_{P3} volt	I_{ℓ_1} mA	I_{ℓ_2} mA	I_{ℓ_3} mA
5	0.300	1.20	1.26	4.4		9.0	8.4
1	0.470	1.29	1.21	3.5		13.0	12.6
4	0.613	1.41	1.43	4.0		16.6	16.4
6	0.830	1.80	1.71	3.8		20.4	21.1
3	1.020	2.20	2.14	4.3		24.6	26.1
7	1.195	2.60	2.45	4.5		27.2	30.1
8	1.404	3.19	2.85	4.1		31.3	35.9
2	1.420	3.18	2.89	4.2		32.5	37.1

Table A.8-9a. Experiment SFR-8a Data.

Run	r_1 volt	r_{F1} volt	r_{F2} volt	r_{F3} volt	$I_{\ell 1}$ mA	$I_{\ell 2}$ mA	$I_{\ell 3}$ mA
7	0.260	0.643	1.365	5.50	1.13	1.35	2.26
6	0.508	0.584	1.400	5.53	2.30	2.50	4.15
5	0.950	0.253	0.624	1.47	3.50	4.06	6.05
4	1.405	0.581	0.770	1.75	4.89	6.01	8.50
3	1.940	0.715	1.020	2.32	7.29	8.64	11.0
2	2.450	1.080	1.310	3.00	9.20	11.73	14.8
1	3.000	1.330	1.670	3.79	12.15	15.25	18.7

Table A.8-9b. Experiment SFR-8b Data.

Run	r_1 volt	r_{F1} volt	r_{F2} volt	r_{F3} volt	$I_{\ell 1}$ mA	$I_{\ell 2}$ mA	$I_{\ell 3}$ mA
12	0.447	0.38	1.41	5.55	2.57	2.62	4.13
11	1.395	0.22	0.77	1.79	5.46	6.39	8.54
10	1.940	0.49	1.02	2.35	7.25	8.80	11.06
9	2.450	0.95	1.34	3.03	9.00	11.22	13.61
8	3.050	1.28	1.76	3.99	10.71	14.06	16.90

A.8-9c. Experiment SPR-8c Data.

Run	r_1 volt	r_{P1} volt	r_{P2} volt	r_{P3} volt	$I_{\ell 1}$ mA	$I_{\ell 2}$ mA	$I_{\ell 3}$ mA
18	0.478	0.38	1.41	5.55	2.53	2.50	4.00
17	0.935	0.29	0.60	1.35	3.86	4.09	6.00
16	1.440	0.31	0.76	1.74	5.48	6.09	7.99
15	1.980	0.44	1.00	2.30	6.99	8.44	10.51
14	2.430	0.98	1.25	2.89	8.40	10.46	12.50
13	3.020	1.26	1.64	3.76	9.80	12.70	14.85

Table A.8-10a. Experiment SPR-9a Data.

Run	r_1 volt	r_{P1} volt	r_{P2} volt	r_{P3} volt	$I_{\ell 1}$ mA	$I_{\ell 2}$ mA	$I_{\ell 3}$ mA
7	0.290	0.475	1.22	4.65	2.01	2.05	3.13
6	0.444	0.502	1.26	4.72	2.67	2.74	4.18
5	0.875	0.544	1.28	4.59	4.15	4.27	6.48
4	1.430	0.608	1.24	3.90	6.10	6.70	9.70
3	1.912	0.705	1.44	4.32	8.32	9.05	12.62
2	2.470	1.150	1.59	4.23	10.95	12.60	16.65
1	2.930	1.290	1.62	3.60	13.17	15.40	20.60

Table A.8-10b. Experiment SPR-9b Data.

Run	r_1 volt	r_{P1} volt	r_{P2} volt	r_{P3} volt	$I_{\ell 1}$ mA	$I_{\ell 2}$ mA	$I_{\ell 3}$ mA
14	0.299	0.551	1.03	3.71	2.11	2.23	3.30
13	0.515	0.538	1.40	5.30	3.07	3.09	4.71
12	0.923	0.495	1.19	4.14	4.53	4.74	6.90
11	1.400	0.560	1.32	4.39	6.14	6.78	9.60
10	1.940	0.678	1.41	4.29	8.04	9.22	12.57
9	2.430	0.950	1.65	4.75	9.68	11.50	15.54
8	3.020	1.150	1.76	4.13	11.50	14.30	19.02

Table A.8-10c. Experiment SPR-9c Data.

Run	r_1 volt	r_{P1} volt	r_{P2} volt	r_{P3} volt	$I_{\ell 1}$ mA	$I_{\ell 2}$ mA	$I_{\ell 3}$ mA
20	0.428	0.736	1.20	4.48	2.69	2.73	4.19
19	0.978	0.769	1.17	4.00	4.68	4.85	7.14
18	1.433	0.872	1.30	4.25	6.18	6.80	9.62
17	1.960	1.010	1.43	4.30	7.99	9.21	12.50
16	2.400	1.180	1.64	4.67	9.41	11.24	14.99
15	3.000	1.310	1.59	3.35	11.03	13.86	18.10
21	2.900	1.340	1.77	4.41	10.60	13.19	17.33

Table A.8-11. Experiment SPR-10 Data.

Run	r_1 volt	r_{P1} volt	r_{P2} volt	r_{P3} volt	I_{X1} mA	I_{X2} mA	I_{X3} mA
7	0.342	0.67	0.96	3.08	2.06	2.58	2.96
6	0.495	0.70	1.00	3.16	2.57	2.65	3.60
5	0.886	0.73	0.99	2.92	3.72	4.25	5.24
4	1.385	0.75	0.84	1.60	5.36	6.65	7.32
3	1.865	0.88	0.93	1.40	7.06	8.80	9.57
2	2.430	1.01	0.95	0.60	8.76	11.60	12.40
1	2.990	1.22	1.08	0.20	10.90	14.30	15.82

APPENDIX 9

DATA FOR TWO-PHASE EXPERIMENTS

The data for the two-phase experiments are tabulated on the following pages. Note that the inside diameter of the test section was 13.5 mm for this set of experiments. The gas temperature at the gas rotameter varied between 14 and 21 °C. This carries over to the gas flow measurement as a variation of less than 1%. Thus the temperature of the gas at the rotameter has been taken to be constant at 21 °C.

The potassium ferrocyanide concentration was 0.0050 M for all the experiments. The sodium hydroxide concentration was 1.00 M for TPR-5 to TPR-8 inclusive. For TPR-9 and TPR-10 the sodium hydroxide concentration was 1.75 M and 3.00 M, respectively. The ferricyanide ion concentration was 0.0050 M for TPR-6 to TPR-10 inclusive. For TPR-5 the ferricyanide ion concentration was 0.0045 M.

The void fraction and flow regime data are given in Table A.9-1. Pressure drops were measured in all the experiments. But in all but TPR-7, the drift of the pressure transducers rendered the results unuseable. Table A.9-2 gives the pressure drop results of TPR-7. The principal data are listed in Tables A.9-3 to A.9-8. The mass transfer spectra data are given in Tables A.9-9 and A.9-10.

The flow temperature was 25 °C for all the experiments.

The nomenclature for Tables A.9-1 to A.9-10 is

A = annular flow regime

C(F) = churn (flooding) flow regime

C(R) = churn (flow reversal) flow regime

I_{ℓ_1}, I_{ℓ_2}, I_{ℓ_3} = time-averaged limiting currents of 1.6, 3.2 and 6.4 mm ring cathodes, respectively

k' = unfiltered rms value of mass transfer fluctuations passed by spectrum analyzer

$k'(n_c)$ = rms value of mass transfer fluctuations passed by spectrum analyzer at the frequency n_c, 6% bandwidth

n_c = centre frequency

P_1 = pressure at pressure ring PR1

P_r = gas pressure at gas rotameter

ΔP_{12} = time-averaged pressure drop between pressure rings PR1 and PR2

ΔP_{23} = time-averaged pressure drop between pressure rings PR2 and PR3 (across the test section)

r_α = reading of voidmeter

r_g = reading of gas rotameter with Float II

r_l = reading of liquid rotameter

S = slug flow regime

Table A.9-1. Void Fraction and Flow Regime Data for the Two-Phase Experiments.

Run	r_l USgpm	r_g %	P_r kPa(a)	r_α ml	Regime
9	0.25	12	170	41.0	S
31		12	446	37.4	S
10		21	446	19.0	C(R)
30		35	446	12.0	C(F)
11		54	446	9.5	A
29		74	446	8.0	A
12		100	446	5.3	A
16	0.60	12	170	48.8	S
32		12	446	45.8	S
15		21	446	28.3	C(R)
27		35	446	14.3	C(F)
14		54	446	12.8	A
18		74	446	8.0	A
13		100	446	6.7	A
1	1.00	12	170	52.1	S
33		12	446	49.0	S
2		21	446	32.8	C(R)
26		35	446	14.4	C(F)
3		54	446	11.4	A
25		74	446	8.1	A
4		100	446	6.8	A
17	1.60	12	170	60.3	S
34		12	446	56.3	S
18		21	446	34.2	S
23		35	446	20.5	C(F)
19		54	446	16.0	A
24		74	446	13.4	A
20		100	446	9.9	A
8	2.20	12	170	63.4	S
35		12	446	60.8	S
7		21	446	40.3	S
22		35	446	29.5	S
6		54	446	20.2	A
21		74	446	15.8	A
5		100	446	13.0	A

Table A.9-2. Pressure Drop Data for the Two-Phase Experiments.

Run	r_l USgpm	r_g %	P_r kPa(a)	P_1 kPa(a)	ΔP_{12} kPa	ΔP_{23} kPa
18	0.25	12	170	128	4.21	1.47
36		12	446	126	3.97	1.40
20		21	446	119	3.04	1.05
15		35	446	116	2.69	0.94
19		54	446	119	2.79	0.99
16		74	446	118	3.11	1.10
17		100	446	119	3.25	1.15
23	0.60	12	170	122	5.07	1.76
37		12	446	121	4.92	1.71
22		21	446	117	4.15	1.49
12		35	446	119	3.96	1.35
21		54	446	119	4.05	1.44
13		74	446	121	4.48	1.59
14		100	446	123	5.15	1.75
30	1.00	12	170	124	5.37	1.88
38		12	446	123	5.35	1.87
31		21	446	121	5.22	1.80
32		35	446	119	4.21	1.63
33		54	446	123	5.60	1.98
34		74	446	126	6.19	2.19
35		100	446	129	7.14	2.50
24	1.60	12	170	126	6.06	2.18
39		12	446	125	6.02	2.16
25		21	446	122	5.82	2.08
9		35	446	126	6.80	2.32
26		54	446	129	7.70	2.61
10		74	446	132	8.58	3.00
11		100	446	136	10.38	3.54
29	2.20	12	170	128	7.00	2.42
40		12	446	127	7.06	2.43
28		21	446	126	7.18	2.49
6		35	446	128	8.66	3.00
27		54	446	132	9.94	3.36
7		74	446	132	11.18	3.95
8		100	446	136	13.26	4.59

Table A.9-3. Experiment TPR-5 Data.

Run	r_l USgpm	r_g %	P_r kPa(a)	$I_{\ell 1}$ mA	$I_{\ell 2}$ mA	$I_{\ell 3}$ mA
3	0.25	0		0.65	1.09	1.70
19		12	170		3.06	4.68
20		21	446		4.49	7.09
21		54	446		4.50	7.52
22		100	446		5.26	8.58
4	0.60	0		1.10	1.70	2.70
23		12	170		3.28	5.11
24		21	446		4.97	7.86
25		54	446		5.55	8.97
26		100	446		6.76	10.73
2	1.00	0		1.46	2.25	3.81
15		12	170		3.46	5.50
16		21	446		5.40	8.52
17		54	446		6.57	10.48
18		100	446		7.82	13.07
5	1.60	0		1.89	2.96	4.92
27		12	170		3.93	6.63
28		21	446		5.75	9.18
29		54	446		7.62	11.89
30		100	446		8.85	15.03
1	2.20	0		2.38	3.70	6.06
6		0		2.30	3.60	6.10
7		0		2.25	3.50	6.05
8		12	170		4.43	7.24
34		12	170		4.50	7.14
9		21	446		5.88	9.58
33		21	446		6.19	9.66
32		54	446		8.38	13.66
31		100	446		9.51	16.43
11		100	446		9.89	16.67

Table A.9-4. Experiment TPR-6 Data.

Run	r_l USgpm	r_g %	P_r kPa(a)	$I_{\ell 1}$ mA	$I_{\ell 2}$ mA	$I_{\ell 3}$ mA
5	0.25	0		0.71	1.10	1.83
27		12	446		3.27	5.63
28		35	446		5.07	7.87
29		54	446		5.16	8.29
30		74	446		5.50	9.09
31		100	446		5.86	9.52
4	0.60	0		1.20	1.80	2.94
22		12	446		3.70	6.23
23		35	446		5.72	9.57
24		54	446		6.18	9.94
25		74	446		6.86	11.02
26		100	446		7.46	11.84
3	1.00	0		1.71	2.52	4.13
7		12	446		3.81	6.49
11		35	446		6.32	9.57
8		54	446		7.30	12.16
10		74	446		7.90	13.50
9		100	446		8.80	14.61
2	1.60	0		2.13	3.25	5.50
17		12	446		4.43	7.47
18		35	446		6.95	11.36
19		54	446		8.19	13.45
20		74	446		9.23	15.42
25		100	446		10.08	16.74
1	2.20	0		2.63	4.10	6.55
6		0		2.60	3.90	6.50
12		12	446		5.06	8.19
13		35	446		8.45	13.07
14		54	446		9.30	15.30
15		74	446		10.08	17.04
16		100	446		10.82	18.53

Table A.9-5. Experiment TPR-7 Data.

Run	r_l USgpm	r_g %	P_r kPa(a)	$I_{\ell 1}$ mA	$I_{\ell 2}$ mA	$I_{\ell 3}$ mA
5	0.25	0		0.76	1.18	1.92
15		35	446		5.00	7.81
16		74	446		5.67	8.75
17		100	446		6.03	9.75
4	0.60	0		1.22	1.80	3.04
12		35	446		6.00	9.20
13		74	446		7.22	11.40
14		100	446		7.79	12.07
3	1.00	0		1.66	2.54	4.15
2	1.60	0		2.12	3.37	5.43
9		35	446		7.22	11.55
10		74	446		9.04	15.24
11		100	446		10.27	16.70
1	2.20	0		2.60	3.90	6.40
6		35	446		8.56	12.69
7		74	446		10.04	16.62
8		100	446		10.84	18.23

Table A.9-6. Experiment TPR-8 Data.

Run	r_l USgpm	r_g %	P_r kPa(a)	$I_{\ell 1}$ mA	$I_{\ell 2}$ mA	$I_{\ell 3}$ mA
5	0.25	0		0.74	1.19	1.85
4	0.60	0		1.17	1.87	2.98
3	1.00	0		1.62	2.60	4.19
6		12	446		4.16	6.53
7		35	446		6.53	9.70
8		54	446		7.86	11.74
9		74	446		8.75	14.06
10		100	446		9.28	15.86
2	1.60	0		2.19	3.35	5.49
1	2.20	0		2.60	4.06	6.67

Table A.9-7. Experiment TPR-9 Data.

Run	r_l USgpm	r_g %	P_r kPa(a)	$I_{\ell 1}$ mA	$I_{\ell 2}$ mA	$I_{\ell 3}$ mA
5	0.25	0		0.67	1.02	1.62
19		35	446		4.48	6.62
20		74	446		5.07	7.57
21		100	446		5.29	8.70
4	0.60	0		0.99	1.61	2.44
16		35	446		5.07	8.33
17		74	446		6.38	10.09
18		100	446		7.23	10.85
3	1.00	0		1.43	2.20	3.58
6		35	446		5.40	8.80
9		54	446		6.72	9.94
8		74	446		7.86	12.07
7		100	446		8.67	13.30
2	1.60	0		1.90	2.89	4.78
13		35	446		6.68	9.99
14		74	446		8.42	13.87
15		100	446		9.81	15.29
1	2.20	0		2.28	3.58	5.72
10		35	446		7.33	11.03
11		74	446		8.66	14.67
12		100	446		9.65	15.80

Table A.9-8. Experiment TPR-10 Data.

Run	r_l	r_g	P_r	$I_{\ell 1}$	$I_{\ell 2}$	$I_{\ell 3}$
	USgpm	%	kPa(a)	mA	mA	mA
5	0.25	0		0.45	0.66	1.10
18		35	446		3.08	5.11
19		74	446		3.27	5.63
20		100	446		3.55	6.20
4	0.60	0		0.77	1.15	1.85
15		35	446		3.22	5.50
16		74	446		4.07	7.10
17		100	446		4.50	7.67
1	1.00	0		1.03	1.55	2.41
12		35	446		4.06	5.96
13		74	446		5.24	8.74
14		100	446		5.91	9.48
3	1.60	0		1.37	2.16	3.25
9		35	446		4.79	6.53
10		74	446		5.83	9.31
11		100	446		6.50	10.35
2	2.20	0		1.59	2.44	4.00
6		35	446		5.11	7.29
7		74	446		6.35	10.32
8		100	446		6.96	11.26

Table A.9-9. Spectra Data for Experiment TPR-5.

n_c Hz	$k'(n_c) / (k' \times 10^{-4})$			
	Run 1 (Single-Phase)	Run 8 (Slug)	Run 19 (Slug)	Run 22 (Annular)
6.3	720	770	860	690
10	900	1340	360	870
20	930	780	200	1040
40	530	380	98	790
60	470	320	77	460
80	380	290	43	300
100	310	230	41	220
200	66	150	45	44
400	38	86	23	50
600	52	69	18	46
1000	38	40	11	26

Table A.9-10. Spectra Data for Experiment TPR-6.

n_c Hz	$k'(n_c) / (k' \times 10^{-4})$					
	Run 7 (Slug)	Run 11 (Churn)	Run 12 (Slug)	Run 17 (Slug)	Run 27 (Slug)	Run 31 (Annular)
6.3	1600	780	560	610	1940	560
8	1470	860	1130	790	850	625
10	960	1010	1870	910	450	660
12	670	1070	1270	960	350	690
15	470	1040	670	900	250	700
20	200	1100	420	770	230	600
40	100	310	120	360	82	240
70	67	240	100	290	47	140
100	44	195	47	160	29	110
200	29	105	24	79	33	88
400	26	36	22	41	35	43
700	23	23	22	29	21	24
1000	22	19	16	25	18	21